A MAGNETIC RESONANCE STUDY OF ALKALI ION BATTERY CATHODES

A MULTINUCLEAR MAGNETIC RESONANCE STUDY OF ALKALI ION BATTERY CATHODE MATERIALS

BY CHELSEY L. HURST, B.SC.

A Thesis Submitted to the School of Graduate Studies in Partial Fulfilment of the Requirements for the Degree Master of Science

McMaster University MASTER OF SCIENCE (2019) Hamilton, Ontario (Chemistry)

TITLE: A Multinuclear Magnetic Resonance Study of Alkali Ion Battery Cathode Materials

AUTHOR: Chelsey L. Hurst, B.Sc. (Redeemer University College)

SUPERVISOR: Professor Gillian R. Goward

NUMBER OF PAGES: xv, 125

Lay Abstract

The need for highly efficient energy storage devices, especially in the form of batteries, has been steadily increasing due to growing energy demands. Presently, the most commercialized types of batteries are lithium ion batteries (LIBs). Concerns over the relatively limited global lithium supply, however, have led to the development of sodium ion battery (SIB) alternatives. Various solid-state nuclear magnetic resonance (ssNMR) techniques have been employed in this thesis to investigate both LIB and SIB cathode materials. The LIB cathode $Li[Ni_{0.6}Mn_{0.2}Co_{0.2}]O_2$ was examined with a combination of ssNMR and Monte Carlo simulations, and it was found that ion clustering occurs in the pristine form of these materials. The promising family of SIB cathodes, $Na_3V_{2-x}Ga_x(PO_4)_2F_3$, was studied by a combination of ssNMR, *ab initio* calculations, and EPR, which allowed for a correlation to be established between the crystal structure and the fast ion dynamics within these materials.

Abstract

The need for highly efficient energy storage devices has been steadily increasing due to growing energy demands. Research in electrochemical energy storage in the form of batteries has consequently become crucial. Currently, the most commercialized battery technology is the lithium ion battery (LIB). Concerns over the relatively limited global lithium supply, however, have led to the development of sodium ion batteries (SIBs). Solid-state nuclear magnetic resonance (ssNMR) spectroscopy is an ideal technique for analyzing battery materials as it can potentially distinguish between different ions within the material.

The most typical cathode for commercial LIBs are the family of NMC layered oxides with the general form $Li[Ni_xMn_yCo_{1-x-y}]O_2$, which consist of Li layers between sheets of transition metals (TMs). The pj-MATPASS NMR technique, in conjunction with Monte Carlo simulations, was applied to investigate the ionic arrangement within TM layers of NMC622 ($Li[Ni_{0.6}Mn_{0.2}Co_{0.2}]O_2$), which revealed the presence of ion clustering in the pristine form of this material.

This thesis also investigated the promising SIB cathode, $Na_3V_2(PO_4)_2F_3$ (NVPF). NVPF has the capability to produce energy densities comparable to those of LIBs and is well understood from a structural standpoint, however ion dynamics within the material are still undetermined. A series of materials have, therefore, been synthesized with the general form, $Na_3V_{2-x}Ga_x(PO_4)_2F_3$ (where x = 0, 1, and 2), where diamagnetic Ga^{3+} was introduced into the structure to enable the establishment of a structural correlation with observed Na-ion dynamics. It, therefore, became possible to explore ionic site exchange using ^{23}Na ssNMR. Density functional theory (DFT) calculations have also been performed alongside ssNMR to confirm chemical shift assignments and provide structural insight. Additionally, electron paramagnetic resonance (EPR) spectroscopy was also used to investigate the paramagnetic nature of NVPF and its variants. Insights into the ionic arrangement and very fast Na-ion dynamics within these materials were revealed.

Acknowledgements

There are many people I must thank for their invaluable support throughout this process. Firstly, my supervisor Dr. Gillian Goward for patiently teaching and supporting me throughout my work. You have always mirrored kindness and strength as a leader. I would also like to thank you for intentionally fostering a fun and supportive environment within our research group.

I would like to thank Dr. Darren Brouwer for, amongst many other things, guiding me throughout both my undergraduate and graduate studies, and for introducing me to the Goward group. Thank you as well for inspiring my love of learning merely for the sake of learning, and for recognizing and encouraging my strengths throughout this pivotal period in my life.

I must also thank my fellow past and present Goward group members for their assistance and encouragement. I would not have accomplished this work without your help. I would especially like to thank Dr. Kris Harris for his constant support during the fist year of my program. You made the daunting task of learning solid-state NMR not only possible but also enjoyable. Dr. Yurij Mozharivskyj must also be thanked for teaching me so much throughout my studies, and for very patiently answering all of my many questions. Thank you as well to the NMR staff including Bob Berno, Hilary Jenkins, and Megan Fair for their support and assistance.

Lastly, I must thank my family for coming along on this journey with me. To my sisters, thank you for uplifting me throughout this process and helping keep all things in perspective. To my parents, thank you for your encouragement and excitement about my work. Your prayers and support have carried me through my whole academic journey.

Table of Contents

List of Figures

List of Tables

List of Abbreviations and Symbols

HEV	Hybrid electric vehicle
EV	Electric vehicle
LIB	Lithium ion battery
SEI	Solid electrolyte interphase
PC	Propylene carbonate
LCO	Lithium cobalt oxide, $LiCoO_2$
LNO	Lithium nickel oxide, $LiNiO_2$
LMO	Lithium manganese oxide, $LiMnO_2$
NMC	$Li[Ni_xMn_yCo_{1-x-y}]O_2$
NCA	$Li[Ni_{0.8}Co_{0.15}Al_{0.05}]O_2$
SIB	Sodium ion battery
LFP	$LiFePO_4$
NASICON	Na super ionic conductor
NVP	$Na_3V_2(PO_4)_3$
XRD	X-ray diffraction
TEM	Transmission Electron Microscopy
STEM	Scanning Transmission Electron Microscopy
ssNMR	Solid-state nuclear magnetic resonance

NMC622	$Li[Ni_{0.6}Mn_{0.2}Co_{0.2}]O_2$
TM	Transition metal
NVPF	$Na_3V_2(PO_4)_2F_3$
SI	Selective inversion
EXSY	Two-dimensional exchange spectroscopy
r.f.	Radio frequency
T_2	Transverse relaxation time
T_1	Spin-lattice relaxation time
CSA	Chemical shift anisotropy
MAS	Magic angle spinning
SSB	Spinning sideband
CT	Central transition
ST	Satellite transition
DFT	Density Functional Theory
ECF	Exchange-correlation functional
LDA	Local density approximation
GGA	Generalized gradient approximation
PBE	Perdew–Burke–Ernzerhof
EPR	Electron paramagnetic resonance
SOC	Sate of charge

PVDF	Polyvinylidene fluoride
NMP	N-methyl-2-pyrrolidone
EC	Ethylene carbonate
DEC	Diethyl carbonate
DMC	Dimethyl carbonate
NVGPF	$Na_3VGa(PO_4)_2F_3$
NGPF	$Na_3Ga_2(PO_4)_2F_3$
h-NVGPF	Homogenous-NVGPF
AF	Antiferromagnetic
IRC	Irreversible capacity loss

Declaration of Academic Achievement

The study of NMC622 was begun by a former postdoctoral researcher, Dr. Kristopher Harris, under the supervision of Dr. Gillian Goward. Dr. Harris was also responsible for determining the experimental parameters for all pj-MATPASS spectra presented in this work. The Monte Carlo calculations and simulated spectra were done in a collaboration between Dr. Harris at McMaster University and Dr. Jamie Foster at the University of Portsmouth, UK. The Rietveld refinement of NGPF was completed with aid of Dr. Yurij Mozharivskyj at McMaster University. DFT calculations were performed by the author, under the guidance of Dr. Dany Carlier at the Institut de Chimie de la Matière Condensée de Bordeaux which is affiliated with the Université de Bordeaux. The VASP software was hosted by the Université de Bordeaux. Al other experimental work was completed by the author at McMaster University.

Chapter 1: Introduction to alkali ion battery cathode materials

1.1 Motivation and background

With the drastic increase in technology development over the past few hundred years, the current period in history can accurately be considered the "age of technology".[1-2] While various technologies can be extremely beneficial for society, it is important for scientists to consider not only technological advancement but also the impact it can have on the world at large. New and developing technologies can have far reaching ramifications in many areas of society, including the energy sector.[3-4]

Interestingly, in recent years the total energy consumption has grown faster than the population indicating that people are using more and more energy in their daily lives.[5] This trend is expected to continue. It is estimated by the U.S. Energy Information Administration that the global energy demand will increase by 56% between 2010 and 2040,[5] which will be problematic when considering the majority of global energy is currently sourced from fossil fuels. Fossil fuels produce environmentally harmful substances upon combustion such as NO_x, SO_x, and CO_2.[6-7] Scientists believe that excess CO_2 in the environment will have a widespread and damaging impact, irreversibly altering the earth's ecosystems. Excess atmospheric CO_2 can cause ocean acidification and effect climate change.[7] On a smaller scale, air pollution from NO_x and SO_x caused by fossil fuel combustion of gasoline, especially in urban environments, can be harmful to human health.[8] It is, therefore, evident that the current rate of usage and development

of fossil fuel-based technologies will have damaging environmental consequences as energy demand increases over the next several years.

In order to effectively address this issue, the combustion of fossil fuels must be minimized or eliminated.[9] One method to diminish the combustion of fossil fuels is to ensure that all grid electricity is sourced from renewable energy. There have been many advances in renewable energy harvesting technologies, such as wind turbines, photovoltaic cells, and pumped hydro.[10-13] However, many of these technologies are dependent on weather conditions or geographical specifications, which have inhibited their mainstream adoption.[10] Therefore, in order to achieve the same reliability that fossil fuels provide, efficient energy storage devices must be found that can store renewable energy for use in non-ideal conditions, such as windless or cloudy days. These storage devices must be able to reliably take in and release large amounts of energy with long term stability.[9]

A similar bottleneck exists in moving away from fossil fuel combustion in the transportation sector. Energy storage devices can be used to power vehicles rather than gasoline, which would help mitigate the negative environmental impacts of fossil fuel combustion. Appropriate energy storage devices for vehicle applications must have comparably high energy density and a long lifespan.

The development of energy storage devices is, therefore, the key to moving away from the combustion of fossil fuels towards a more environmentally sustainable future. Electrochemical energy storage in the form of batteries is the most promising

technology within the energy sector, which is most likely the reason that research into battery technology has boomed over the past several decades.[9, 14-18]. Between 2010 and 2017 alone there was a 260% growth in the total literature volume relating to batteries.[19] This surge in interest is due to the many benefits batteries are capable of providing the energy sector. Batteries can ideally be charged by renewable energy sources during periods with optimal conditions, and then discharged to release electricity during less ideal conditions.[10] Similarly, batteries are excellent devices to replace fossil fuel reliance in vehicles. Instead of combusting gasoline, one could ideally operate a vehicle's engine solely from battery discharge, effectively eliminating much of the environmental strain in the transportation sector.[18]

Interestingly, the idea of using batteries to power vehicles is as old vehicles themselves. When vehicles were first popularized a century ago, they were often powered by lead-acid and nickel-iron batteries, which were invented by Gaston Plantè in 1859 and Thomas Edison in 1901, respectively.[18] In the early nineteen hundreds Henry Ford and Thomas Edison collaborated with the aim to produce a working, inexpensive electric powered vehicle. Henry Ford is quoted as saying, "The problem so far has been to build a storage battery of light weight which would operate for long distances without recharging."[20] Unfortunately, over a century later that problem has not been fully resolved. The work done by Edison and Ford was, however, crucial for laying down the foundation for modern day battery technology. The batteries used in Henry Ford's early models were the precursor to the nickel-metal hydride batteries introduced in 1989,

which currently power the Toyota Prius, a hybrid electric vehicle (HEV).[18] With the goal to make the fully EVs, and considering the heaviness and low operating voltage of Ni-metal hydride batteries, there still remains many research challenges to be overcome in developing suitable batteries for EV applications.

1.2 Introduction to Lithium-Ion Batteries

The battery industry was fundamentally altered with the introduction of a rechargeable high-voltage lithium ion battery (LIB) by Sony Corporation in 1991, which catapulted LIBs to the forefront of battery technology.[18] Since then, varieties of LIBs have been developed, all of which share a common design. A typical LIB consists of an

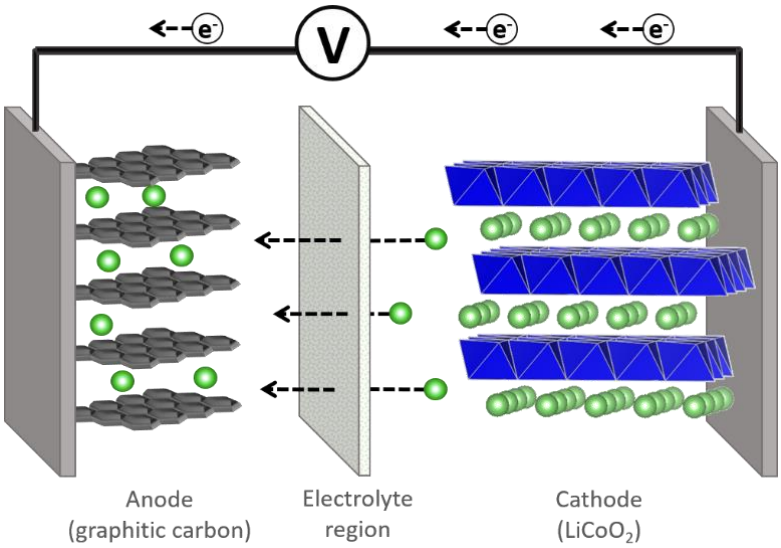

Figure 1.1 A diagram of a typical charging LIB showing Li ions (green spheres) traveling from the cathode (depicted as $LiCoO_2$), through an electrolyte region containing a separator, and into the anode (pictured as graphite sheets) with the corresponding elctron flow through an external curicuit.

anode and cathode separated by an electrolyte, as illustrated in Figure 1.1. During charging, Li^+ ions travel from the cathode through an electrolyte region and into the anode, corresponding with an electron flow through an external circuit. For example, the LIB introduced by Sony Corporation in 1991 operated using a Li_xC_6/non-aqueous liquid electrolyte/$Li_{1-x}CoO_2$ system.[18] Generally, electrolyte solutions prevent electron flow, forcing electrons into the external circuit. Therefore, increasing the amount of ions flowing through the battery will further promote electrons traveling through the external circuit, which corresponds to greater electrical output. Consequently, battery research must be focused on developing materials that allow efficient ion storage (high capacity) and fast ion motion.

Originally, Li metal was used as the anode material in LIBs. However, Li metal suffers from poor cyclability.[21] Lithium plating on the solid electrolyte interface (SEI) during lithiation induced volume expansion can make the SEI layer crack.[22] From these cracks, dendrites can form, break free, and contribute to a layer of dead Li on the surface of the anode. Over repeated cycling, this layer of dead Li causes capacity fade. Additionally, dendritic growth can cause thermal runaway, a process where a positive feedback loop is established between increasing reaction rate and temperature.[23] Thermal runaway can then lead to the battery short circuiting and potentially catching on fire. It should be noted, however, that the formation of a stable SEI layer is crucial to a batteries performance in that it provides both a protective passivation layer as well as kinetic stability during lithiation and delithiation.[10]

Although the many drawbacks of using Li metal have led to the development of alternative anode materials, there has recently been a resurgence of interest in finding ways to incorporate Li metal into the anode.[22, 24] This is due to the fact that current LIB technology is not expected to fulfill growing energy demands, and Li metal has the highest theoretical capacity and lowest electrochemical potential which will be necessary moving forward. Regardless, the most common anode material currently on the market is graphitic carbon.[21] Graphitic carbon has been very successful because it easily allows for Li intercalation between graphite layers, providing good electrical conductivity and Li transport capabilities. However, the most common electrolyte solutions include propylene carbonate (PC) because it allows for fast Li ion transportation and has a low melting point. Unfortunately, PC can co-intercalate with Li ions between graphite layers, which causes decreased capacity. Consequently, alternative anode materials have been investigated, such as other intercalation materials, like lithium titanium oxide (LTO), or alloy materials that reversibly alloy with Li during cycling.[9, 21]

Cathode materials are a promising area of LIB research where capacity and ion motion capabilities can be optimized to improve battery performance, because the materials are readily tunable. Cathode materials are also the focus of this thesis. As already stated, the first highly successful LIB developed by Sony used a lithium cobalt oxide cathode ($LiCoO_2$, known as LCO) which has a high theoretical specific capacity (274 mAh/g), experimental specific capacity 155 mAh/g, and unprecedented high cycling

voltage.[18, 21, 25] This material was first discovered for battery application ten years earlier by Goodenough et. al.[26] who found that Li ions were able to reintercalate during cycling at higher voltages than had previously been observed. The crystal structure of LCO in the R$\overline{3m}$ space group was shown as the cathode material in Figure 1.1. Layers of Co in octahedral environments are separated from layers of Li by oxygen layers.[27] Although many improvements have been made in the realm of LIB cathodes since the introduction of LCO in 1991, it is still commonly utilized in batteries today.[21, 25]

Several developments in the LCO system were designed to mitigate its limitations. For one, the high cost of Co makes LCO a relatively expensive cathode.[21] Secondly, as a layered material, the structure becomes unstable at high voltages (over 4.2 V) when more than 50% of the Li has been extracted. This instability distorts the lattice symmetry and inhibits further battery cycling. Lastly, LCO has low thermal stability. At elevated temperatures thermal runaway will occur, similar to what was discussed with regards to Li metal anodes, which can cause the battery to short circuit and potentially catch on fire. One particularly effective way these issues with LCO were addressed was by incorporating elements of similar layered oxide materials, such as LNO ($LiNiO_2$) and LMO ($LiMnO_2$) to make a superior combined cathode material. For various reasons, both LNO and LMO are not suitable cathode materials on their own. LNO has a comparable specific capacity (275 mAh/g) to LCO and is more ideal from a cost perspective because Ni is less expensive than Co.[28] However, LNO is more thermally unstable than LCO. Additionally, Ni^{2+} in the structure will often substitute in the place of

Li^+ during both the synthesis and delithiation, which inhibits cycling by blocking the pathways for Li-diffusion. Similarly, LMO can be considered an effective cathode material because Mn is cheaper and less toxic than both Co and Ni.[21] Unfortunately, the structure of LMO is unstable upon cycling and tends to convert from a layered to a spinel structure. Mn^{2+} also tends to leach out of the material, dissolve into the electrolyte, and destabilize the SEI on the anode.

In order to capitalize on the various strengths of each of these layered oxide materials, while also minimizing their weaknesses, various combinations of LCO, LNO, and LMO have been designed and tested as cathodes materials. The most common variant is one which combines all three materials in the general form $Li[Ni_xMn_yCo_{1-x-y}]O_2$), referred to as NMC.[21, 25] NMC is more cost effective than LCO because it has less Co. Furthermore, depending on the values of x and y in the chemical formula, it can reach comparable or even higher specific capacities. Due to charge distribution throughout the material, the ions in pristine NMC exist as Ni^{2+}, Ni^{3+}, Co^{3+}, and Mn^{4+}.[29] The combination of these metals in their respective oxidation states was found to offset many of the limitations observed in the pure parent compounds.[19, 29] For example, while Ni is more ideal from a cost perspective than Co, mixing Co^{3+} with Ni^{2+} prevents Ni^{2+} from swapping with Li during synthesis and intercalation. Mn is also cheaper than both Co and Ni, but has the added benefit of providing thermal and structural stability to the material when combined with Ni and Co. Although Mn^{4+} is electrochemically inactive, having Mn in the 4+ oxidation state pushes some Ni^{3+} into Ni^{2+}, thereby increasing

capacity, while also eliminating the tendency of Mn^{2+} formation and subsequent leaching into the electrolyte. The first NMC variant was developed by Yabuuchi and Ohzuku in 2003.[30] This variant used equal amounts of Ni, Mn, and Co in a 1:1:1 ratio, hence the name NMC111 ($Li[Ni_{0.33}Mn_{0.33}Co_{0.33}]O_2$). Like LCO, NMC111 is a layered material in the $R\overline{3}m$ space group and has a theoretical specific capacity of approximately 200 mAh/g, and a typical experimental specific capacity of 160 mAh/g.[21, 30] Although NMC111 was introduced over fifteen years ago, it is still one of the most commonly used cathode materials in batteries today.

Much work has been devoted to understanding, from an electrochemical perspective, how the NMC family of cathodes are able to function so successfully. One of the most important findings was that Ni acts as the redox active centre in the material throughout the typical voltage window of 2.5 – 4.5 V through the $Ni^{2+} \rightarrow Ni^{3+} \rightarrow Ni^{4+}$ oxidation pathway.[29, 31] It would seem logical then that including a greater proportion of Ni into NMC materials would increase their cycling capacities. This idea has led to the development of Ni-rich NMC materials, which have generally demonstrated improved experimental capacities. Naturally, increasing the amount of Ni in the material also increases the safety issues associated with the thermal instability of LNO. These safety issues must be addressed if Ni-rich materials are to become viable cathodes for battery applications.

One example of a successfully implemented Ni-rich material is NCA ($Li[Ni_{0.8}Co_{0.15}Al_{0.05}]O_2$), which combines LNO and LCO with a small amount of Al doping.[21]

Small amounts of Al doping can increase thermal stability and overall performance of the battery. NCA has a comparatively high experimental discharge capacity (approximately 200 mAh/g), which can be attributed to the relatively large proportion of Ni in the material. For this reason, NCA has been used in Tesla EVs.[21, 25] However, this material has been shown to experience capacity fade over time and even thermal runaway in delithiated states.[32] Similar drawbacks have been observed for other high capacity Ni-rich NMC variants, such as NMC811 ($Li[Ni_{0.8}Mn_{0.1}Co_{0.1}]O_2$), which have generally limited the acceptance of Ni-rich materials into the battery mass market. One method to obtain a safe Ni-rich material has been to optimize the structure of the material. This was demonstrated clearly by Sun et. al.[32] who were able to overcome much of these safety limitations by designing a particulate NMC variant with an average composition of $Li[Ni_{0.68}Mn_{0.18}Co_{0.18}]O_2$, where each particle contained a core-shell structure. The particles were synthesized using a specially designed co-precipitation method. The core bulk material of each particle is NMC811. The outer shell is composed of $Li[Ni_{0.46}Mn_{0.31}Co_{0.23}]O_2$ which is far more thermally stable, and consequently safer, than the Ni-rich core. This biphasic particle design allows for the high capacity of NMC811 to be harnessed in a much safer way. This material has achieved an experimental specific capacity of 209 mAh/g, making it suitable for plug-in hybrid EVs. While this is an impressive outcome, it resulted from structural optimization rather than from improving the electrochemical properties of the material itself. In order to extend

the capacity of Ni-rich materials to where it can power fully electric EVs, the inherent capacity limitations of Ni-rich materials must be overcome.

While there has been a great deal of progress in the last several decades in producing batteries capable of powering EVs, there still remains much work to be done. Out of all the components of the battery, cathode materials arguably have the most design flexibility, and therefore, the greatest potential for innovation. Consequently, much research has been devoted to optimizing battery cathode materials for LIBs, as previously discussed. All of the currently utilized cathodes have serious shortcomings in either capacity limitations or safety, both of which must be improved for EV application. Because Ni-rich materials have shown so much promise as viable cathode materials, it is important to understand the exact mechanisms at the electrochemical level by which they function so effectively. Such knowledge would aid in strategically designing the next generation of LIB cathode materials.

1.3 Introduction to Sodium-Ion Batteries

While it is true that LIBs have dominated the battery market since their introduction in the early 1990s, recently, concerns about the global Li supply have led to research into LIB alternatives. Li is the smallest and lightest metal on the periodic table, and it will most likely remain as the primary metal used for lightweight, high capacity battery applications, such as in EVs.[14-15] However, it is estimated that the global Li supply

could not support LIB application in both large-scale grid energy storage and widespread use of EVs, ultimately driving up the cost of Li to where LIB technology becomes unfeasible. The introduction of extensive battery recycling programs may not even be enough to support Li depletion at such a high rate. It should also be noted that many Li reserves exist in remote areas or in areas of political unrest, leading to uncertainty in maintaining a constant Li supply from these areas.

Accordingly, researchers have switched their focus primarily to LIB alternatives in the form of sodium-ion batteries (SIBs). Na is an ideal alternative to Li in many respects. By merely examining the relative positions of Li and Na on the periodic table one would expect Na to have similar properties compared to Li, which turns out to be the case here. Both Na and Li have a single unpaired electron in their outermost shell, which could potentially be harnessed for electrochemical applications. The most appealing aspect of using SIBs instead of LIBs, however, is the cost. Na is the fourth most abundant element in the earth's crust, and consequently, much cheaper to obtain than Li.[14-15, 33-35] While it is true that the ionic radius of Na (1.02 Å) is larger than Li's (0.76 Å), ergo comparable energy densities for SIBs will be less than for LIBs, the cost benefits of using Na is expected to outweigh the disadvantage of lower capacities. In addition, the redox potential of Na (-2.71 V versus the standard hydrogen electrode) is only 0.3 V above that of Li, making Na a fairly comparable alternative to Li from an electrochemical standpoint. As a result, SIBs are not only advisable to develop from a cost perspective, but also appear to be a feasible technology to meet future energy demands.

The overall design of SIBs is essentially the same as that of LIBs, as shown in Figure 1.1, where the main difference is that the mobile ion is Na instead of Li. The materials used as anodes and cathodes can also vary quite extensively from those of LIBs. Interestingly, it was a high-temperature, solid-state Na ionic conductor called β-alumina ($NaAl_{11}O_{17}$), which was developed in 1967,[36] that originally sparked interest in the fields of sodium electrochemistry and solid-state ionics. Because β-alumina allowed for very fast Na-ion motion, it was eventually utilized as an electrolyte in two of the earliest commercially available sodium batteries, sodium sulfur (Na–S) and ZEBRA (Zero-Emission Battery Research Activities) batteries, the former of which is still in use today.[14-15, 18] Both of these battery types are high-temperatures cells, operating at temperatures near 300 °C, which causes Na metal and the positive counter electrode to be molten. The advantages of having molten electrodes is fast ion motion through the β-alumina electrolyte and the prevention of dendrite formation. Unfortunately, there are many disadvantages to operating these cells, including maintaining a constant heating system and safety concerns of storing molten compounds, which makes these batteries impractical for widespread use.

Despite the early success of these sodium batteries, research into SIBs did not gain significant interest until only recently. After LIBs were introduced in the early 1990's, the majority of battery research focus leaned towards developing LIBs, because of their many inherent advantages, as described in the previous section. It is only after the rapid growth of LIB technology, that researchers can now see impending needs for an

alternative mobile ion in batteries. This delay in SIB research may actually turn out to be advantageous for the field, however, because many of the principles learned through the focused research attention on LIBs can be transferred to SIB development, which will effectively minimize the learning curve in SIB research.[35, 37] Therefore, based on the similarities between LIBs and SIBs many of the materials implemented in SIBs are structurally analogous to those used in LIBs.

One important difference, however, between SIBs and LIBs lies in the anode material. As discussed in the previous section, LIBs primarily use graphitic carbon as the anode material. However, graphite is not suitable for SIBs, as Na ions cannot intercalate between graphite sheets like Li ions can due to their increased ionic size.[15, 37] Consequently, the anode material for SIBs is usually disordered hard carbon, which can be obtained by the pyrolysis of sucrose, for example. Instead of intercalating between sheets, Na ions fill the pores formed as a result of the disorder in the hard carbon material. Using hard carbon anodes has made reversible capacities up to 300 mAh/g achievable. While this energy density is impressive, an issue arises with hard carbon anodes where reduced sodiated hard carbon can interact with the electrolyte to cause side reactions that ultimately hinder battery performance. As a result, the search for more suitable anode materials for SIBs still continues.

For the same reasons as in LIBs, cathode materials used in a SIBs are one of the most tunable components of the battery. Subsequently, research intended to improve SIB performance, both in terms of capacity and ion mobility, has been focused on

various cathode materials. Inspired by the burgeoning success of Li layered oxides, such as LCO, $NaMO_2$ (where M = Co, Mn, Ni, Ti, Cu, and Fe, for example) cathode materials have also been investigated as early as the 1980s.[14-15, 33, 35, 37-39] Generally, Na layered oxide materials face unique challenges as compared to their Li counterparts. Due to the larger ionic radius of Na, a greater variety of metals can substitute for M in the $NaMO_2$ structure. However, desodiation often causes irreversible phase changes in $NaMO_2$ materials, which has severely limited their acceptance into the mass market. Perhaps the most promising Na layered oxide material thus far is P2-$Na_{0.67}Mn_{1/2}Fe_{1/2}O_2$. P2 refers to a layered structure where Na in the interstitial layers reside in prismatic environments and 2 adjacent layers make up the repeating unit of in the structure. This P2-$Na_{0.67}Mn_{1/2}Fe_{1/2}O_2$ material can produce specific capacities close to 190 mAh/g, with an average potential of 3 V versus Na metal, which is outstanding for layered oxide SIB cathode materials in general. This material is also fairly optimal from a resource perspective because Na, Mn, and Fe are all relatively inexpensive and easily obtained. Combining more than one transition metal in the structure has generally been shown to improve electrochemical performance for this class of cathode materials. However, this capacity is only observed after additional Na insertion during the first cycle against a Na metal anode. Considering that Na metal is not a suitable commercial anode material for the same reasons outlined for Li metal, the feasibility of Na layered oxides is questionable. Naturally, researchers have investigated alternative ways to promote Na insertion without the need for pure Na metal, such as adding a NaN_3 salt into the

cathode which decomposes into Na and N_2 gas after the first battery charging step and increases the amount of Na in the material.[40] However, other issues, such as the volume expansion that results from this additional Na insertion, are problematic for the practical design of these batteries. It would also be more ideal to achieve even higher SIB capacities in order to truly compete with LIB applications.

To obtain SIB cathode materials with greater structural stability and competitive specific capacity, researchers have investigated alternative structure types compared to layered oxides. The most promising structures in these respects are polyanionic materials, which are generally three-dimensional open framework structures comprised of tetragonal XO_4 or trigonal XO_3 units combined with octahedral MO_6 metal coordination centres.[14-15, 35, 37] Polyanionic materials generally demonstrate much greater structural stability upon cycling since, unlike layered oxides, the crystal structure remains intact even when Na is removed. Consequently, polyanionic structures often allow low-energy Na ion diffusion pathways and the possibility to modify the mobile ion local environment in order to increase the operating voltage window. Research into SIB polyanionic cathodes was inspired by the successful olivine-type LIB polyanionic cathode material, LFP ($LiFePO_4$), introduced by Goodenough, et. al. in 1997.[41] However, the analogous Na variant, olivine-$NaFePO_4$, does not exhibit the same or even comparable ion dynamics, which is primarily due to the rather drastic change in volume that occurs in the structure between charging and discharging.

The polyanionic materials that currently hold the most promise as SIB cathodes belong to the NASICON (Na super ionic conductor) family of compounds.[15] NASICON-type structures were first introduced in 1976 as solid electrolytes comparable with β-alumina.[42] The general structure of NASICON-type materials consists of corner-sharing MO_6 and XO_4 polyhedra, which form large tunnels that promote fast Na-ion conduction.[14-15, 35] An example of a NASICON-type structure, $Na_{1.5}VPO_{4.8}F_{0.7}$, can be seen in Figure 1.2.[43] Fast ion conduction is also a requirement for cathode materials, and as a result, NASICON variants have recently developed as very promising SIB cathode materials. Amongst several potential SIB NASICON cathode materials, NVP ($Na_3V_2(PO_4)_3$) initially stood out due to its relatively large energy density (400 Wh/kg) and structural stability during cycling. NVP was introduced in 2002,[44] and at first demonstrated poor electronic conductivity. However, it has since been found that carbon coating NVP

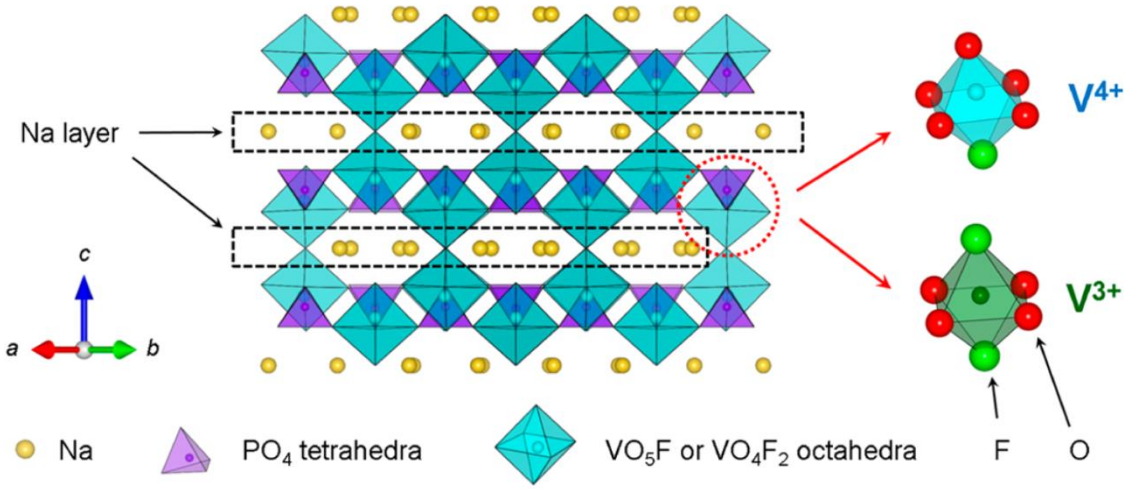

Figure 1.2 An example NASICON-type structure, $Na_{1.5}VPO_{4.8}F_{0.7}$, which show tunnels where Na ion motion is favourable. Reprinted with permission from Park, et. al. Journal of the American Chemical Society, 2013, 135 (37), 13870-13878. Copyright 2013 American Chemical Society.

nanoparticles enables 113 mAh/g of the theoretical 118 mAh/g specific capacity to be achieved, while retaining 95% of its capacity after 50 cycles. NVP is, therefore, exemplar of the potential for polyanionic materials in SIB cathode applications, especially in comparison to the structural instability of layered compounds.

Higher specific capacities, however, must be achieved in Na-based polyanionic cathodes if SIBs are to really compete with LIBs in adequately supplying the energy needs of the future. Other materials have built upon the strengths of NVP, and thus yield impressive electrochemical performance. One such material was analyzed in this thesis and will be discussed further in the following sections. The goal of research in the field of SIB cathodes is to find a particular cathode, or family of cathodes, that can outperform LIBs with reliable structural stability. While polyanionic cathodes appear to be the future of SIB cathodes in this respect, more research must be done to identify the source of capacity limitations in these materials, and hence, allow the strategic development of modified or new materials. Only then can some of the strain on Li resources be offset by the widespread commercialization of SIBs.

1.4 Introduction to the Methods and Cathodes Used in this Thesis

1.4.1 Methodology

Both LIB and SIB cathodes share the need for increased research efforts to fundamentally understand the source of capacity limitations in current materials and

identify areas where improvements can be effectively implemented. This fundamental understanding must come in both the structural and electrochemical levels, and ideally, in the relationship between the two. Many techniques have been implemented to investigate cathode materials that can yield different pieces of the LIB and SIB cathode puzzle.[45] One commonly employed technique is X-ray diffraction (XRD) which can effectively give information about the bulk material, including structural evolution and phase transformations of electrode materials, as well as SEI formation on electrode surfaces, as a result of cycling. Interestingly, many in situ and in operando XRD techniques have been developed which allow for bulk structural information of battery cathodes to be monitored in real-time during cycling. Various microscopic techniques have been also been employed, including transmission electron microscopy (TEM) and scanning transmission electron microscopy (STEM), which generally yield valuable visualizations of morphological changes and phase transformations resulting from cycling.

This thesis primarily employs the use of solid-state nuclear magnetic resonance (ssNMR) spectroscopy. ssNMR is a particularly valuable method because it is a very sensitive technique and is capable of distinguishing between ions based on their unique local environments. Analyzing battery materials is, therefore, a natural extension of this technique because both structural and mobile ions can ideally be observed. Consequently, structural evolution and phase changes that occur as result of electrochemical cycling can be observed nicely using ssNMR. Also, using specific ssNMR

techniques, mobile ion dynamics within a given material can be observed and even quantified. What is particularly valuable about using ssNMR to analyze battery cathode materials is the potential to correlate structural and ion dynamics information with each other. Much information can be gleaned about complex battery systems when ssNMR is combined with other investigative techniques, as will be frequently demonstrated throughout this thesis.

1.4.2 NMC622

The LIB cathode material that has been investigated in this work is NMC622 ($Li[Ni_{0.6}Mn_{0.2}Co_{0.2}]O_2$). NMC622 is a Ni-rich material belonging to the NMC family. As previously discussed, Ni-rich NMC materials demonstrate high capacities due to the relatively large proportion of redox-active Ni ions. NMC622 is currently considered one of the best LIB cathode materials on the market because of its high experimental specific

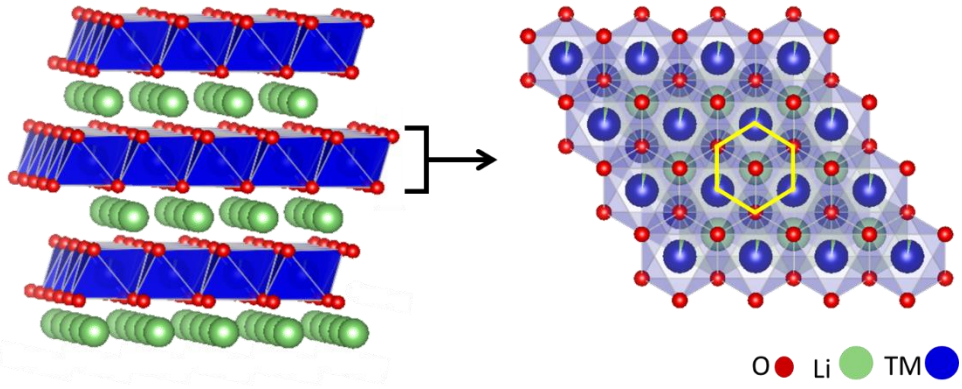

Figure 1.3 A depiction of the structure of NMC622 showing a close-up view of the transition metal (TM) layer with an example six-membered TM coordination ring to a central Li highlighted in yellow

capacity of 190 mAh/g and theoretical capacity of 277 mAh/g.[46-48] The crystal structure of NMC622 can be seen in Figure 1.3. The structure is comprised of layers of mobile Li between transition metal (TM) sheets. The general ionic arrangement within the TM sheets consists of six-membered TM rings connected by oxygen bridging to a central Li. Although these materials are widely utilized, a detailed understanding of their ionic arrangement remains elusive, which is mostly due to high disorder within the TM layers.[49-52] It is generally believed that there is partial ordering of the TMs within the layers consisting of ion clusters, the arrangement of which depends on the synthesized composition of Ni, Mn, and Co as well as the sate of charge (SOC).[52-54]

NMC622 contains both Ni^{2+} and Ni^{3+} in its pristine state.[55] While it known that Ni^{2+} will undergo oxidation to Ni^{4+} during cycling, the exact mechanism by which this occurs in Ni-rich NMC materials is still not well understood. It is currently unclear whether there is a preference for a stepwise mechanism where all Ni^{2+} is oxidized to Ni^{3+} followed by oxidation of all Ni^{3+} to Ni^{4+}, or a simultaneous mechanism where Ni^{2+} and Ni^{3+} are non-preferentially oxidized to Ni^{4+}. The purpose of this work is to help elucidate the Ni-oxidation pathway in NMC622. It is important to understand the mechanism of Ni-oxidation because Ni is the primary redox active ion in the promising family of Ni-rich NMC cathodes. This information will eventually aid researchers in designing Ni-rich materials to maximize Ni-oxidation efficiency.

1.4.3 Sodium Vanadium Fluorophosphate: $Na_3V_2(PO_4)_2F_3$

The SIB cathode studied in this work, which also demonstrates outstanding performance in its field, is NVPF ($Na_3V_2(PO_4)_2F_3$).[56-57] By examining the molecular formula, it becomes obvious that NVPF is a fluorinated derivative of NVP. The inclusion of the extremely electronegative F ions into the structure has been proven to enhance the voltage potential of the TM redox couple.[15] The reason why NVPF is considered one of the most promising SIB cathodes currently under investigation, especially for high energy density applications, is because of its high theoretical energy density (507 Wh/kg), which is higher than NVP (400 Wh/kg) and is comparable to certain commercial LIB cathodes. It generally demonstrates a high experimental specific capacity (120 mAh/g) compared to its theoretical (128 mAh/g).[35, 58] It has also recently been shown to outperform Na layered oxide materials in full cell applications in terms of specific energy, cyclability, and rate capability.[56]

NVPF crystallizes in the Amam space group, composed of V^{3+} ions at the centre of corner-sharing $V_2O_8F_3$ bioctahedra, where F ions lie along the bioctahedra axis. The bioctahedra are connected by PO_4 tetrahedra. This structure creates a NASICON-type framework with large tunnels along the [110] and [1$\bar{1}$0] directions which are ideal for Na mobility and structural stability.[58-59] The structure, shown in Figure 1.4, contains 3 unique Na sites, only two of which have been observed to participate in electrochemical cycling corresponding with the V^{3+}/V^{4+} oxidation couple.[58-60] Broux et. al.[60] showed that oxygen-substitution for F occurs in the bioctahedra ($V_2O_8F_{3-y}O_y$) as a result of synthesis conditions, which causes a V oxidation shift to 4+. This O-substitution acts to lower the average operating voltage and increase the capacity by producing higher electronic conductivity and a lowering the activation energy for Na mobility.[60-61] Ab initio calculations done on this material have also shown that additional V oxidations states are achievable, however, large Na diffusion energy barriers and highly stable Na ordering are the cause of capacity limitations. A recent and interesting development in

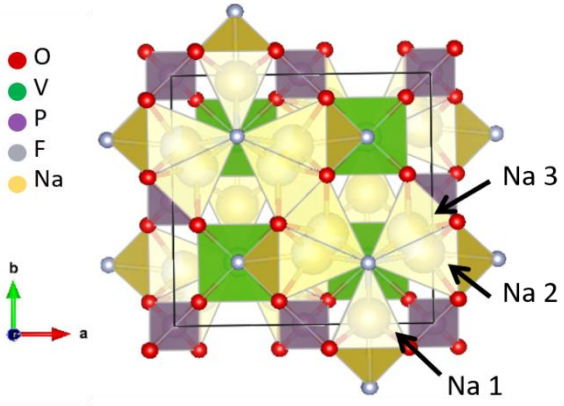

Figure 1.4 A view of the crystal structure of NVPF along the z-direction, with the three Na sites noted

the investigation of NVPF was observed by Guochun et. al. who were able to extract the third Na site during cycling from a disordered NVPF phase, which crystallized in the I4/mmm space group upon synthesis. This result demonstrates that there is still viability for developing NVPF for commercial viability. However, while the structure of NVPF been extensively investigated, the relationship between structure and ion dynamics in this promising SIB cathode material has still not been established. The work begun in this thesis seeks to understand the fundamental relationship between structure and ion dynamics in NVPF, with the aim to aid the strategic development of this material, or new SIB cathode materials, in the future.

1.5 Summary and Thesis Outline

The purpose of this thesis is to outline the work done to elucidate electrochemically relevant information about NMC622 and NVPF, which was primarily accomplished using various ssNMR techniques. The second chapter will explain some of the theory behind ssNMR, and specifically how it relates to these materials. Both NMC622 and NVPF have paramagnetic TM ions, which can greatly influence the observed NMR spectrum. The second chapter will also delve into the theory behind the density functional theory calculations that were implemented in this work. Theories behind electron paramagnetic resonance and XRD will also be explained in Chapter 2. Chapter 3 will explain details about the specific ssNMR techniques used in this work. Chapter 4 will discuss the current results and future work for the NMC622 cathode

material. Results pertaining to the NVPF family of materials which were synthesized and investigated in this work will be shown in Chapter 5. Chapter 5 will also go into detail about the future of the NVPF project, in order to act as a guide for any future work undertaken with this project. Finally, Chapter 6 will summarize the results presented throughout this thesis and the contribution of both projects.

1.6 References

1. Musango, J. K.; Brent, A. C., A conceptual framework for energy technology sustainability assessment. *Energy for Sustainable Development* **2011,** *15* (1), 84-91.
2. Babapoor, A.; Azizi, M.; Karimi, G., Thermal management of a Li-ion battery using carbon fiber-PCM composites. *Applied Thermal Engineering* **2015,** *82*, 281-290.
3. Amer, M.; Daim, T. U., Application of technology roadmaps for renewable energy sector. *Technological Forecasting and Social Change* **2010,** *77* (8), 1355-1370.
4. Jacobsson, S., Transforming the energy sector: the evolution of technological systems in renewable energy technology. *Industrial and Corporate Change* **2004,** *13* (5), 815-849.
5. Allouhi, A.; El Fouih, Y.; Kousksou, T.; Jamil, A.; Zeraouli, Y.; Mourad, Y., Energy consumption and efficiency in buildings: current status and future trends. *Journal of Cleaner Production* **2015,** *109*, 118-130.
6. Hameed, S.; Dignon, J., Global Emissions of Nitrogen and Sulfur Oxides in Fossil Fuel Combustion 1970–1986. *Journal of the Air & Waste Management Association* **1992,** *42* (2), 159-163.
7. Steffen, W.; Richardson, K.; Rockstrom, J.; Cornell, S. E.; Fetzer, I.; Bennett, E. M.; Biggs, R.; Carpenter, S. R.; de Vries, W.; de Wit, C. A.; Folke, C.; Gerten, D.; Heinke, J.; Mace, G. M.; Persson, L. M.; Ramanathan, V.; Reyers, B.; Sorlin, S., Sustainability. Planetary boundaries: guiding human development on a changing planet. *Science* **2015,** *347* (6223), 1259855.
8. Covert, T.; Greenstone, M.; Knittel, C. R., Will We Ever Stop Using Fossil Fuels? *Journal of Economic Perspectives* **2016,** *30* (1), 117-138.
9. Etacheri, V.; Marom, R.; Elazari, R.; Salitra, G.; Aurbach, D., Challenges in the development of advanced Li-ion batteries: a review. *Energy & Environmental Science* **2011,** *4* (9), 3243.
10. Gür, T. M., Review of electrical energy storage technologies, materials and systems: challenges and prospects for large-scale grid storage. *Energy & Environmental Science* **2018,** *11* (10), 2696-2767.
11. Chehouri, A.; Younes, R.; Ilinca, A.; Perron, J., Review of performance optimization techniques applied to wind turbines. *Applied Energy* **2015,** *142*, 361-388.
12. Nema, P.; Nema, R. K.; Rangnekar, S., A current and future state of art development of hybrid energy system using wind and PV-solar: A review. *Renewable and Sustainable Energy Reviews* **2009,** *13* (8), 2096-2103.
13. Parida, B.; Iniyan, S.; Goic, R., A review of solar photovoltaic technologies. *Renewable and Sustainable Energy Reviews* **2011,** *15* (3), 1625-1636.
14. Ellis, B. L.; Nazar, L. F., Sodium and sodium-ion energy storage batteries. *Current Opinion in Solid State and Materials Science* **2012,** *16* (4), 168-177.
15. Kundu, D.; Talaie, E.; Duffort, V.; Nazar, L. F., The emerging chemistry of sodium ion batteries for electrochemical energy storage. *Angew Chem Int Ed Engl* **2015,** *54* (11), 3431-48.
16. Dunn, B.; Kamath, H.; Tarascon, J.-M., Electrical Energy Storage for the Grid: A Battery of Choices. *Science* **2011,** *334* (6058), 928-935.
17. Mahmoudzadeh Andwari, A.; Pesiridis, A.; Rajoo, S.; Martinez-Botas, R.; Esfahanian, V., A review of Battery Electric Vehicle technology and readiness levels. *Renewable and Sustainable Energy Reviews* **2017,** *78*, 414-430.

18. Thackeray, M. M.; Wolverton, C.; Isaacs, E. D., Electrical energy storage for transportation—approaching the limits of, and going beyond, lithium-ion batteries. *Energy & Environmental Science* **2012,** *5* (7).
19. Li, M.; Lu, J.; Chen, Z.; Amine, K., 30 Years of Lithium-Ion Batteries. *Advanced Materials* **2018,** *30* (33).
20. Edison Batteries for New Ford Cars; Automobile Man Discusses Possibilities of New Storage System with Its Inventor. *New York Times* 1914.
21. Nitta, N.; Wu, F.; Lee, J. T.; Yushin, G., Li-ion battery materials: present and future. *Materials Today* **2015,** *18* (5), 252-264.
22. Lin, D.; Liu, Y.; Cui, Y., Reviving the lithium metal anode for high-energy batteries. *Nature Nanotechnology* **2017,** *12*, 194.
23. Wang, Q.; Ping, P.; Zhao, X.; Chu, G.; Sun, J.; Chen, C., Thermal runaway caused fire and explosion of lithium ion battery. *Journal of Power Sources* **2012,** *208*, 210-224.
24. Xu, W.; Wang, J.; Ding, F.; Chen, X.; Nasybulin, E.; Zhang, Y.; Zhang, J.-G., Lithium metal anodes for rechargeable batteries. *Energy Environ. Sci.* **2014,** *7* (2), 513-537.
25. Blomgren, G. E., The Development and Future of Lithium Ion Batteries. *Journal of The Electrochemical Society* **2017,** *164* (1), A5019-A5025.
26. Mizushima, K.; Jones, P. C.; Wiseman, P. J.; Goodenough, J. B., LixCoO2 (0<x⩽1): A new cathode material for batteries of high energy density. *Solid State Ionics* **1981,** *3-4*, 171-174.
27. Aydinol, M. K.; Kohan, A. F.; Ceder, G.; Cho, K.; Joannopoulos, J., Ab initio study of lithium intercalation in metal oxides and metal dichalcogenides. *Physical Review B* **1997,** *56* (3), 1354-1365.
28. Rougier, A.; Gravereau, P.; Delmas, C., Optimization of the Composition of the Li1 − z Ni1 + z O 2 Electrode Materials: Structural, Magnetic, and Electrochemical Studies. *Journal of The Electrochemical Society* **1996,** *143* (4), 1168-1175.
29. Wei, Y.; Zheng, J.; Cui, S.; Song, X.; Su, Y.; Deng, W.; Wu, Z.; Wang, X.; Wang, W.; Rao, M.; Lin, Y.; Wang, C.; Amine, K.; Pan, F., Kinetics Tuning of Li-Ion Diffusion in Layered Li(NixMnyCoz)O2. *Journal of the American Chemical Society* **2015,** *137* (26), 8364-7.
30. Yabuuchi, N.; Ohzuku, T., Novel lithium insertion material of LiCo1/3Ni1/3Mn1/3O2 for advanced lithium-ion batteries. *Journal of Power Sources* **2003,** *119-121*, 171-174.
31. Ren, H.; Huang, Y.; Wang, Y.; Li, Z.; Cai, P.; Peng, Z.; Zhou, Y., Effects of different carbonate precipitators on LiNi1/3Co1/3Mn1/3O2 morphology and electrochemical performance. *Materials Chemistry and Physics* **2009,** *117* (1), 41-45.
32. Sun, Y.-K.; Myung, S.-T.; Park, B.-C.; Prakash, J.; Belharouak, I.; Amine, K., High-energy cathode material for long-life and safe lithium batteries. *Nature Materials* **2009,** *8*, 320.
33. Hwang, J. Y.; Myung, S. T.; Sun, Y. K., Sodium-ion batteries: present and future. *Chemical Society reviews* **2017,** *46* (12), 3529-3614.
34. Palomares, V.; Serras, P.; Villaluenga, I.; Hueso, K. B.; Carretero-González, J.; Rojo, T., Na-ion batteries, recent advances and present challenges to become low cost energy storage systems. *Energy & Environmental Science* **2012,** *5* (3), 5884.
35. Chayambuka, K.; Mulder, G.; Danilov, D. L.; Notten, P. H. L., Sodium-Ion Battery Materials and Electrochemical Properties Reviewed. *Advanced Energy Materials* **2018,** *8* (16).
36. Yung-Fang Yu, Y.; Kummer, J. T., Ion exchange properties of and rates of ionic diffusion in beta-alumina. *Journal of Inorganic and Nuclear Chemistry* **1967,** *29* (9), 2453-2475.

37. Nayak, P. K.; Yang, L.; Brehm, W.; Adelhelm, P., From Lithium-Ion to Sodium-Ion Batteries: Advantages, Challenges, and Surprises. *Angew Chem Int Ed Engl* **2018,** *57* (1), 102-120.
38. You, Y.; Manthiram, A., Progress in High-Voltage Cathode Materials for Rechargeable Sodium-Ion Batteries. *Advanced Energy Materials* **2018,** *8* (2).
39. Han, M. H.; Gonzalo, E.; Singh, G.; Rojo, T., A comprehensive review of sodium layered oxides: powerful cathodes for Na-ion batteries. *Energy & Environmental Science* **2015,** *8* (1), 81-102.
40. Martinez De Ilarduya, J.; Otaegui, L.; López del Amo, J. M.; Armand, M.; Singh, G., NaN 3 addition, a strategy to overcome the problem of sodium deficiency in P2-Na 0.67 [Fe 0.5 Mn 0.5]O 2 cathode for sodium-ion battery. *Journal of Power Sources* **2017,** *337*, 197-203.
41. Padhi, A. K.; Nanjundaswamy, K. S.; Goodenough, J. B., Phospho-olivines as Positive-Electrode Materials for Rechargeable Lithium Batteries. *Journal of The Electrochemical Society* **1997,** *144* (4), 1188-1194.
42. Goodenough, J. B.; Hong, H. Y. P.; Kafalas, J. A., Fast Na+-ion transport in skeleton structures. *Materials Research Bulletin* **1976,** *11* (2), 203-220.
43. Park, Y.-U.; Seo, D.-H.; Kwon, H.-S.; Kim, B.; Kim, J.; Kim, H.; Kim, I.; Yoo, H.-I.; Kang, K., A New High-Energy Cathode for a Na-Ion Battery with Ultrahigh Stability. *Journal of the American Chemical Society* **2013,** *135* (37), 13870-13878.
44. Uebou, Y.; Kiyabu, T.; Okada, S.; Yamaki, J.-I., Electrochemical Sodium Insertion into the 3Dframework of Na_3M_2(PO_4)_3 (M=Fe, V). *The Reports of Institute of Advanced Material Study, Kyushu University* **2002,** *16*, 1-5.
45. Shadike, Z.; Zhao, E.; Zhou, Y.-N.; Yu, X.; Yang, Y.; Hu, E.; Bak, S.; Gu, L.; Yang, X.-Q., Advanced Characterization Techniques for Sodium-Ion Battery Studies. *Advanced Energy Materials* **2018,** *8* (17).
46. Jung, R.; Metzger, M.; Maglia, F.; Stinner, C.; Gasteiger, H. A., Chemical versus Electrochemical Electrolyte Oxidation on NMC111, NMC622, NMC811, LNMO, and Conductive Carbon. *J Phys Chem Lett* **2017,** *8* (19), 4820-4825.
47. Wang, Q.; Shen, C. H.; Shen, S. Y.; Xu, Y. F.; Shi, C. G.; Huang, L.; Li, J. T.; Sun, S. G., Origin of Structural Evolution in Capacity Degradation for Overcharged NMC622 via Operando Coupled Investigation. *ACS Appl Mater Interfaces* **2017,** *9* (29), 24731-24742.
48. Schmuch, R.; Wagner, R.; Hörpel, G.; Placke, T.; Winter, M., Performance and cost of materials for lithium-based rechargeable automotive batteries. *Nature Energy* **2018,** *3* (4), 267-278.
49. Jarvis, K. A.; Deng, Z.; Allard, L. F.; Manthiram, A.; Ferreira, P. J., Atomic Structure of a Lithium-Rich Layered Oxide Material for Lithium-Ion Batteries: Evidence of a Solid Solution. *Chemistry of Materials* **2011,** *23* (16), 3614-3621.
50. Seo, D.-H.; Lee, J.; Urban, A.; Malik, R.; Kang, S.; Ceder, G., The structural and chemical origin of the oxygen redox activity in layered and cation-disordered Li-excess cathode materials. *Nature Chemistry* **2016,** *8*, 692.
51. Shukla, A. K.; Ramasse, Q. M.; Ophus, C.; Duncan, H.; Hage, F.; Chen, G., Unravelling structural ambiguities in lithium- and manganese-rich transition metal oxides. *Nature communications* **2015,** *6*, 8711.
52. Zeng, D.; Cabana, J.; Bréger, J.; Yoon, W.-S.; Grey, C. P., Cation Ordering in Li[NixMnxCo(1–2x)]O2-Layered Cathode Materials: A Nuclear Magnetic Resonance (NMR), Pair

Distribution Function, X-ray Absorption Spectroscopy, and Electrochemical Study. *Chemistry of Materials* **2007,** *19* (25), 6277-6289.
53. Harris, K. J.; Foster, J. M.; Tessaro, M. Z.; Jiang, M.; Yang, X.; Wu, Y.; Protas, B.; Goward, G. R., Structure Solution of Metal-Oxide Li Battery Cathodes from Simulated Annealing and Lithium NMR Spectroscopy. *Chemistry of Materials* **2017,** *29* (13), 5550-5557.
54. Yan, P.; Xiao, L.; Zheng, J.; Zhou, Y.; He, Y.; Zu, X.; Mao, S. X.; Xiao, J.; Gao, F.; Zhang, J.-G.; Wang, C.-M., Probing the Degradation Mechanism of Li2MnO3 Cathode for Li-Ion Batteries. *Chemistry of Materials* **2015,** *27* (3), 975-982.
55. Tian, C.; Nordlund, D.; Xin, H. L.; Xu, Y.; Liu, Y.; Sokaras, D.; Lin, F.; Doeff, M. M., Depth-Dependent Redox Behavior of LiNi0.6Mn0.2Co0.2O2. *Journal of The Electrochemical Society* **2018,** *165* (3), A696-A704.
56. Mariyappan, S.; Wang, Q.; Tarascon, J. M., Will Sodium Layered Oxides Ever Be Competitive for Sodium Ion Battery Applications? *Journal of The Electrochemical Society* **2018,** *165* (16), A3714-A3722.
57. Yan, G.; Mariyappan, S.; Rousse, G.; Jacquet, Q.; Deschamps, M.; David, R.; Mirvaux, B.; Freeland, J. W.; Tarascon, J. M., Higher energy and safer sodium ion batteries via an electrochemically made disordered Na3V2(PO4)2F3 material. *Nature communications* **2019,** *10* (1), 585.
58. Zhu, C.; Wu, C.; Chen, C.-C.; Kopold, P.; van Aken, P. A.; Maier, J.; Yu, Y., A High Power–High Energy Na3V2(PO4)2F3 Sodium Cathode: Investigation of Transport Parameters, Rational Design and Realization. *Chemistry of Materials* **2017,** *29* (12), 5207-5215.
59. Bianchini, M.; Fauth, F.; Brisset, N.; Weill, F.; Suard, E.; Masquelier, C.; Croguennec, L., Comprehensive Investigation of the Na3V2(PO4)2F3–NaV2(PO4)2F3 System by Operando High Resolution Synchrotron X-ray Diffraction. *Chemistry of Materials* **2015,** *27* (8), 3009-3020.
60. Broux, T.; Bamine, T.; Fauth, F.; Simonelli, L.; Olszewski, W.; Marini, C.; Ménétrier, M.; Carlier, D.; Masquelier, C.; Croguennec, L., Strong Impact of the Oxygen Content in Na3V2(PO4)2F3–yOy (0 ≤ y ≤ 0.5) on Its Structural and Electrochemical Properties. *Chemistry of Materials* **2016,** *28* (21), 7683-7692.
61. Broux, T.; Bamine, T.; Simonelli, L.; Stievano, L.; Fauth, F.; Ménétrier, M.; Carlier, D.; Masquelier, C.; Croguennec, L., VIV Disproportionation Upon Sodium Extraction From Na3V2(PO4)2F3 Observed by Operando X-ray Absorption Spectroscopy and Solid-State NMR. *The Journal of Physical Chemistry C* **2017,** *121* (8), 4103-4111.

Chapter 2: Magnetic Resonance Techniques and Calculation Methods

2.1 Introduction

The inherent complexity of various cathode materials for alkali ion batteries was established in Chapter 1, as well as many of the ongoing research efforts to develop and understand these materials. Researchers have applied many different techniques to elucidate the mechanisms that are responsible for both superior performance and capacity limitations within cathode materials, in order to enable the informed development of new cathode materials.[1] ssNMR has proven to be an exemplary technique because of its uncommon ability to distinguish ions within a structure based on their unique environments. This feature of ssNMR is particularly valuable for studying cathode materials because ion motion throughout the battery is responsible for the observed electrochemical performance.

There are two primary veins where ssNMR can supply insights about cathode materials: ionic arrangement within the crystal structure and ion dynamics. As previously discussed, the structures in LIB layered oxide cathodes are relatively complicated and disordered. The ionic compositions and local ordering which can exist in these materials, however, is known to be very determinative of their electrochemical performance. Additionally, structural evolution can occur in both SIB and LIB cathodes during charge and discharge. The ability of ssNMR to potentially distinguish ions based

on their local environments can, therefore, be particularly useful for structural elucidation of these materials. Specifically, a well-established pulse sequence called the Hahn ECHO can help mitigate some of the dispersive effects of nuclei in a magnetic field, producing spectra that are more easily analyzable.[2]

Ion dynamics are another area where ssNMR can be very informative. The relationship between the crystal structure and ion motion in cathode materials is very important in understanding the structural properties responsible for capacity limitations. Certain ssNMR techniques are able to illuminate this relationship, such as selective inversion (SI) and two-dimensional exchange spectroscopy (EXSY), and have previously been successfully applied to alkali ion cathodes.[3-7] EXSY was primarily used throughout this work, as it is the simpler of the two methods to implement and was able to supply many of the desired insights into Na ion dynamics of the materials.

Density Functional Theory (DFT) calculations were also performed in conjunction with ssNMR experiments to help determine the structural interpretation of experimental spectra, a method that has been successfully applied to various other cathode materials.[8-10] There can be multiple different signals resulting from a variety of similar Na environments that appear as one broad peak in NMR spectra of complicated cathode materials. DFT calculations can be used to determine an optimized structure for a particular material from which the NMR shift can be calculated and compared to experimental spectra. DFT calculations, therefore, allow for direct a correlation between crystal structures and NMR spectra.

Electron paramagnetic resonance (EPR) was yet another technique used to investigate some of the cathode materials analyzed in this work.[11-13] EPR is valuable for application in cathode analysis because these materials often contain paramagnetic transition metals as the redox-active centre. EPR, therefore, has the potential to reveal information about the cathode's redox behaviour by directly monitoring the redox-active ion. EPR is particularly complimentary to NMR as it takes advantage of the paramagnetic nature of cathode materials that otherwise makes them difficult to analyze using ssNMR, which will be outlined in more detail in the following sections.

Before these various techniques can be outlined in detail, however, the nuclear response of these materials in an external magnetic field must be discussed. These characteristics determine much of the experimentally observed behaviour. This chapter will, therefore, first consider some basic aspects of the nuclei being investigated, before going into a more detailed discussion of the various techniques employed in this study.

2.2 A Brief Introduction to Relevant NMR Theory

To fully grasp the impending discussion of the background and techniques used throughout this work, it is important to first understand some of the basic principles regarding how a nucleus behaves in a magnetic field. A given nucleus has a magnetic moment, resulting from the combination of the spin angular momenta of the individual protons and neutrons that make up that nucleus.[14] The overall nuclear spin quantum number is denoted as I, which is $(2I + 1)$-fold degenerate at a given unperturbed spin

state (the ground state). When nuclei are placed in a magnetic field, the spin state degeneracy is broken, and the nuclear spin energy levels are split in an effect called nuclear Zeeman splitting. NMR-active nuclei, therefore, are nuclei that have a non-zero nuclear spin ground state ($I \neq 0$), so they can experience Zeeman splitting. In response to an external magnetic field (B_0) the spins will tend to align in the lowest energy state, parallel to B_0, and precess about B_0 at a characteristic frequency called the Larmor frequency (ω_0). The Larmor frequency is a function of the nuclear gyromagnetic ratio (γ) and the strength of the external magnetic field, B_0, as shown in Equation 2.1.

$$\omega_0 = \gamma B_0 \qquad \text{(Equation 2.1)}$$

In addition to the nuclear magnetic moment, electrons surrounding the nucleus also have magnetic moments that will respond to an external magnetic field.[14-15] The B_0 field induces a current in the electron cloud surrounding a nucleus, which then generates a magnetic field in opposition to B_0. Consequently, the effective magnetic field felt by nuclei will be the sum of B_0 and the local magnetic field induced by the circulation of the valence electrons within the molecule. This interaction results in the chemical shift, which determines where signals lie in the experimental spectrum. Any differences in the electron density surrounding various nuclei will result in dissimilar chemical shifts, corresponding to different signals in the observed spectra.

The signals in an NMR spectrum are obtained by use of radio frequency (r.f.) pulses. Conventionally, B_0 is defined in a typical cartesian coordinate system as aligning with the z-axis. When a r.f. pulse is applied with the appropriate frequency and length of time along the y-axis to nuclear spins aligned with B_0 (referred to as longitudinal magnetization), the nuclear spins are flipped by $\pi/2$ radians about the y-axis, resulting in net spin polarization aligned along the x-axis. The xy-plane is denoted as the transverse plane. Once in the transverse plane, the net nuclear spin then begins to precess at the Larmor frequency. Due to slight inhomogeneity in the individual nuclear magnetic moments that make up the net magnetization, precession in the transverse plane will eventually decay to zero. The time scale for this loss of magnetization within the transverse plane is referred to as the transverse relaxation time, T_2. Similarly, the time required for the net nuclear magnetization to return from the transverse plane to equilibrium (aligned with B_0) is called the spin-lattice relaxation time, T_1. Both T_2 and T_1 are inherent properties of each unique nucleus in a given sample. The general process of an NMR experiment described herein is depicted in Figure 2.1.

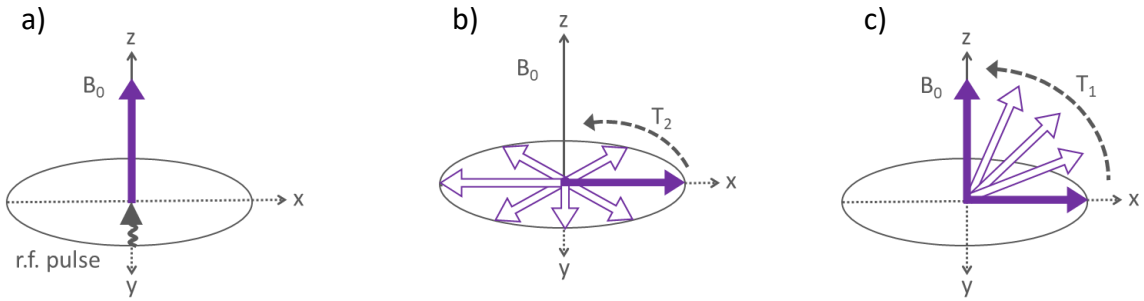

Figure 2.1 The generalized behaviour of net nuclear spin magnetization (solid purple arrow) in a magnetic field (B_0). a) At the start of the experiment, net magnetization is aligned with the B_0 and a r.f. pulse (solid grey arrow) is applied. b) Net magnetization is transferred to the transverse plane where precession (open purple arrows) is governed by T_2. c) The transverse magnetization relaxes back to equilibrium according to T_1.

The NMR experiment described thus far, is a generic representation of nuclei in a magnetic field. However, there are certain important differences between the interactions experienced by nuclei in a solid sample and a solution sample that can greatly influence the observed spectrum. This work is primarily concerned with nuclei in a solid sample. Unlike in solution samples, where molecular tumbling average out any orientation dependent interactions, in solid samples the relatively stationary nuclei will experience all inter-nuclear interactions resulting in extremely broad peaks.[16] There are two particularly impactful interactions in the solid state. The first is dipolar coupling, which refers to the through-space interaction of the magnetic moments of two nuclear spins. The dipolar coupling that can occur between two different spins, I and S, is described by the Hamiltonian (H_{IS}) in Equation 2.2. The terms I_z and S_z correspond to the longitudinal component of the spin magnetization, while $(cos^2\theta - 1)$ is the orientation dependent term where θ is the angular orientation of the internuclear

vector with respect to the direction of B_0. The d term is the dipolar coupling constant, defined in Equation 2.3, where γ is the gyromagnetic ratio of spins I and S, ħ is Planck's constant, r_{IS} is the internuclear distance, and μ_0 is the permeability of free space. Dipolar coupling causes peak broadening in ssNMR spectra.

$$H_{IS} = -d(cos^2\theta - 1)I_Z S_Z \qquad \text{(Equation 2.2)}$$

$$d = \left(\frac{\mu_0}{4\pi}\right)\frac{\hbar\gamma_I\gamma_S}{r_{IS}^3} \qquad \text{(Equation 2.3)}$$

Another important interaction that contributes to peak broadening is chemical shift anisotropy (CSA). The general expression describing the chemical shift Hamiltonian (H_{CS}) is shown in Equation 2.4. Again, this equation shows an orientation dependence with respect to B_0 through the $(cos^2\theta - 1)$ term. The $\gamma B_0 I_Z$ term refers to the resonant frequency of the longitudinal component of spin I magnetization, similar to what was seen in Equation 2.1. The observed chemical shift is determined by H_{CS} which contains a CSA orientation dependent term (δ_{CSA}) and an isotropic term which is independent of orientation (δ_{iso}). The best way to describe the effect CSA has on the observed spectrum is to visualize each crystallite in a powder sample as an ellipsoid, where the orientation of the ellipsoid with respect to B_0 determines at which position (chemical shift) the signal appears in the observed spectrum. In a powdered sample one can assume infinite crystallite orientations which ultimately results in the appearance of a single broad peak containing all crystallite signals.

$$H_{CS} = \gamma B_0 I_Z[\delta_{iso} + {}^1\!/_2\, \delta_{CSA}(3cos^2\theta - 1)] \qquad \text{(Equation 2.4)}$$

Although these various orientation dependent nuclear interactions contain a great deal of information, such as nuclear distances and the orientation of crystallites within a solid sample, the peak broadening they induce can make the resulting ssNMR spectra very difficult to analyze. However, it was found that both dipolar coupling and CSA can be eliminated in ssNMR by using magic angle spinning (MAS). The MAS process involves very quickly spinning a sample that is tilted at the "magic" angle (θ = 54.74°). The effect MAS has on orientation dependent interactions can be understood by re-examining H_{IS} and H_{CS}. As previously discussed, both the H_{IS} and H_{CS} contain the orientation dependent term $(cos^2\theta - 1)$, which goes to zero when θ = 54.74°, essentially eliminating dipolar coupling effects and the CSA term (δ_{CSA}) from H_{CS}. As a result, only the δ_{iso} remains for chemical shift determination. Fast spinning is necessary to average the CSA of all crystallites in the sample so they essentially behave as a single ellipsoid, which can then be uniformly affected by MAS. Any remnants of anisotropic interactions will appear in the spectrum as spinning sidebands (SSBs), which appear at regular intervals corresponding with the MAS speed from the isotropic signal.[17] Figure 2.1 shows a series of experimental ^{13}C labeled (10%) glycine ssNMR spectra collected at various MAS speeds, which can be compared to a simulated static spectrum. As the MAS

speed is steadily increased the effect of orientation dependent terms is decreased resulting narrowing peak width.

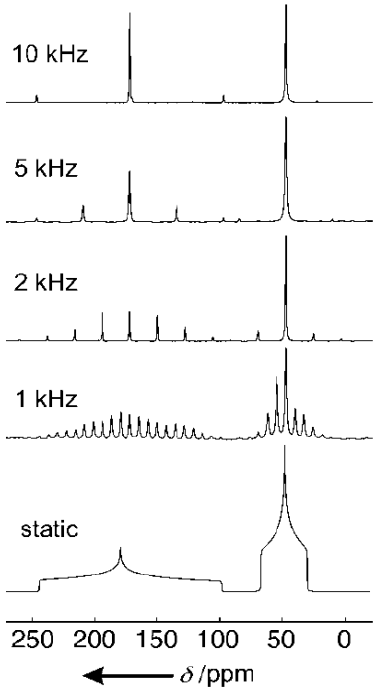

Figure 2.2 ^{13}C ssNMR spectra (at 125 MHz) of a powder 10% ^{13}C uniformly labeled glycine sample at various MAS spinning speeds compared to a simulated static spectrum. Reprinted with permission from Laws, D. D.; Bitter, H.-M. L.; Jerschow, A., Solid-State NMR Spectroscopic Methods in Chemistry. Angewandte Chemie International Edition, *2002,* 41 *(17), 3096-3129. Copyright 2002 American Chemical Society.*

2.3 A Comparison of Relevant ssNMR Parameters Between ^{7}Li and ^{23}Na Nuclei

In attempting to gain a comprehensive understanding of alkali ion cathode materials, the NMR-active mobile ions of both LIBs and SIBs, ^{6,7}Li and ^{23}Na respectively, have been extensively studied.[3-5, 18-24] In this work as well, both ^{7}Li and ^{23}Na nuclei were

probed. There are fundamentally more similarities between these nuclei than there are differences. Table 2.1 shows various NMR-relevant parameters for these nuclei.

Table 2.1 Select NMR-relevant parameters for ^{6,7}Li and ^{23}Na nuclei. These values were taken from Harris, et. al., Pure and Applied Chemistry (2001). [25]

Nucleus	Natural abundance (%)	Nuclear spin, I	Gyromagnetic Ratio, γ (10^7 rad s^{-1} T^{-1})	Quadrupole Moment, Q (fm^2)
^{6}Li	7.59	1	3.937	0.0808
^{7}Li	92.41	3/2	10.397	4.01
^{23}Na	100	3/2	7.08	10.4

Both Li and Na are quadrupole nuclei, meaning that the electronic charge is asymmetrically distributed around the nucleus.[14, 16] Asymmetric electron density surrounding a given nucleus (when $I > 1/2$) will interact with the nucleus and induce a nuclear electric quadrupole moment, Q. The effect of nuclear quadrupole coupling is further shifting of Zeeman split energy levels to where the resulting transitions have different energies relative to each other. The energy of the central transition (CT), corresponding to the isotropic chemical shift, does not change from this first order quadrupole interaction, however, a new set of peaks, called satellite transitions (ST), appear due to the additional $\pm\left(\frac{1}{2} \rightarrow \frac{3}{2}\right)$ transitions. A schematic of the first order quadrupole splitting for a $I = 3/2$ nucleus, as well as the corresponding simulated spectrum, can be seen in Figure 2.3a and 2.3b, respectively.[26] The term ω_0 is the first

order quadrupolar coupling, which determines the frequency shift of the STs from the CT in the observed NMR spectrum. A given nucleus will resonate over a range of frequencies, which is dependent on the magnitude of Q. High Q values result in a relatively large distribution of resonant frequencies, corresponding with a wider quadrupole lineshape. When Q is sufficiently large, the energy difference between transitions will again be shifted due to second order quadrupole effects, which causes even broader spectral widths.[14, 27] While the position of the CT is not impacted by first order quadrupole interactions, it will be altered by a second order interaction.[26] It should also be noted that both high B_0 and fast MAS can help reduce broadening in quadrupole lineshapes.[27]

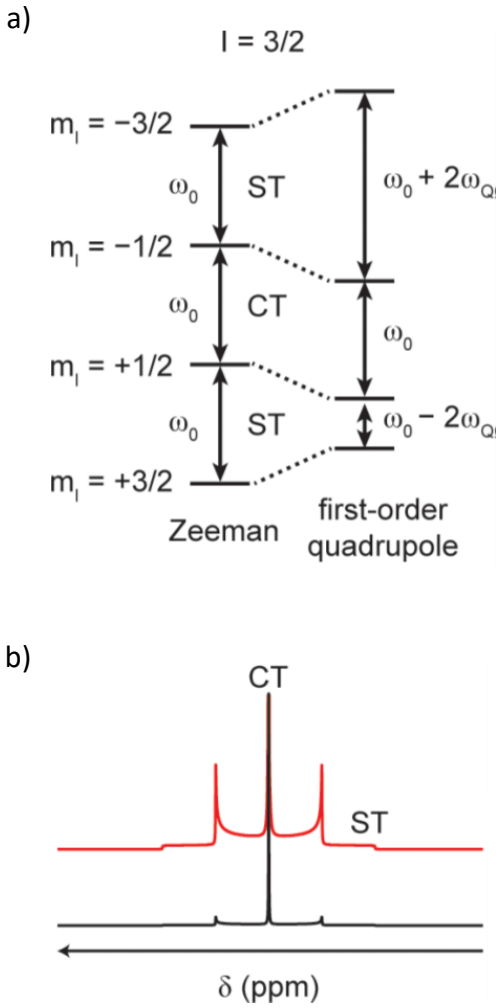

Figure 2.3 a) A schematic of an $I = 3/2$ *nuclear spin splitting as a result of Zeeman and 1st order quadrupole interactions which produce a central transition (CT) and a pair of satellite transitions (ST)`. b) The corresponding simulated ssNMR powder spectrum. Reprinted (adapted) with permission from Ashbrook, S. E.; Sneddon, S., New methods and applications in solid-state NMR spectroscopy of quadrupolar nuclei.* Journal of the American Chemical Society, *2014,* 136 *(44), 15440-56. Copyright 2014 American Chemical Society.*

According to Table 2.1, the quadrupole moment is the most striking difference between the three nuclei. When examining the difference between ^{6}Li and ^{7}Li, it is

apparent that Q is smaller for ^{6}Li, however, its natural abundance is much lower. As well, generally the quadrupole lineshapes of both ^{6}Li and ^{7}Li salts are not evident under typical MAS.[28] Therefore, in the results presented throughout this thesis, ^{7}Li ssNMR was performed to take advantage of its greater natural abundance. The ^{23}Na nucleus has the largest Q so its quadrupole lineshape is expected to be the broadest of all three nuclei. Interestingly, in this work synthesized NVPF was initially analyzed in a 4.7 T magnetic field, as shown in Figure 2.4b, and the peak had a distinct quadrupole lineshape where the broadened CT indicates that second order quadrupole broadening has occurred. In contrast, the effects of quadrupole broadening were greatly diminished for the same sample at a higher B_0 of 11.7 T, shown in Figure 2.4a. Accordingly, all further ^{23}Na ssNMR spectra were collected in a 11.7 T magnetic field, where the primary chemical shift determinate were paramagnetic effects, which will be further discussed in the following section.

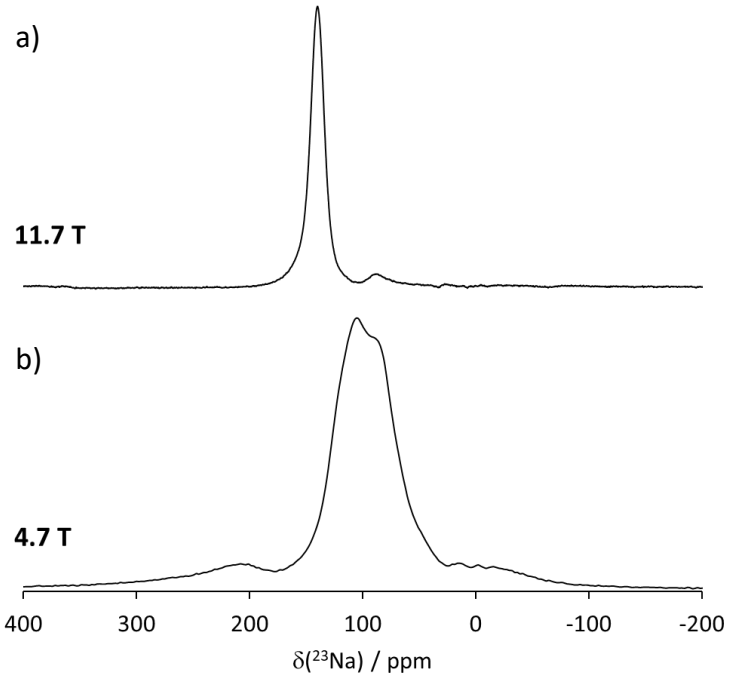

Figure 2.4 The ^{23}Na ssNMR spectra of NVPF in a) 11.7 T magnetic field (30 kHz MAS) which is a narrowed lineshape compared to the same sample in a b) 4.7 T (60 kHz MAS) magnetic field whisch shows a distinct quadrupole linshape

2.4 Challenges to studying paramagnetic materials using NMR

Alkali ion cathode materials are generally inherently difficult to analyze using ssNMR because the redox active metal in these materials are often paramagnetic transition metals.[10, 20, 29] Paramagnetic ions have unpaired electrons. As previously discussed with respect to quadrupole coupling, electronic spins will interact with nuclear spins in a magnetic field (hyperfine coupling), and consequently, contribute to the observed experimental shift. This contribution is known as the hyperfine shift. This hyperfine shift dominates many features of the observed ssNMR spectrum, primarily by

broadening spectral peaks. Because the relaxation rate of perturbed electron spins in a magnetic field is so much shorter than the nuclear T_1, an outcome of hyperfine coupling is also significantly faster nuclear T_1 values compared to diamagnetic systems. The through-bond transfer of unpaired electron spin density to the nuclei of interest is referred to as the Fermi-contact interaction. Similar to internuclear dipolar coupling, a through-space interaction can occur between unpaired electron spins and a given nucleus, referred to as the pseudocontact shift, which also contributes to peak broadening.[29] MAS is able to minimize the broadening effects of these various interactions. In contrast to quadrupole coupling parameters, however, high B_0 fields actually linearly scale electron−nuclear anisotropic interactions, increasing peak broadening at higher B_0 fields.[30] The various methods used to compensate for paramagnetic peak broadening in NMR spectra of the cathode samples analyzed in this thesis will be outlined in Chapters 3 and 4.

2.5 The Spin ECHO NMR Experiment

In order to ascertain the structural information that ssNMR spectra can potentially provide, various ssNMR techniques can be used to obtain clear isotropic spectra. One of the potential issues that can arise in NMR experiments occurs during precession in the transverse plane where interactions between precessing nuclear spins, or energy loss to the lattice as thermal energy, can cause the spins to precess at different rates. This dephasing effect will lower the amount of observable signal and cause shortened T_2

rates. In order to correct for dephasing, Erwin Hahn suggested the Hahn ECHO pulse sequence in 1950.[2] Following an initial 90° pulse which flips the longitudinally aligned nuclear spins into the transverse plane, a 180° pulse is applied that symmetrically flips the spins within the transverse plane so they re-phase with one another. This pulse sequence is visualized in Figure 2.5.

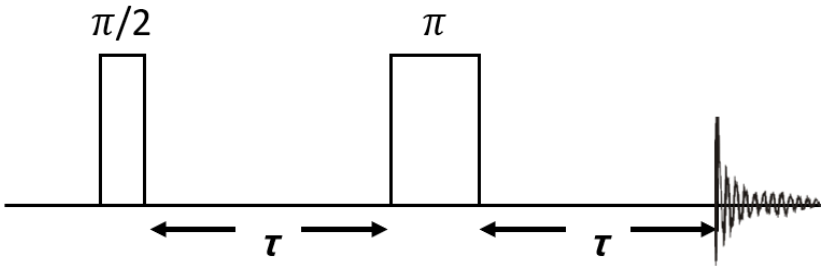

Figure 2.5 The Hahn ECHO pulse sequence which includes a re-phasing π pulse

2.6 The Two-Dimensional Exchange Spectroscopy NMR Experiment

Two-dimensional exchange spectroscopy (EXSY) is a NMR technique which is used to elucidate site-to-site dynamics.[14, 31] The pulse sequence is shown in Figure 2.6. The first 90° pulse flips nuclear spins into the transverse plane. The following τ_1 delay is called the frequency labeling period, where the precession of non-exchanging spins is identified, corresponding to the diagonal peaks. The next 90° pulse flips the spins back into the longitudinal plane. The last delay is referred to as the mixing time (τ_m), which is the time period where magnetization loss due to an exchange process can occur. The

last 90° pulse flips the resulting magnetization back into the transverse plane for observation.

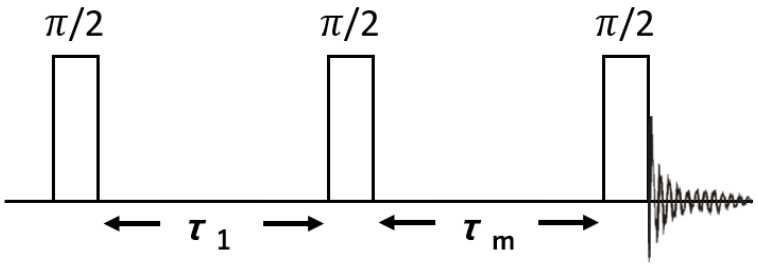

Figure 2.6 The EXSY pulse sequence which includes a mixing time (τ_m) where exchange processes can occur

The result of an EXSY experiment is a two-dimensional spectrum where peaks lying along the diagonal correspond the one-dimensional spectrum. Off-diagonal peaks indicate that an exchange process has taken place between sites on the diagonal. A schematic representation of an EXSY spectrum can be seen in Figure 2.5. The outcome of an EXSY experiment is both the frequency (position) and amplitude (intensity) of diagonal and off-diagonal peaks. A cross peak will appear at a position in the spectrum determined by the frequency coordinates of each diagonal peak between which exchange has occurred. For example, the cross peaks in the spectrum in Figure 2.7 have coordinates of frequencies (Ω_A^0, Ω_B^0) and (Ω_B^0, Ω_A^0) corresponding to exchange between sites A and B with coordinates of (Ω_A^0, Ω_A^0) and (Ω_B^0, Ω_B^0) respectively. This exchange process can be either a through-space magnetization transfer or site-to-site ion exchange. The EXSY pulse sequence is a particularly important technique to have in the

NMR toolkit because it can be used quantitively. The rate constants for the observed exchange processes can be extracted by examining the intensity growth of cross-peaks as a function of mixing time. The EXSY technique was used extensively throughout this thesis to probe ion dynamics in SIB cathode materials.

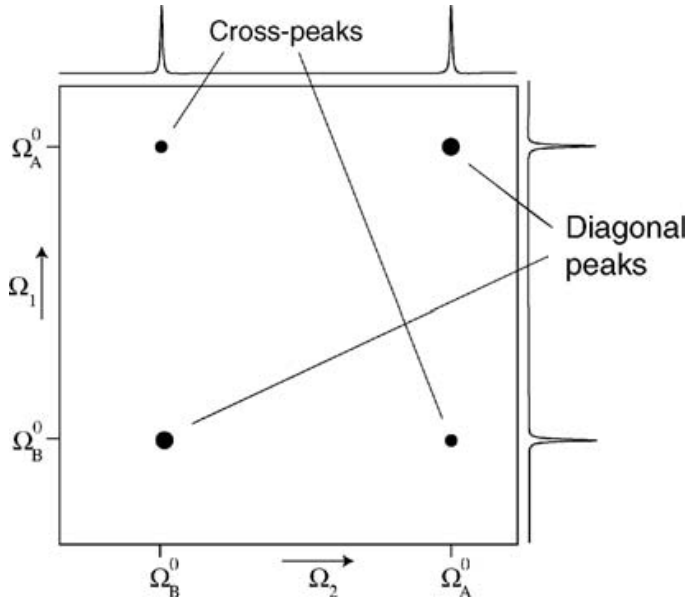

Figure 2.7 A schematic representation of an EXSY spectrum. Diagonal and cross peaks are labeled. The Ω_1 and Ω_2 axes correspond to the indirect and direct dimensions respectively. Reprinted with permission from Levitt, M. H., Spin dynamics basics of nuclear magnetic resonance*. 2nd ed. ed.; John Wiley & Sons Ltd: Chichester, West Sussex, England; Hoboken, N.J., 2008. Copyright 2008 John Wiley and Sons.*

2.7 *Ab Initio* Calculations of Paramagnetic NMR Shifts

One of the greatest challenges to studying paramagnetic materials using ssNMR is peak broadening, as previously discussed in Section 2.4. In these instances, combining ssNMR with computational methods can be an effective means to extract meaningful

information from paramagnetic systems. Many successful studies have employed *ab initio* calculation methods to model paramagnetic systems and their corresponding ssNMR spectra.[8-10, 32-33] Paramagnetic broadening in the ssNMR spectra of the SIB cathode materials investigated in this work, necessitated the implementation of similar calculation methods to understand the structural correlation with observed experimental spectra.

The primary determinate of the observed chemical shift in paramagnetic cathode materials is the amount of unpaired electron spin density transferred to the nucleus of interest through hyperfine coupling.[8] Consequently, to calculate the expected chemical shift of a species in a given paramagnetic material the hyperfine coupling must be determined. In this work, *ab initio* calculations were performed which calculated the hyperfine coupling constant, A, which is associated with the amount of electron spin density transferred to the nucleus of interest.[29, 32] The hyperfine coupling was comprised only of the calculated Fermi contact result, as contributions from through-space interactions were considered negligible in comparison to the Fermi contact.[32, 34] The hyperfine coupling constant, A, is then used to calculate the total electron density surrounding a given nucleus (ρ) by Equation 2.5, where $S(tot)$ is the total number of unpaired electrons in the unit cell, γ_N is the gyromagnetic ratio of the nucleus of interest, and the term *c* is a combination of various physical constants. Once the electron density, ρ, is found the NMR chemical shift can be calculated by incorporating experimentally measured magnetic susceptibility information.

$$\rho = \frac{A \,.\, S(tot)}{\gamma_N \,.\, c} \qquad \text{(}\textit{Equation 2.5}\text{)}$$

The hyperfine coupling constant is calculated by determining the unpaired electron density within the crystal structure. In this work, electron densities were calculated using density functional theory (DFT). Conceptually, DFT attempts to find the ground state energy solution to the one-particle Schrödinger equation, from which it is possible to know the electron density.[35] An electron density solution is found when the energy of the overall functional is minimized, which is only accomplished when an exchange-correlation functional (ECF), which describes components of electron interactions, is included in the calculations. An exact form of the ECF is unknown, however, an approximate ECF can be found by assuming electron density occurs as a uniform gas. This technique is called the local density approximation (LDA). The ECF used in this work, known as the generalized gradient approximation (GGA), includes an additional term to model the local gradient within the electron density, thus better accounting for inhomogeneity within the electron density gas.[35] The component of the GGA functional that includes electron gradient information is the Perdew–Burke–Ernzerhof (PBE) functional.[36] Consequently, this approach is more representative of real systems than LDA and is not too computationally expensive.

Finding the electron density of all atomic orbitals in an extended lattice, such as in a crystal structure, would be computationally unfeasible.[35] The electron density can, therefore, be modeled by plane waves over a finite energy range. However, even this method can be computationally complicated. One way to minimize the required calculations is to define an approximate plane wave basis set for core electrons, which is known as a pseudopotential. Treating core electrons in this way is referred to as the frozen core approximation. This approximation is valid because core electrons in reality have very little impact compared to valence electrons on a material's physical properties.[35] The chosen pseudopotentials, therefore, define the energy cutoff for the system. The most superior set of pseudopotentials currently available is the projector augmented-wave (PAW) method, as it produces the most accurate results compared to all-electron modeling while still maintaining computational efficiency.[37-38]

The principles of DFT described herein are foundational to the calculations performed on SIB cathodes, which are outlined in Chapter 4. The efficacy of these calculations to model paramagnetic systems, based on a first-principles understanding of electron-nuclear interactions, made them invaluable to the interpretation of paramagnetic ssNMR spectra in this work.

2.8 Electron Paramagnetic Resonance

Electron paramagnetic resonance (EPR) spectroscopy is a fascinating technique which can only observe paramagnetic species. EPR has accordingly been applied to the

analysis of various paramagnetic cathode materials.[11-13, 39] EPR is well suited to the study of these materials because it has the potential to both determine the oxidation state and local environment, with less ambiguity than NMR, of the paramagnetic transition metals that are usually present in cathode materials. In this work, EPR was used to investigate the paramagnetic redox-active centre in various SIB cathode materials.

EPR is a technique very similar in theory to NMR. Similarities between the two techniques include the use of electromagnetic radiation and a magnetic field to induce Zeeman splitting in the magnetic moment of a particle.[40-41] However, several differences between the two methods have allowed EPR to standout as a valuable technique for studying paramagnetic systems. In a typical EPR experiment, steady microwave radiation is applied to a paramagnetic sample at the energy associated with the energy difference between the Zeeman splitting of an unpaired electron magnetic moment. The surrounding magnetic field is then varied over a given range. A signal is observed in the EPR spectrum when the magnetic field induces a transition within the Zeeman-split energy levels. The observed EPR spectrum can appear as single line surrounded by any number of additional lines. The total set of observed lines is referred to as the hyperfine structure of the spectrum. The hyperfine structure results from interactions of the electron spins and the nuclear spins. EPR is, therefore, a unique method which is valuable for potentially understanding details about the paramagnetic transition metals present in cathode materials, by distinguishing ions based on their surrounding environment and oxidation state (the number of unpaired electrons). EPR was,

consequently, applied to the study of various SIB cathodes in this work, which will be discussed in more detail in Chapter 4.

2.9 Summary

This chapter outlined the basic theory that drives NMR experiments. Certain characteristics of alkali ion cathode materials were then discussed in relation to their effects on the observed NMR spectrum. The features of ^{6,7}Li and ^{23}Na nuclei were shown, and the differences pertaining to the quadrupole nature of the nuclei were outlined. The ^{23}Na nucleus was shown to experience the largest quadrupole effects. The other dominating factor in NMR of cathode materials, the presence of paramagnetism, was explained. The types of unpaired electron spin density transfer that can occur were explored. Specific NMR techniques were then outlined in relation to extracting structural (Hahn ECHO) and dynamics (EXSY) information from cathode materials. The variation of DFT calculations used throughout this work was then explained. Finally, the basic concepts of EPR and its relation to the materials analyzed in this thesis were outlined.

2.10 References

1. Shadike, Z.; Zhao, E.; Zhou, Y.-N.; Yu, X.; Yang, Y.; Hu, E.; Bak, S.; Gu, L.; Yang, X.-Q., Advanced Characterization Techniques for Sodium-Ion Battery Studies. *Advanced Energy Materials* **2018,** *8* (17).
2. Hahn, E. L., Spin Echoes. *Physical Review* **1950,** *80* (4), 580-594.
3. Cahill, L. S.; Chapman, R. P.; Britten, J. F.; Goward, G. R., 7Li NMR and Two-Dimensional Exchange Study of Lithium Dynamics in Monoclinic Li3V2(PO4)3. *The Journal of Physical Chemistry B* **2006,** *110* (14), 7171-7177.
4. Davis, L. J. M.; Ellis, B. L.; Ramesh, T. N.; Nazar, L. F.; Bain, A. D.; Goward, G. R., 6Li 1D EXSY NMR Spectroscopy: A New Tool for Studying Lithium Dynamics in Paramagnetic Materials Applied to Monoclinic Li2VPO4F. *The Journal of Physical Chemistry C* **2011,** *115* (45), 22603-22608.
5. Davis, L. J. M.; Goward, G. R., Differentiating Lithium Ion Hopping Rates in Vanadium Phosphate versus Vanadium Fluorophosphate Structures Using 1D 6Li Selective Inversion NMR. *The Journal of Physical Chemistry C* **2013,** *117* (16), 7981-7992.
6. Davis, L. J. M.; Heinmaa, I.; Goward, G. R., Study of Lithium Dynamics in Monoclinic Li3Fe2(PO4)3using6Li VT and 2D Exchange MAS NMR Spectroscopy†. *Chemistry of Materials* **2010,** *22* (3), 769-775.
7. Smiley, D. L.; Tessaro, M. Z.; He, X.; Goward, G. R., Correlation of Electrochemical Performance with Lithium Environments and Cation Dynamics in Li2(Mn1–yFey)P2O7 using 6Li Solid-State NMR. *The Journal of Physical Chemistry C* **2015,** *119* (29), 16468-16474.
8. Bamine, T.; Boivin, E.; Boucher, F.; Messinger, R. J.; Salager, E.; Deschamps, M.; Masquelier, C.; Croguennec, L.; Ménétrier, M.; Carlier, D., Understanding Local Defects in Li-Ion Battery Electrodes through Combined DFT/NMR Studies: Application to LiVPO4F. *The Journal of Physical Chemistry C* **2017,** *121* (6), 3219-3227.
9. Broux, T.; Bamine, T.; Fauth, F.; Simonelli, L.; Olszewski, W.; Marini, C.; Ménétrier, M.; Carlier, D.; Masquelier, C.; Croguennec, L., Strong Impact of the Oxygen Content in Na3V2(PO4)2F3–yOy (0 ≤ y ≤ 0.5) on Its Structural and Electrochemical Properties. *Chemistry of Materials* **2016,** *28* (21), 7683-7692.
10. Grey, C. P.; Dupré, N., NMR Studies of Cathode Materials for Lithium-Ion Rechargeable Batteries. *Chemical Reviews* **2004,** *104* (10), 4493-4512.
11. Li, C.; Shen, M.; Lou, X.; Hu, B., Unraveling the Redox Couples of VIII/VIV Mixed-Valent Na3V2(PO4)2O1.6F1.4 Cathode by Parallel-Mode EPR and In Situ/Ex Situ NMR. *The Journal of Physical Chemistry C* **2018,** *122* (48), 27224-27232.
12. Nizamov, F. A.; Togulev, P. N.; Abdullin, D. R.; Khantimerov, S. M.; Balaya, P.; Suleimanov, N. M., Antisite defects and valence state of vanadium in Na3V2(PO4)3. *Physics of the Solid State* **2016,** *58* (3), 475-480.
13. Serras, P.; Palomares, V.; Goñi, A.; Gil de Muro, I.; Kubiak, P.; Lezama, L.; Rojo, T., High voltage cathode materials for Na-ion batteries of general formula Na3V2O2x(PO4)2F3−2x. *Journal of Materials Chemistry* **2012,** *22* (41).
14. Levitt, M. H., *Spin dynamics basics of nuclear magnetic resonance*. 2nd ed. ed.; John Wiley & Sons Ltd: Chichester, West Sussex, England ; Hoboken, N.J., 2008.

15. Bertini, I.; Luchinat, C.; Parigi, G.; Ravera, E., Chapter 1 - Introduction. In *NMR of Paramagnetic Molecules (Second Edition)*, Bertini, I.; Luchinat, C.; Parigi, G.; Ravera, E., Eds. Elsevier: Boston, 2017; pp 1-24.
16. Laws, D. D.; Bitter, H.-M. L.; Jerschow, A., Solid-State NMR Spectroscopic Methods in Chemistry. *Angewandte Chemie International Edition* **2002,** *41* (17), 3096-3129.
17. Bertini, I.; Luchinat, C.; Parigi, G.; Ravera, E., Chapter 5 - High resolution solid-state NMR in paramagnetic molecules. In *NMR of Paramagnetic Molecules (Second Edition)*, Bertini, I.; Luchinat, C.; Parigi, G.; Ravera, E., Eds. Elsevier: Boston, 2017; pp 127-150.
18. Langer, J.; Smiley, D. L.; Bain, A. D.; Goward, G. R.; Wilkening, M., An Unexpected Pathway: 6Li-Exchange NMR Spectroscopy Points to Vacancy-Driven Out-of-Plane Li-Ion Hopping in Crystalline Li2SnO3. *The Journal of Physical Chemistry C* **2016,** *120* (6), 3130-3138.
19. Smiley, D. L.; Davis, L. J. M.; Goward, G. R., An Improved Understanding of Li+ Hopping Pathways and Rates in Li3Fe2(PO4)3 Using Selective Inversion 6Li NMR Spectroscopy. *The Journal of Physical Chemistry C* **2013,** *117* (46), 24181-24188.
20. Smiley, D. L.; Goward, G. R., Ex Situ 23Na Solid-State NMR Reveals the Local Na-Ion Distribution in Carbon-Coated Na2FePO4F during Electrochemical Cycling. *Chemistry of Materials* **2016,** *28* (21), 7645-7656.
21. Billaud, J.; Clement, R. J.; Armstrong, A. R.; Canales-Vazquez, J.; Rozier, P.; Grey, C. P.; Bruce, P. G., beta-NaMnO2: a high-performance cathode for sodium-ion batteries. *Journal of the American Chemical Society* **2014,** *136* (49), 17243-8.
22. Ma, C.; Alvarado, J.; Xu, J.; Clement, R. J.; Kodur, M.; Tong, W.; Grey, C. P.; Meng, Y. S., Exploring Oxygen Activity in the High Energy P2-Type Na0.78Ni0.23Mn0.69O2 Cathode Material for Na-Ion Batteries. *Journal of the American Chemical Society* **2017,** *139* (13), 4835-4845.
23. Yan, G.; Mariyappan, S.; Rousse, G.; Jacquet, Q.; Deschamps, M.; David, R.; Mirvaux, B.; Freeland, J. W.; Tarascon, J. M., Higher energy and safer sodium ion batteries via an electrochemically made disordered Na3V2(PO4)2F3 material. *Nature communications* **2019,** *10* (1), 585.
24. Zeng, D.; Cabana, J.; Bréger, J.; Yoon, W.-S.; Grey, C. P., Cation Ordering in Li[NixMnxCo(1–2x)]O2-Layered Cathode Materials: A Nuclear Magnetic Resonance (NMR), Pair Distribution Function, X-ray Absorption Spectroscopy, and Electrochemical Study. *Chemistry of Materials* **2007,** *19* (25), 6277-6289.
25. Harris Robin, K.; Becker Edwin, D.; Cabral de Menezes Sonia, M.; Goodfellow, R.; Granger, P., NMR nomenclature. Nuclear spin properties and conventions for chemical shifts(IUPAC Recommendations 2001). In *Pure and Applied Chemistry*, 2001; Vol. 73, p 1795.
26. Kentgens, A. P. M., A practical guide to solid-state NMR of half-integer quadrupolar nuclei with some applications to disordered systems. *Geoderma* **1997,** *80* (3), 271-306.
27. Ashbrook, S. E.; Sneddon, S., New methods and applications in solid-state NMR spectroscopy of quadrupolar nuclei. *Journal of the American Chemical Society* **2014,** *136* (44), 15440-56.
28. Leskes, M.; Drewett, N. E.; Hardwick, L. J.; Bruce, P. G.; Goward, G. R.; Grey, C. P., Direct detection of discharge products in lithium-oxygen batteries by solid-state NMR spectroscopy. *Angew Chem Int Ed Engl* **2012,** *51* (34), 8560-3.
29. Bertini, I.; Luchinat, C.; Parigi, G.; Ravera, E., Chapter 2 - The hyperfine shift. In *NMR of Paramagnetic Molecules (Second Edition)*, Bertini, I.; Luchinat, C.; Parigi, G.; Ravera, E., Eds. Elsevier: Boston, 2017; pp 25-60.

30. Hung, I.; Zhou, L.; Pourpoint, F.; Grey, C. P.; Gan, Z., Isotropic high field NMR spectra of Li-ion battery materials with anisotropy >1 MHz. *Journal of the American Chemical Society* **2012,** *134* (4), 1898-901.
31. Perrin, C. L.; Dwyer, T. J., Application of two-dimensional NMR to kinetics of chemical exchange. *Chemical Reviews* **1990,** *90* (6), 935-967.
32. Kim, J.; Middlemiss, D. S.; Chernova, N. A.; Zhu, B. Y.; Masquelier, C.; Grey, C. P., Linking local environments and hyperfine shifts: a combined experimental and theoretical (31)P and (7)Li solid-state NMR study of paramagnetic Fe(III) phosphates. *Journal of the American Chemical Society* **2010,** *132* (47), 16825-40.
33. Middlemiss, D. S.; Ilott, A. J.; Clément, R. J.; Strobridge, F. C.; Grey, C. P., Density Functional Theory-Based Bond Pathway Decompositions of Hyperfine Shifts: Equipping Solid-State NMR to Characterize Atomic Environments in Paramagnetic Materials. *Chemistry of Materials* **2013,** *25* (9), 1723-1734.
34. Kresse, G.; Marsman, M.; Furthmuller, J., VASP the Guide. Computational Materials Physics, Faculty of Physics, Universitat Wien, Vienna, 2016.
35. Sholl, D.; Steckel, J. A., *Density functional theory: a practical introduction*. John Wiley & Sons: 2011.
36. Perdew, J. P.; Burke, K.; Ernzerhof, M., Generalized gradient approximation made simple. *Physical review letters* **1996,** *77* (18), 3865.
37. Blöchl, P. E., Projector augmented-wave method. *Physical review B* **1994,** *50* (24), 17953.
38. Kresse, G.; Joubert, D., From ultrasoft pseudopotentials to the projector augmented-wave method. *Physical Review B* **1999,** *59* (3), 1758.
39. Gourier, D.; Tranchant, A.; Baffier, N.; Messina, R., EPR study of electrochemical lithium intercalation in V2O5 cathodes. *Electrochimica acta* **1992,** *37* (15), 2755-2764.
40. Bersohn, M.; Baird, J. C., *Introduction to electron paramagnetic resonance*. 1966.
41. Weil, J. A.; Bolton, J. R., *Electron paramagnetic resonance: elementary theory and practical applications*. John Wiley & Sons: 2007.

Chapter 3: Investigating the relationship between structure and charge state in NMC622

3.1 Introduction

One of the most important family of cathodes in the battery industry are Ni-rich NMC materials. Considering that Ni is the redox-active ion in NMC materials within a typical voltage window, an excess of Ni ions increases the overall capacity. As introduced in Chapter 1, one such material is NMC622, $Li[Ni_{0.6}Mn_{0.2}Co_{0.2}]O_2$. NMC622 is a commercially available state-of-the-art material considered to be one of the best cathodes currently on the market for high power density applications, which is primarily due to its comparatively high experimental specific capacity of 190 mAh/g and theoretical capacity of 277 mAh/g.[1-3] Despite its success as a cathode material, however, how exactly NMC622 functions on the ionic level is not well understood.

The NMR spectrum and structure of pristine NMC622 are shown in Figure 3.1a and 3.1b respectively. NMC622 has a layered oxide structure with layers of mobile Li ions (green spheres) between TM sheets (blue polyhedra). TM sheets are known to consist of six-membered TM rings connected by oxygen bridges to central Li. A simplified view of the Li coordination environment can be seen in Figure 3.1c. A given Li ion within the Li layer is coordinated to six TMs in the TM sheets above and below it, corresponding to a total coordination number of twelve. Its total coordination environment is comprised of six TMs within its first coordination sphere (forming 90° interactions) and a second

coordination sphere (arising from 180° interactions).[4-5] While it is generally understood that the arrangement of TMs within the TM layer is highly disordered, there is some evidence to suggest that TM ion clustering can exist in these types of materials (SOC).[4, 6-10] Additionally, the mechanism for the $Ni^{2+} \rightarrow Ni^{4+}$ oxidation pathway is unclear.[2] There are two mechanisms by which Ni oxidation can reasonably occur. One is a stepwise mechanism where all Ni^{2+} is oxidized to Ni^{3+}, followed by all Ni^{3+} to Ni^{4+}. Alternatively, there could be a simultaneous mechanism where Ni^{2+} and Ni^{3+} are non-preferentially oxidized to Ni^{4+}. Studies have been done on NMC111[11] and NMC622[12] using X-ray Absorption Spectroscopy to elucidate the Ni-oxidation pathway, and interestingly, both studies found similar results. It was established that the Ni^{2+} ions at the surface of the electrode tend to be oxidized only to Ni^{3+}, whereas bulk Ni^{2+} will be oxidized to Ni^{4+} during cycling. While this surface-bulk differentiation is an important facet of these materials to realize, it cannot reveal whether there is a preference within the Ni-oxidation pathway for a stepwise or simultaneous mechanism of Ni^{2+} oxidation to Ni^{4+}. A deeper understanding of the Ni-oxidation pathway in NMC622, as representative of other Ni-rich materials, will be extremely valuable for the development and optimization of these types of materials in the future.

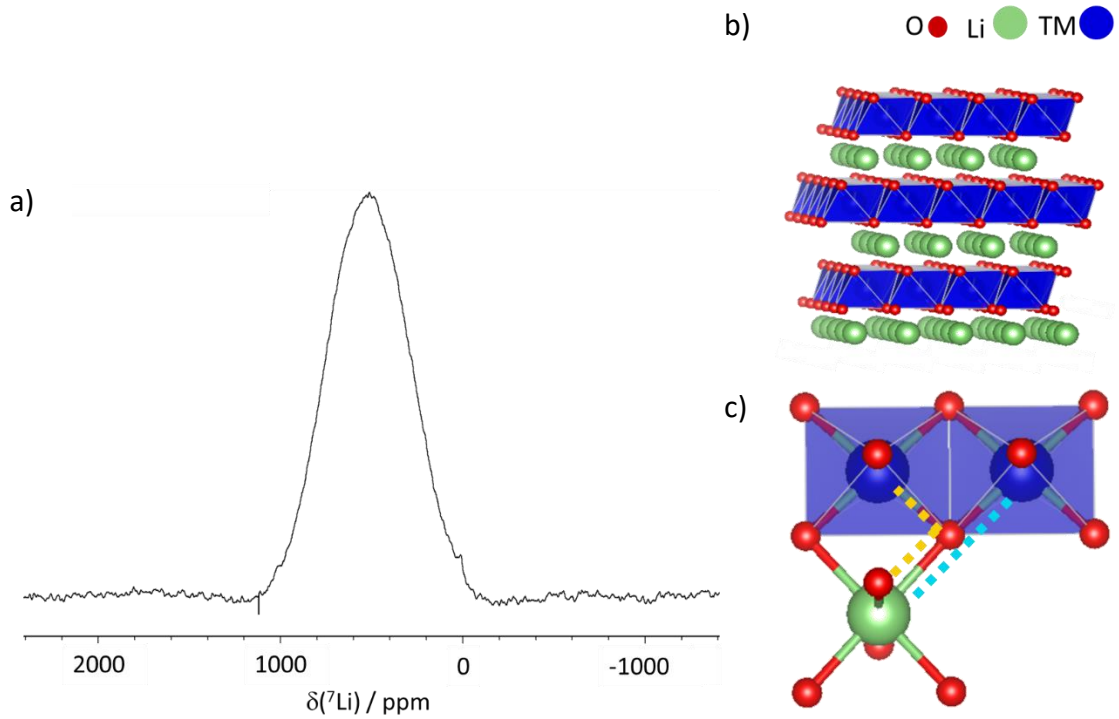

Figure 3.1 a) The ^{7}Li pj-MATPASS NMR spectrum of pristine NMC622. The spectrum corresponds to the middle slice of the pj-MATPASS spectrum. b) The NMC622 layered strucuture, where blue polyhedra denote TM layers and green spheres comprise the Li layer (oxygen atoms are not shown for clarity) c) An example of the Li coordination environment, where the yellow dashed line highlights the first cooridination sphere (90° interactions) and the turqoius dashed line outlines the second coordination sphere (180° interactions).

The basis of the analytical method developed herein was first demonstrated by Harris et. al.[4] to gain structural insight into disordered TM layers in a series of pristine NMC phases of the form $Li[Ni_xMn_xCo_{1-2x}]O_2$ phases (where x = 0.02, 0.1 and 0.33). In that study, ssNMR spectra were collected using the pj-MATPASS (projection magic angle turning phase-adjusted spinning sideband) experiment. This technique can be used to separate the isotropic and anisotropic shift contributions in paramagnetic materials. pj-

MATPASS is thus quite applicable to these NMC samples where paramagnetically broadened peaks, caused by paramagnetic TMs in the TM layer, can overlap with residual spinning side bands (SSBs) and make it difficult to only interpret isotropic spectral features. The pj-MATPASS experiment works by separating SSBs into different slices of a 2D spectrum, which can then be aligned and summed to yield the MAS spectrum. A single slice from the 2D spectrum, usually the centre slice, will contain only isotropic peaks.[4, 13]

In order to correlate ion arrangement within TMs in the TM layer to the pj-MATPASS NMR spectrum, Harris et. al.[4] developed a computational approach using Monte Carlo calculations. This computational approach simulates high temperature annealing by employing Monte Carlo simulations constrained by local charge neutrality and yields a simulated "structure" of the TM sheets, which in turn provides a statistical distribution of Li environments. A result is found when, at a certain simulated "temperature", the energy of the system remains constant with further iterations. The energy is defined as a charge balance of +2 for every O surrounded by three TMs and three Li, each contributing 1/6th of its charge to the total charge on O. The chemical shifts for ^{7}Li spectra can be calculated from these structures because various NMC phases have been analyzed so extensively over the years, that the contribution to Li's chemical shift by a given TM in the first and second coordination sphere is well known.[4-5] As previously described, Li between TM layers will be coordinated to TMs in the layers above and below it at either a 90° angle (1st coordination shell) or at 180° angles (2nd

coordination shell). The expected chemical shift, can therefore, be calculated for any Li in the TM layer as the sum of the surrounding TM contributions to the chemical shift, according to Table 3.1.

Table 3.1 The chemical shift contributions of TMs in NMC materials

TM ion	1st coordination shell (ppm)	2nd coordination shell (ppm)
Mn^{4+}	235	-53
Ni^{2+}	-30	120
Ni^{3+}	-18	72
Co^{3+}	0	0

By combining the results of experimental pj-MATPASS spectra and Monte Carlo simulated spectra, Harris was able to successfully produce a structural interpretation of observed experimental pristine NMC spectra.[4] An example pj-MATPASS spectrum showing the deconvolution and corresponding Monte Carlo simulated structure solution for pristine NMC111 is shown in Figure 3.2a and 3.2b, respectively.

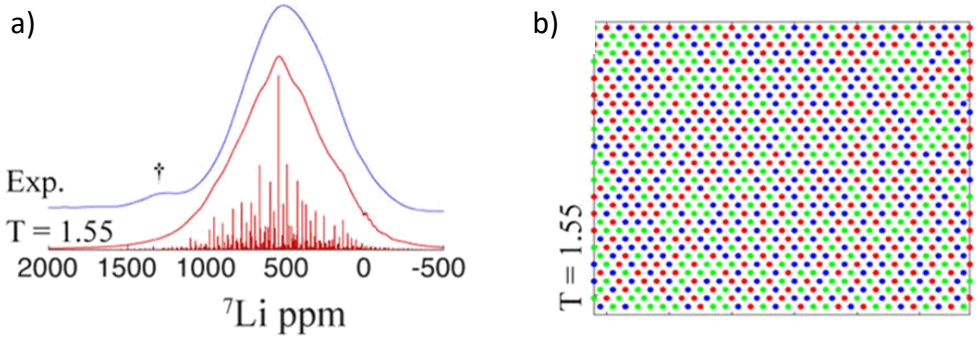

Figure 3.2 a) The comparison of the experimental NMR spectrum (blue) and the simulated spectrum with deconvoluted peaks (red) and b) the corresponding structure solution. The † symbol marks the peak corresponding to Li within the transition metal layer. Reprinted (adapted) with permission from Harris, K. J.; Foster, J. M.; Tessaro, M. Z.; Jiang, M.; Yang, X.; Wu, Y.; Protas, B.; Goward, G. R., Structure Solution of Metal-Oxide Li Battery Cathodes from Simulated Annealing and Lithium NMR Spectroscopy. Chemistry of Materials, *2017*, 29 *(13), 5550-5557. Copyright 2017 American Chemical Society.*

Building on this previous work by Harris, pj-MATPASS experiments and Monte Carlo simulations were performed on NMC622 in this project, where it is expected that Monte Carlo simulations will similarly yield corroborative structure solutions for Ni-rich NMC materials. In addition to analyzing pristine materials, the results presented herein also show the first applications of this technique to cycled NMC samples. The robustness of this technique to model changes in ion oxidation throughout cycling, was therefore, investigated throughout this work. As a result, some fascinating insights into NMC622 were found, which include the discovery of ion clustering leading to two distinct phases in this material. These methods and results will be explored in the work described below.

All of the experimental work of this project was done at McMaster University under the supervision of Prof. Gillian Goward and with the aid of Dr. Kristopher Harris. This experimental work primarily included electrochemical cycling and the collection of NMR spectra. The Monte Carlo calculations were done in collaboration with Dr. Jamie Foster at the University of Portsmouth, UK.

3.2 Methodology

3.2.1 Electrochemical measurements

NMC622 cathodes were prepared by grinding NMC622 (BASF), acetylene carbon black, and polyvinylidene fluoride (PVDF) in an 80:10:10 weight % ratio, respectively. PVDF was added to the NMC622/carbon black mixture through a solution of 2.005% PVDF in N-methyl-2-pyrrolidone (NMP), and the mixture was allowed to stir for 2 hours with a magnetic stir bar before being cast onto aluminum foil and smeared to a 381 μm thickness. The cathode cast was dried in the vacuum oven overnight at 120 °C. Individual cathode disks (0.5 inch diameter) were then punched out of the cast and assembled into coin cells in an argon-filled glovebox using 1.0 M $LiPF_6$ in EC/DEC (1:1 v% ratio ethylene carbonate : diethyl carbonate solution, from Aldrich) electrolyte against a Li metal anode. The cells were then cycled in an Arbin BT2000 instrument, at a C-rate of C/10. In order to analyze the cathodes after cycling, the batteries were disassembled in an argon-filled glovebox and the cathodes were washed thoroughly with DMC (dimethyl

carbonate) to minimize any $LiPF_6$ salt remaining on the cathode. During the washing process the cathodes were twice rinsed with DMC and then soaked in DMC for 30 min before being dried under vacuum for 30 min.

3.2.2 Solid-State ^{7}Li NMR

Lithium-7 ssNMR spectra were collected in a wide bore Bruker 200 MHz spectrometer (Corresponding to a ^{7}Li a resonance frequency of 77.72 MHz) at a typical MAS spinning speed of 60 kHz in a Bruker 1.3mm double resonance probe. Each experiment utilized a recycle delay of 100 ms. A typical $\pi/2$ pulse length was 1.5 μs. pj-MATPASS spectra were collected using the pulse program entitled, kh_pjMATPASSaltC, developed by Kristopher Harris. The QF acquisition mode (FnMODE) was implemented, and TD in the direct and indirect dimensions were 4096 and 16 respectively. An example of a pj-MATPASS experiment used in this work can be fund under the file directory, "CH_C3E_NMC62_Mar21_2018" in experiment three.

3.3 Results and Discussion

Due to the fact that disordered TM layers in the layered oxide NMC622 materials give rise to a large variety of possible ^{7}Li environments, resulting spectra show only a few, broad peaks which can span from 0 to 1000 ppm. Consequently, a combined experimental and simulation approach was applied to studying NMC622, which yielded

interesting results. Monte Carlo simulations were performed for pristine NMC622 material and additionally at various SOCs. Figure 3.1a shows an overlay of the experimental (purple, light blue, gold, dark blue) and calculated (black) NMC622 spectra for the pristine material and at various SOCs. The charge curve for NMC622 can be seen in Figure 3.1c, where the coloured circles represent the SOC for each of the corresponding NMR spectra in Figure 3.1a. The corresponding calculated structure solution for the pristine material is shown in Figure 3.1b. The peak at 0 ppm is believed to correspond with Li in SEI formed on the cathode, as the estimated T_1 for this peak was relatively long (on the order of seconds), likely corresponding to a polymerized compound arising from SEI formation. An extensive washing procedure was used to ensure the peak does not correspond to pure electrolyte. The peak at zero could also be attributed to Li surrounded in both its first and second coordination sphere by only Co^{3+}. Some general observations can be made about the broader more complicated regions of the spectra at higher chemical shifts as well. Peaks that appear at high chemical shifts will most likely correspond to Li surrounded by Mn in their first coordination sphere, because Mn has the largest contribution to the overall chemical shift. Similarly, Li surrounded primarily by Ni^{3+} will appear at lower chemical shifts due to the relatively small contribution of Ni^{3+} to the overall observed shift.

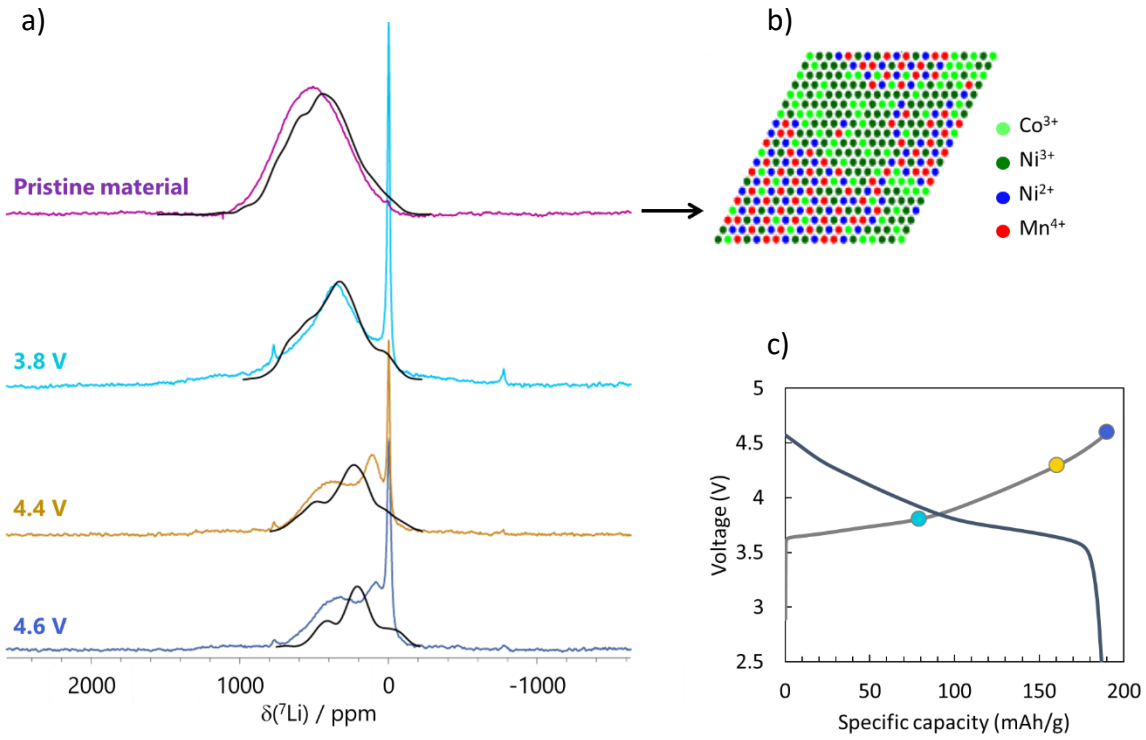

Figure 3.3 a) A comparison of experimental NMR spectra of NMC622 in the pristine state (purple), charged to 3.8 V (light blue), 4.4 V (gold), 4.6 V (dark blue) with the corresponding simulted spectrum overlayed (black). b) An example structure solution from Monte Carlo simulations of the pristine NMC622 material. c) The charge curve for NMC622 showing the three points at which the correcponding (by colour) NMR spectra were taken.

When examining the spectra in Figure 3.1a, it becomes apparent that there is a very good fit between the experimental and calculated spectra for the pristine and low SOC experimental spectra (3.8 V), whereas there is a poor correlation at high SOCs (4.4 and 4.6 V). Despite this poor agreement at high SOC, it is nonetheless possible to use the structure solution for pristine NMC622 in Figure 3.1b to gain insight into the initial ionic arrangement in this material. It is immediately apparent from the agreement between

the simulated and experimental spectra that ion clustering exists within the material in the pristine state. There appears to be regions of M^{3+} ion clustering, containing primarily Ni^{3+} and Co^{3+}, and regions of NMC111-like ion clusters containing Mn^{4+}, Ni^{2+}, and Ni/Co^{3+}. Li surrounded by Mn^{4+}, as in NMC111, must appear in the spectrum at higher chemical shifts because Mn^{4+} in the first coordination sphere has the largest positive contribution to the chemical shift.[4] Consequently, peaks appearing at high chemical shifts may be correlated with Li in NMC111 regions. This trend of ion clustering appears to be common in Ni-rich NMC materials, as evidenced by the Ni-rich material discussed in Chapter 1, which has an average composition of $Li[Ni_{0.68}Mn_{0.18}Co_{0.18}]O_2$.[14] As previously discussed, this material was synthesized by a novel co-precipitation method which resulted in the formation of bi-phasic particles containing a NMC811 core and outer layer composed of $Li[Ni_{0.46}Mn_{0.31}Co_{0.23}]O_2$. This bi-phasic behaviour was responsible for the high capacity and safe cycling behaviour of this material. It is interesting that a similar, albeit less distinct, bi-phasic ionic arrangement exists in NMC622 as well. In this case, the two co-existing phases are Ni^{3+}/Co^{3+} and NMC111 regions, which follows a similar trend in having a Mn-rich phase surrounding some sort of Ni-dominated phase. It may be possible to surmise from these preliminary results that the optimal low energy charge balance in Ni-rich materials is only accomplished by naturally occurring charge segregation. This information can be used to more strategically develop Ni-rich NMC materials in the future to perhaps synthetically induce

charge segregation to safely harness an even greater proportion of Ni oxidation potential.

From the above results, it is apparent that Monte Carlo simulations can be extremely informative about complicated NMR spectra of NMC materials. However, the poor fit at high charge states currently limits the extent of useful information that can be gleaned from the simulations. It is likely that the reason for this poor fit is that the current Monte Carlo calculations do not accurately account for the delithiation process that occurs during charging. The calculations are currently setup to force delithiation from the NMC111 regions as opposed to the M^{3+} regions, which can be observed in the simulated spectra as an intensity decrease primarily for peaks at higher chemical shifts throughout charging, corresponding to regions containing considerable amounts of Mn^{4+} in the first coordination sphere. However, the experimental spectra do not show this same trend, but instead show that intensity generally decreases more at lower chemical shifts during charging.

In order to achieve a better fit between the calculated and experimental results, the Monte Carlo simulations must be altered to better account for delithiation of the cathode during charging. Some suggested alterations to the calculations will be discussed more thoroughly in Section 3.4. The current calculations do reveal, however, that delithiation during charging in this material does not occur primarily from the NMC111 regions in the material. Therefore, some other delithiation model must be responsible for the observed experimental trend. Two possible alternative models could

be that Li is first extracted from the M^{3+} region followed by extraction from the NMC111 region. Otherwise, the accurate model would be that delithiation occurs non-preferentially from both NMC111 and M^{3+} regions at the same time. However, Monte Carlo simulated spectra will be able to shed more light on the exact ionic arrangement at each SOC which will be invaluable in determining the method of delithiation.

3.4 Summary and outlook

The results presented in this chapter demonstrate the efficacy of using both NMR and statistical Monte Carlo calculations to extract valuable information from low-resolution NMR spectra of disordered, paramagnetic cathode materials. In this project, a combination of these two techniques was used to analyze a commercialized Ni-rich material, NMC622. Monte Carlo simulations were carried out to elucidate the relationship between the observed NMR spectra and the ionic arrangement within TM layers. The calculated spectra show very good correlation in the pristine and low SOC states. Therefore, analyzing the structure solution for calculations of the pristine state reveal that ion clustering occurs in these materials, where ions will tend to cluster either into NMC111-like or Ni/Co^{3+} regions. This result suggests that charge balance in this material is best achieved by ionic clustering, which seems consistent with similar Ni-rich materials.

However, the simulated spectra do not fit the experimental spectra at higher charge states. It may, therefore, be possible to improve the calculated fit at higher SOCs

by altering the calculations in one of two ways: first, by allowing delithiation from M^{3+} in addition to NMC111 regions, or, second, forcing delithiation from M^{3+} before allowing it to occur in NMC111 regions. Whichever resulting simulated spectrum best fits the experimental data will be very informative about the preferred delithiation method in these Ni-rich NMC materials, if indeed there is any preference for Li deintercalation in these regions. Altering the calculations in this way would also give insight into the Ni-oxidation pathway in these materials, where a good simulation fit from calculations that allowed non-preferential delithiation from both NMC111 (containing Ni^{2+} and Ni^{3+}) and M^{3+} regions would indicate that the simultaneous mechanism of Ni-oxidation is preferred. Whereas, a good fit between experimental and simulated spectra for calculations where delithiation was forced to occur initially from M^{3+} regions, would indicate that some sort of stepwise mechanism is instead preferred.

This work, therefore, has demonstrated the viability of Monte Carlo calculations, informed by ssNMR experiments, to give valuable information about disordered cathode materials. The future of this work is dependent on how the calculations will be modified to fit experimental results. The resulting information regarding ionic clustering behaviour, delithiation methods, and the preferred Ni-oxidation pathway will be extremely useful in informing the strategic development of Ni-rich LIB cathode materials for application in high power density applications.

3.5 References

1. Jung, R.; Metzger, M.; Maglia, F.; Stinner, C.; Gasteiger, H. A., Chemical versus Electrochemical Electrolyte Oxidation on NMC111, NMC622, NMC811, LNMO, and Conductive Carbon. *J Phys Chem Lett* **2017,** *8* (19), 4820-4825.
2. Wang, Q.; Shen, C. H.; Shen, S. Y.; Xu, Y. F.; Shi, C. G.; Huang, L.; Li, J. T.; Sun, S. G., Origin of Structural Evolution in Capacity Degradation for Overcharged NMC622 via Operando Coupled Investigation. *ACS Appl Mater Interfaces* **2017,** *9* (29), 24731-24742.
3. Schmuch, R.; Wagner, R.; Hörpel, G.; Placke, T.; Winter, M., Performance and cost of materials for lithium-based rechargeable automotive batteries. *Nature Energy* **2018,** *3* (4), 267-278.
4. Harris, K. J.; Foster, J. M.; Tessaro, M. Z.; Jiang, M.; Yang, X.; Wu, Y.; Protas, B.; Goward, G. R., Structure Solution of Metal-Oxide Li Battery Cathodes from Simulated Annealing and Lithium NMR Spectroscopy. *Chemistry of Materials* **2017,** *29* (13), 5550-5557.
5. Liu, H.; Bugnet, M.; Tessaro, M. Z.; Harris, K. J.; Dunham, M. J.; Jiang, M.; Goward, G. R.; Botton, G. A., Spatially resolved surface valence gradient and structural transformation of lithium transition metal oxides in lithium-ion batteries. *Physical Chemistry Chemical Physics* **2016,** *18* (42), 29064-29075.
6. Zeng, D.; Cabana, J.; Bréger, J.; Yoon, W.-S.; Grey, C. P., Cation Ordering in Li[NixMnxCo(1–2x)]O2-Layered Cathode Materials: A Nuclear Magnetic Resonance (NMR), Pair Distribution Function, X-ray Absorption Spectroscopy, and Electrochemical Study. *Chemistry of Materials* **2007,** *19* (25), 6277-6289.
7. Yan, P.; Xiao, L.; Zheng, J.; Zhou, Y.; He, Y.; Zu, X.; Mao, S. X.; Xiao, J.; Gao, F.; Zhang, J.-G.; Wang, C.-M., Probing the Degradation Mechanism of Li2MnO3 Cathode for Li-Ion Batteries. *Chemistry of Materials* **2015,** *27* (3), 975-982.
8. Jarvis, K. A.; Deng, Z.; Allard, L. F.; Manthiram, A.; Ferreira, P. J., Atomic Structure of a Lithium-Rich Layered Oxide Material for Lithium-Ion Batteries: Evidence of a Solid Solution. *Chemistry of Materials* **2011,** *23* (16), 3614-3621.
9. Seo, D.-H.; Lee, J.; Urban, A.; Malik, R.; Kang, S.; Ceder, G., The structural and chemical origin of the oxygen redox activity in layered and cation-disordered Li-excess cathode materials. *Nature Chemistry* **2016,** *8*, 692.
10. Shukla, A. K.; Ramasse, Q. M.; Ophus, C.; Duncan, H.; Hage, F.; Chen, G., Unravelling structural ambiguities in lithium- and manganese-rich transition metal oxides. *Nature communications* **2015,** *6*, 8711.
11. Yoon, W.-S.; Balasubramanian, M.; Chung, K. Y.; Yang, X.-Q.; McBreen, J.; Grey, C. P.; Fischer, D. A., Investigation of the charge compensation mechanism on the electrochemically Li-Ion deintercalated Li1-x Co1/3Ni1/3Mn1/3O2 electrode system by combination of soft and hard X-ray absorption spectroscopy. *Journal of the American Chemical Society* **2005,** *127* (49), 17479-17487.
12. Tian, C.; Nordlund, D.; Xin, H. L.; Xu, Y.; Liu, Y.; Sokaras, D.; Lin, F.; Doeff, M. M., Depth-Dependent Redox Behavior of LiNi0.6Mn0.2Co0.2O2. *Journal of The Electrochemical Society* **2018,** *165* (3), A696-A704.
13. Hung, I.; Zhou, L.; Pourpoint, F.; Grey, C. P.; Gan, Z., Isotropic high field NMR spectra of Li-ion battery materials with anisotropy >1 MHz. *Journal of the American Chemical Society* **2012,** *134* (4), 1898-901.

14. Sun, Y.-K.; Myung, S.-T.; Park, B.-C.; Prakash, J.; Belharouak, I.; Amine, K., High-energy cathode material for long-life and safe lithium batteries. *Nature Materials* **2009,** *8*, 320.

Chapter 4: A Magnetic Resonance Study of a Promising Family of Sodium Ion Battery Cathode Materials, $Na_3V_{2-x}Ga_x(PO_4)_2F_3$

4.1 Introduction

Although LIBs are currently the most widely commercialized battery technology, concerns about the global Li supply have led to the development of LIB alternatives. It is generally believed that if LIB technology was widely adopted in both EV and grid energy storage applications, the global Li supply would eventually be depleted so extensively that the cost of Li would skyrocket.[1-2] SIBs have thus been developed as an alternative to LIB technology. Na is significantly cheaper than Li because it is far more naturally abundant.[1-5] The redox potential of Na (-2.71 V versus the standard hydrogen electrode) is also only 0.3 V higher than that of Li. Consequently, Na is a viable alternative to Li for battery applications both in terms of its cost and electrochemical potential.

One of the most promising SIB cathodes currently on the market is NVPF ($Na_3V_2(PO_4)_2F_3$) because it has a high theoretical specific capacity of 128 mAh/g. NVPF is particularly competitive for high energy density applications because its theoretical energy density (507 Wh/kg) is comparable to certain commercialized LIB cathodes.[5-6]

The structure of NVPF crystallizes into the Amam space group composed of redox-active V^{3+} ions at the centre of corner-sharing $V_2O_8F_3$ bioctahedra. F ions lie along the axis of the bioctahedra, which are connected by PO_4 tetrahedra. This ion arrangement forms a NASICON-type framework which is ideal for fast Na ion mobility. The structure

of NVPF can be seen in Figure 4.1a Large tunnels exist in the structure along the [110] and [1$\bar{1}$0] directions, shown in Figure 4.1b, which not only allow Na mobility but also help maintain structural stability during cycling.[6-7] The structure contains 3 unique Na sites, however, only two Na ions have been observed to participate in electrochemical cycling. Charge balance is maintained during Na extraction by the V^{3+}/V^{4+} redox couple, which have $3d^2/3d^1$ electronic configurations respectively. [6-8] The observed electrochemical behaviour of NVPF corresponds to the one-electron capacity limitation of the V^{3+}/V^{4+} redox couple.[9]

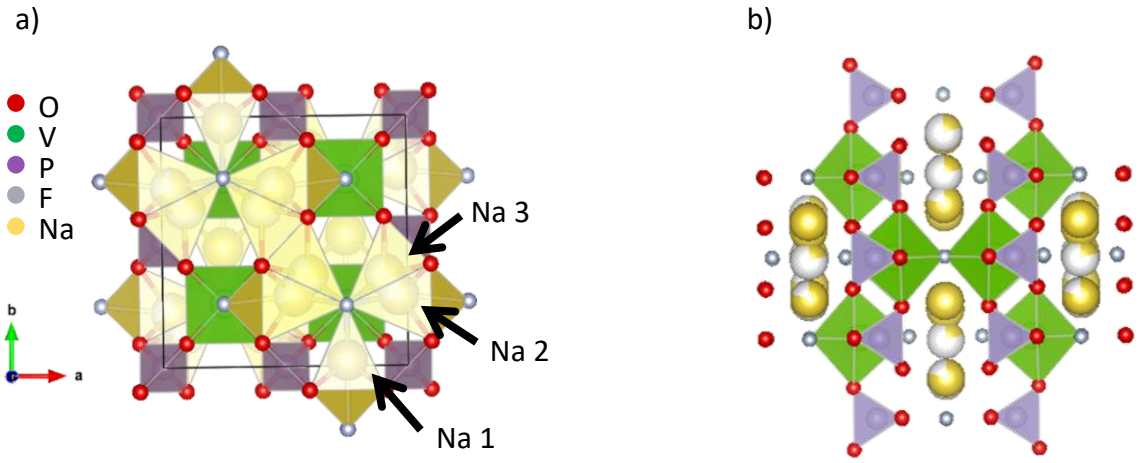

Figure 4.1 a) The crystal structure of the NVPF viewed along the c axis of the unit cell. The three Na sites are labeled in the structure. b) A view of the NVPF crystal structure along the [110] direction highlighting the tunnels for Na ion mobility.

During the synthesis of NVPF, O can inadvertently substitute for F in the corners of the bioctahedra, according to the general formula $V_2O_8F_{3-y}O_y$.[8, 10] This substitution causes the V oxidation state to shift from 3+ to 4+. Interestingly, this O-substitution actually has the effect of lowering the average operating voltage of the material and

increasing the capacity. It is believed this effect occurs because the oxygen doping allows higher electronic conductivity and lowers the Na ion mobility activation energy. Ab initio calculations also revealed that a larger range of V oxidation states, potentially V^{2+} to V^{5+}, could be achieved in this material while still maintaining structural stability. However, the calculations revealed that the full V oxidation range is not experimentally observed due to large Na diffusion energy barriers and highly stable Na ordering.

In order to experimentally confirm that the capacity of NVPF was not fundamentally limited by the available range of V oxidations states, Matts, et. al.[9] synthesized a sample doped with electrochemically inactive Ga. Ga^{3+} is a reasonable substitution for V^{3+} in the structure because it has a similar ionic radius to V (0.62 Å as opposed to 0.64 Å for V).[11] Consequently, a direct substitution of Ga for V does not significantly alter the unit cell. Batteries made of this Ga-doped material, $Na_3VGa(PO_4)_2F_3$, demonstrated additional voltage plateaus in the charge/discharge curve and a larger specific capacity than the NVPF parent material. By modeling this cycling behaviour with first-principles calculations, it was determined that Ga-doping pushes V to a larger oxidation range than observed in NVPF. The additional plateaus in the charge curve were attributed to V being oxidized to V^{2+}, V^{3+}, V^{4+}, and V^{5+} during cycling. The increased capacity as compared to NVPF was attributed to accessing this greater range of V oxidation states.

Ga-substituted NVPF variants are not only valuable to study for the information they can potentially yield about vanadium fluorophosphate cathodes in general, but also

for their application in ssNMR spectroscopy. ssNMR was the primary method employed to analyze the structure and dynamics of these materials throughout this work, because it is very sensitive to different ions and their environments. This sensitivity makes it possible to obtain information about how ions are arranged within the structure and about ion mobility, where fast ion motion is associated with high power batteries. However, as discussed in detail in Chapter 2 of this thesis, paramagnetic ions can have very dramatic effects on the observed NMR signal. Often the effects are undesirable, where peak broadening and shortened T_1 times can make it difficult to extract meaningful information from NMR spectra of paramagnetic samples. NVPF is one such paramagnetic material due to the V^{3+} ion containing two unpaired electrons in its t_{2g} orbital.[8] By substituting some of the V^{3+} out for diamagnetic Ga^{3+}, some undesirable paramagnetic effects are diminished and it becomes possible to extract more information from the corresponding NMR spectra.

Electron paramagnetic resonance (EPR) was also used to analyze these cathode samples. While EPR is generally a very effective technique for investigating paramagnetic materials, it has certain pertinent limitations. As previously mentioned, the paramagnetic V^{3+} ion present in pristine $Na_3V_2(PO_4)_2F_3$ is in an octahedral environment and a $3d^2$ electron configuration. There are seven crystal-field energy levels in a $3d^2$ ion in an octahedral environment, which split into two triply degenerate states and one non-degenerate state, as can be seen in Figure 4.2.[12-15] The lowest energy level triplet will then be further split into a low energy singlet and a higher energy doublet

due to octahedral distortions caused by spin-orbit interactions. The transition energy between the low-level singlet and doublet is so small that the spin-lattice relaxation rate is too fast for the signal to be observed at room temperature. At very low temperatures, less than 5 K, the spin-lattice relaxation rate is sufficiently lengthened to observe signals from octahedral V^{3+} ions. EPR in this work was limited to higher temperatures, however, the technique was still applied to the study of synthesized cathode materials, and generally supplied many valuable insights.

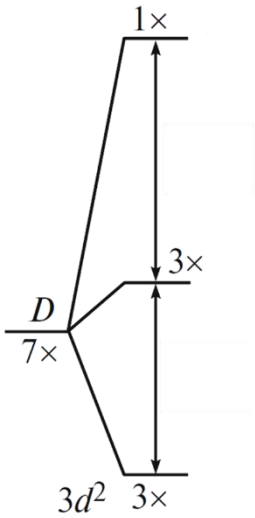

Figure 4.2 A schematic of the ground state splitting which occurs in $3d^2$ octahedral environment. Reprinted (adapted) with permission from Nizamov, F. A.; Togulev, P. N.; Abdullin, D. R.; Khantimerov, S. M.; Balaya, P.; Suleimanov, N. M., Antisite defects and valence state of vanadium in Na3V2(PO4)3. Physics of the Solid State, *2016,* 58 *(3), 475-480. Copyright 2016 Springer Nature.*

The work outlined in this chapter is part of an ongoing project to correlate structural properties to ion dynamics in the Ga-substituted family of cathodes, Na_3V_{2-}

$_xGa_x(PO_4)_2F_3$. Three members of this family were synthesized, where x = 0, 1, and 2. The pure paramagnetic nature of NVPF (x = 0) made investigation by ssNMR challenging. Consequently, EPR was also employed. The mixed phase material, NVGPF (x = 1), was primarily investigated using a combination of DFT calculations, ssNMR, and EPR to elucidate the relationship between structure and Na-ion dynamics in both the pristine and cycled materials. It was found that the mixed phase material is a highly dynamic material, where Na ion mobility is very favorable. A similar approach was taken with the pure Ga material, NGPF (x= 2), using ssNMR and X-ray diffraction. Although Ga is electrochemically inactive, NGPF was synthesized to potentially provide structural insight in a similar system where all paramagnetic effects have been removed. The results of this work have thus far demonstrated the effectiveness of using various magnetic resonance techniques, both ssNMR and EPR, in conjunction with ab initio calculations to investigate paramagnetic cathode materials and proves the viability of the NVPF family of cathodes for application in SIBs.

The synthesis of materials, NMR and EPR experiments, and electrochemical measurements presented in this chapter were performed at McMaster University under the supervision of Dr. Gillian Goward. Rietveld refinement of NGPF was completed with aid of Dr. Yurij Mozharivskyj at McMaster University. DFT calculations were performed by the author, under the guidance of Dr. Dany Carlier at the Institut de Chimie de la Matière Condensée de Bordeaux which is affiliated with the Université de Bordeaux. The VASP software was hosted by the Université de Bordeaux.

4.2 Methodology

4.2.1 Solid-state NMR experiments

Sodium-23 ssNMR spectra were collected in a Bruker 500 MHz spectrometer (corresponding to a ^{23}Na resonance frequency of 132 MHz) in a Bruker double resonance 2.5 mm rotor at 30 kHz MAS and referenced to solid NaCl (δ = 0).[16] EXSY experiments were implemented using the typical pulse sequence, 90-t_1-90-t_{mix}-90. The ^{31}P ssNMR spectra were collected in a Bruker 200 MHz spectrometer (^{31}P resonance frequency of 81.0 MHz) in a Bruker 1.3mm double resonance probe at a spinning speed of 60 kHz and referenced to 85.0% H_3PO_4 (Caledon). The ^{31}P spectra was collected using a typical Hahn-echo pulse sequence with a recycle delay of 1 s. A typical $\pi/2$ pulse for ^{23}Na and ^{31}P was 1 μs and 2.8 μs, respectively.

4.2.2 EPR experiments

EPR spectra were collected on a Bruker EMXnano EPR spectrometer running Xenon software. The parameters of the experiments were as follows: microwave frequency of 9.6 GHz, microwave power of 25 dB (for NVPF) and 10 db (for NVGPF), modulation frequency 100kHz, and modulation amplitude 4 G. All experiments were done at room temperature.

4.2.3 Electrochemical cycling

NVGPF cathodes were prepared by combining synthesized NVGPF, Super P carbon black, and polyvinylidene fluoride (PVDF) in a 75:15:10 weight % ratio, respectively. PVDF was added to the NVGPF/carbon black mixture as a solution of 2.005% PVDF in NMP. The mixture was stirred for 3 hours with a magnetic stir bar before being cast onto aluminum foil and smeared to a 254 μm thickness. The cathode cast was dried in a vacuum oven overnight at 120 °C. 0.5 inch cathode disks were then punched out of the cast and assembled into coin cells in an argon-filled glovebox using 0.6 M $NaPF_6$ in 3:7 EC/DMC (3:7 v% ratio ethylene carbonate (Sigma Aldrich) : dimethyl carbonate solution (Sigma Aldrich)) electrolyte against a Na metal anode. The cells were then cycled in an Arbin BT2000 Instrument at a C-rate of C/20 (according to an expected capacity of 141 mAh/g) between a voltage range of 1.2 – 4.5 V.[9] After cycling the batteries were disassembled in an argon-filled glovebox and the cathodes were washed with DMC to rinse remaining electrolyte or electrolyte salt from the cathode. This washing process involved first rinsing the cathodes with DMC and then soaking them in DMC for 30 min. This rinsing process was repeated twice before the cathodes were dried under vacuum for 30 min.

4.2.4 Synthesis and characterization of NVPF, the V-Ga mixed phase, and NGPF

Powder X-ray diffraction patterns for all samples were collected on a PANalytical diffractometer using Cu Kα radiation at room temperature using a 2θ range from 15° to 60°. NVPF and the NVGPF were synthesized as a two-step reaction according to the literature.[9, 17] The intermediate product from the first step of the reaction was VPO_4 or $V_{0.5}Ga_{0.5}PO_4$, respectively. NVPF was made by mixing stoichiometric amounts of V_2O_5 and $NH_4H_2PO_4$ with 15% Super P carbon black by mass and dry ball milling the mixture for 24 hours. Ball milling was done in a Teflon ball milling container with three Teflon pellets used for grinding, which were approximately 1 cm in diameter each, to grind a typical sample size of 1 g. It was then pelletized and heated in a tube furnace under a constant flow of Ar for 4 hours at 750 °C. The resulting VPO_4 was then ground. Stoichiometric amounts of VPO_4 and NaF were ball milled together for 2 hours, pelletized, and calcined under constant Ar flow for 1.5 hours at 750 °C to yield the final NVPF product.

The synthesis of the mixed phase material, NVGPF, was similarly done using stoichiometric amounts of both V_2O_5 and Ga_2O_3 with $NH_4H_2PO_4$ and 15% Super P carbon black by mass. The mixture was dry ball milled for 24 hours and heated for 8 hours at 850 °C under Ar. The resulting $V_{0.5}Ga_{0.5}PO_4$ was crushed, mixed with stoichiometric amounts of NaF, ball milled for 2 hours, and calcined for 2 hours at 750 °C under Ar flow. It should be noted as well that the amount of time allowed in the first ball milling step

for the mixed phase material had a large impact on the final arrangement of V and Ga in the structure. Figure 4.3 shows the X-ray powder patterns and corresponding ssNMR spectra of two mixed phase materials that underwent ball milling for a) 48 hours and b) 24 hours. It is apparent that V and Ga are more intimately mixed together in the sample that was ball milled for 48 hours as opposed to the sample that was ball milled for 24 hours. This is evident by the broader peak corresponding to more homogeneous Na environments in the NMR spectrum of the sample ball milled for 48 hours in contrast to the more separated regions of peaks in the sample ball milled for 24 hours, which would indicate more distinct Na environments. A sample ball milled for 96 hours was also synthesized, and the resulting X-ray pattern and ssNMR spectra (shown in Appendix, Section A.1) were not significantly different to those of the material mixed for 48 hours, indicating that V and Ga are as homogenously mixed as they can be using this method in the sample ball milled for 48 hours. Consequently, for the remainder of this thesis the sample ball milled for 48 hours will be referred to as homogenous-NVGPF (h-NVGPF). The majority of the work presented in this thesis was performed on the material mixed for 24 hours (NVGPF) as it was synthesized before the h-NVGPF synthesis was optimized and was synthesized according to the procedure outlined in the literature so it can be more easily compared to the literature results.

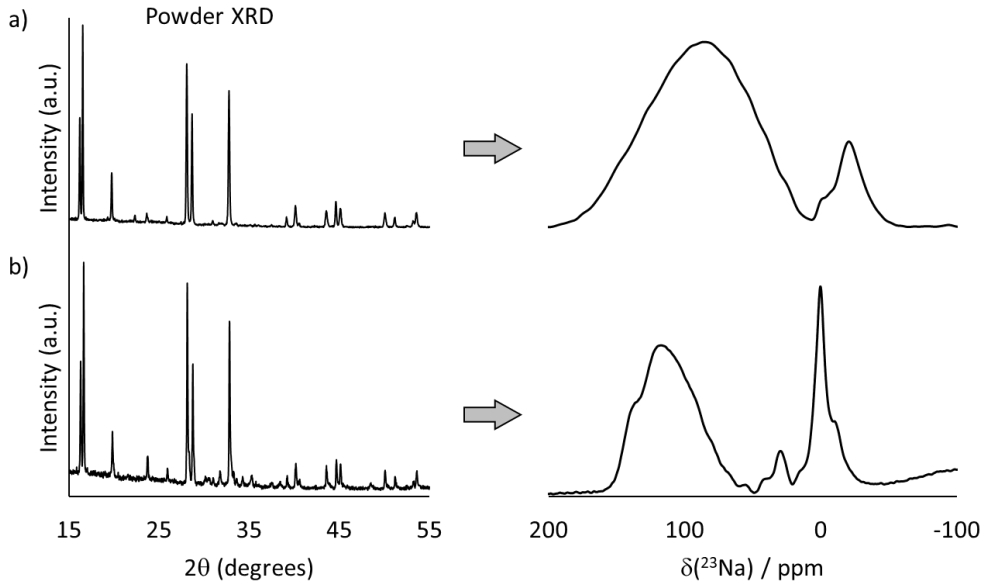

Figure 4.3 The X-ray powder patterns and corresponding ssNMR spectra of mixed phase materials ball milled at a) 48 hours (h-NVGPF) and b) 24 hours (NVGPF)

Synthesis of the fully Ga-substituted material (NGPF) was also done by mixing stoichiometric amounts of Ga_2O_3 and $NH_4H_2PO_4$ with 15% Super P carbon black by mass and dry ball milling the mixture for 24 hours. The resulting powder was then pelletized and heated for 24 hours at 1000 °C under Ar flow. The intermediate product was then crushed and mixed with 10% by mass excess amount of NaF before ball milling for 24 hours and heating for 8 hours at 750 °C. Because there has never been a pure sample of NGPF synthesized in the literature to date, these synthesis conditions had to be optimized over several attempts to obtain a crystalized product. Excess NaF was added because it was revealed through Rietveld refinement of a previously synthesized sample that the material was Na deficient. Following the synthesis, the sample was washed with

water to remove any unreacted NaF, although no NaF was observed in the preliminary powder XRD patterns of this sample. The refined powder X-ray diffraction pattern for NGPF is shown in Figure 4.4, which shows a good fit with the expected Amam structure based on the NVPF parent material. The unit cell parameters for the refined NGPF structure and the parent NVPF material can be seen in Table 4.1. The unit cell volume for NGPF is 4% smaller than NVPF, which is logical considering that the ionic radius of Ga^{3+} is less than V^{3+}. It should also be noted that there appears to be some amorphous background in the XRD pattern of NGPF, which indicates that the optimized synthesis of NGPF used in this work may need to be yet further optimized in order to push the synthesis to completion.

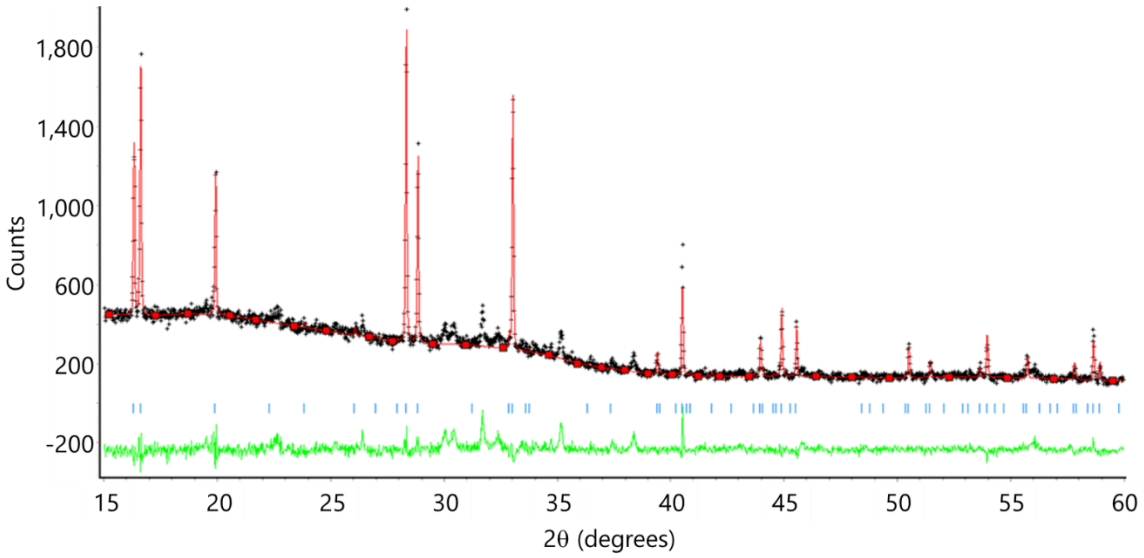

Figure 4.4. Rietveld refinement for NGPF showing the experimental pattern in black, the calculated in red, and the difference in green

Table 4.1 The unit cell parameters of synthesized NGPF refined in this work and NVPF (obtained from the combined Rietveld refinement of synchrotron radiation and neutron diffraction obtained by Bianchini et. al.[18])

	a (Å)	b (Å)	c (Å)	Volume (Å^3)
Experimental NVPF [18]	9.02847(3)	9.04444(3)	10.74666(6)	877.54
Refined NGPF	8.89583(7)	8.89095(8)	10.64178(7)	841.6(8)

4.2.5 DFT calculations

All ab-initio calculations performed in this work utilized Density Functional Theory (DFT) using the Vienna Ab-initio Simulation Package (VASP). The Generalized Gradient Approximation (GGA) method with Projector Augmented Wave (PAW) pseudopotentials were employed. The PAW-PBE potentials were implemented from those included in the VASP software. A k-point grid of 2x2x2 was chosen for all calculations in order to minimize the length of time for each calculation, which was possible because the unit cell parameters were not significantly different from each other. An energy cutoff of 600 eV was chosen for the plane wave basis set. The calculations were carried out in two steps. First, an optimized structure was found. Second, the unpaired electron density for all atoms in the unit cell was then calculated from the optimized structure. In order to more accurately account for the sample temperature in chemical shift calculations, a temperature of 320 K was used

corresponding to the expected heating of a rotor spinning at 60 kHz. It should also be noted that two of the three Na sites in the NVPF crystal structure (Na1 and Na2) have overlapping atomic positions, which inhibits the VASP software from finding an optimized structure. Consequently, only the Na2 site was included in the starting structure inputted into the VASP software and the Na1 site was deleted, which allowed the software to successfully find an optimized structure in all cases.

In order to obtain reasonable calculated S(tot) values, which correspond to the total number of unpaired electrons in the unit cell, S(tot) had to be fixed to the expected value in the input for all Ga-substitution calculations. The value of S(tot) can be known prior to calculations, as there are 8 V^{3+} ions in the unit cell each containing 2 unpaired electrons. Thus, with every Ga substitution into the unit cell, the total amount of unpaired electrons decreases by 2. Without fixing S(tot) the results of the calculations would produce S(tot) values that were illogical considering the amount of Ga being substituted into the unit cell. Having total number of unpaired electrons that was different than one would expect in a paramagnetic system indicated the presence of antiferromagnetic (AF) coupling. The corresponding calculated ^{23}Na chemical shifts were slightly negative due to AF coupling. However, it was very difficult to distinguish if these calculated peaks were present in the broad peaks of the experimental spectrum. Therefore, in order to determine if there was indeed AF coupling in the material, the phosphorus-31 chemical shifts were also calculated and compared to an experimental NMR spectrum. The ^{31}P nucleus was preferable to ^{23}Na for analysis in this case because

the ^{31}P chemical shift range is much larger (typically between 0 and 7000 ppm) than ^{23}Na (between 0 and 200 ppm) for these kinds of materials, making it potentially much easier to distinguish negative peaks in the experimental spectrum.[8] According to the calculated ^{31}P chemical shifts in AF systems, peaks should appear in the spectrum across a large range of negative chemical shifts. The presence of AF coupling was, therefore, discounted in this material because no peaks appeared in the negative chemical shift range expected, as shown in the experimental spectrum in Figure 4.5.

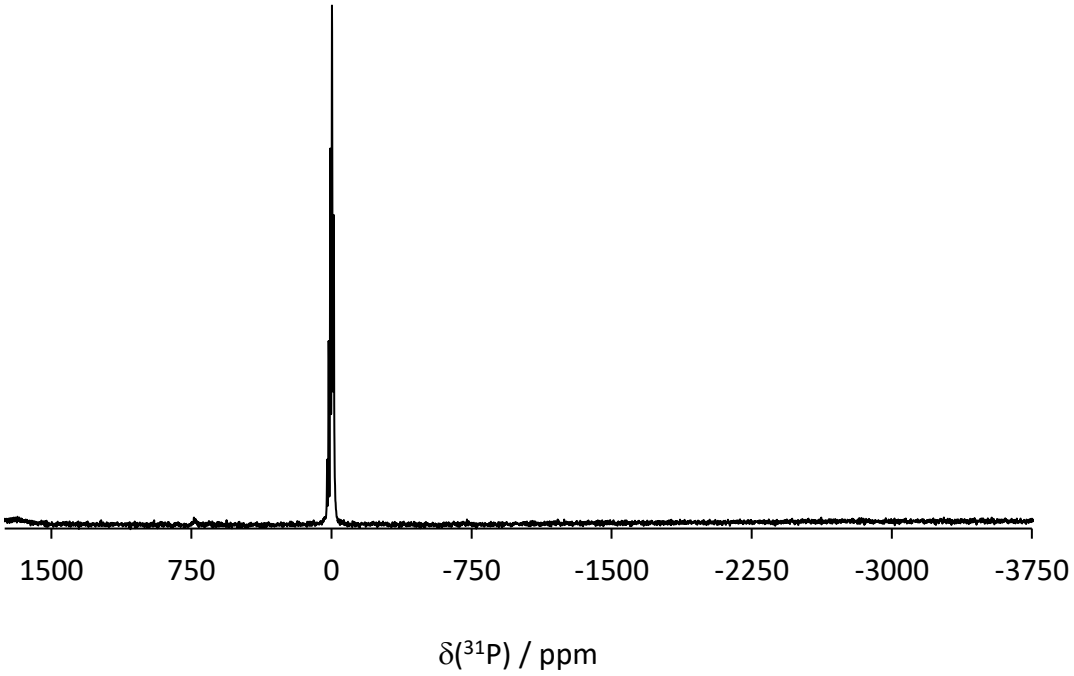

Figure 4.5 The ^{31}P NMR spectrum of h-NVGPF

4.3 Results and Discussion

4.3.1 NVPF

Due to complications arising from paramagnetism in the parent material, NVPF, it was difficult to analyze using only ssNMR. Figure 4.6 shows the ssNMR spectrum of NVPF. The large peak at 140 ppm contains the three expected Na sites paramagnetically broadened into one peak. The small peak at 90 ppm corresponds to a small amount of Na surrounded by V^{4+} due to oxygen-substitution, as previously discussed.[8] These chemical shifts were assigned according to an extensive study by Broux et. al.[8] which measured a series of NMR spectra of NVPF with various amounts of O-substitution. In comparison to their work, it can be concluded that the sample of NVPF shown here contains the least amount of O-substitution as an unintentional result of synthetic

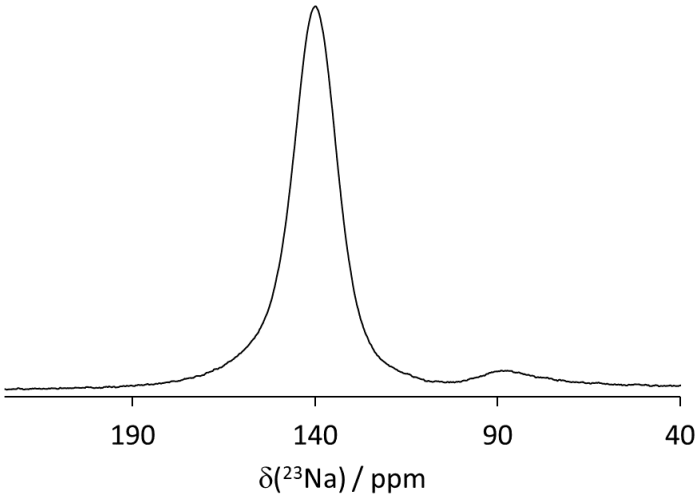

Figure 4.6 The ^{23}Na ssNMR spectrum of NVPF

conditions. Because the three Na sites of NVPF have all broadened into one peak and the T_1 of this sample is so short (approximately 0.5 ms), it was difficult to implement any quantitative NMR methods on this sample, such as selective inversion or EXSY experiments, which have been successfully applied to other electrochemical energy storage materials to elucidate dynamics information.[19-25] These challenges illustrate the value of synthesizing Ga-substituted phases of this material in order to use these ssNMR techniques to extract information about the dynamics of these systems.

Phosphorus-31 NMR was also performed on these samples which aligned nicely with what is expected from the literature.[8] Figure 4.7 shows the ^{31}P spectrum of NVPF where the large peak at 5943 ppm corresponds to P surrounded only by V^{3+} ions, while the peak at 4595 ppm belongs to P surrounded by one V^{4+} and three V^{3+} ions. The peak at ≈ 0 ppm was assigned to P surrounded by four V^{4+} ions. The ^{31}P spectrum, therefore, also confirms the presence of V^{4+} in pristine NVPF according to the literature.[8]

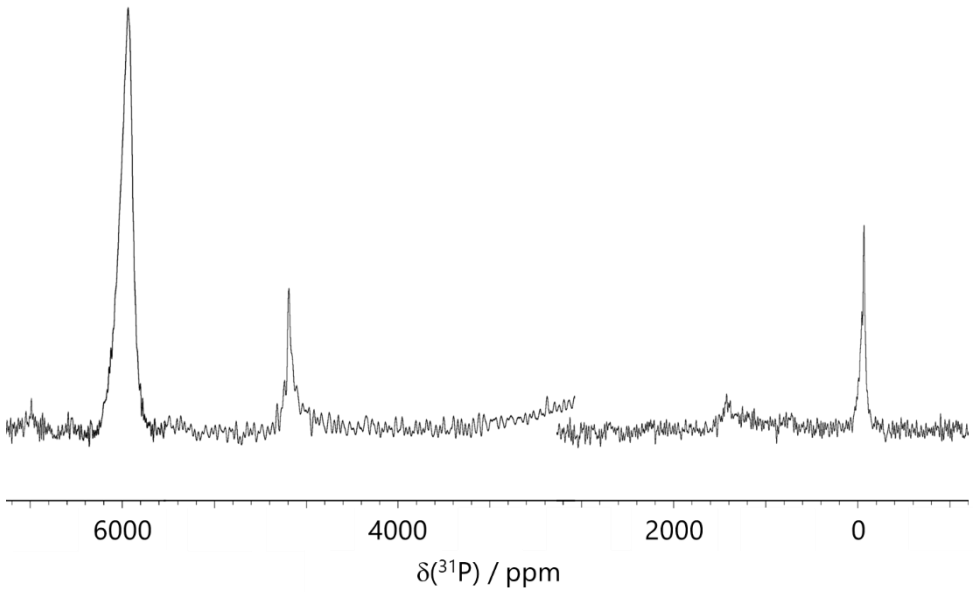

Figure 4.7 The ^{31}P spectrum of NVPF. Obtaining a sufficiently large sweep width in this spectrum was accomplished by compiling three different spectra having the same paramaters at various transmitter frequencies. Discrepencies in the baseline have been atributed to distortions due to the positions of the transmitter in that region.

While paramagnetism poses challenges to NMR analysis of NVPF, it is the paramagnetic nature of this material that makes it well suited for application in EPR. Figure 4.8 shows the EPR spectrum of NVPF. One signal is apparent in the spectrum at 3500 G. As previously discussed, EPR is incapable of seeing V^{3+} ions ($3d^2$ electron configuration) under these experimental conditions. The previously discussed O-substitution in NVPF pushes some V to the V^{4+} oxidation state, which was confirmed in the NMR spectrum in Figure 4.6. For these reasons, the signal seen in the EPR spectrum has been assigned to V^{4+}, which agrees with the literature on similar cathode materials.[15, 26] EPR has, therefore, been able to confirm the presence of V^{4+} in pristine

NVPF. This is a valuable result in that EPR is one of the few techniques that is able to visualize paramagnetic ions so unambiguously. Consequently, there is much work that can yet be done using EPR to further investigate NVPF, especially with regards to tracking charged samples during cycling. This future work will be discussed in further detail in Section 4.4, Summary and Outlook.

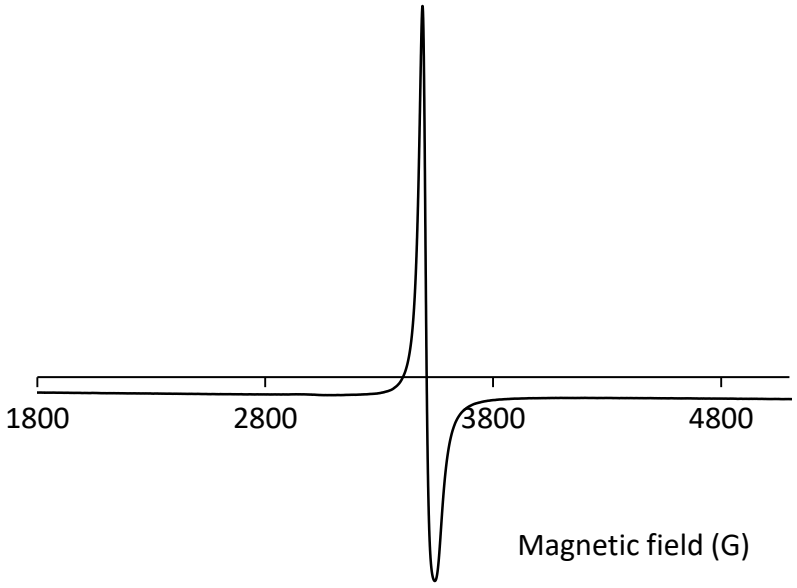

Figure 4.8 The EPR spectrum of NVPF showing one signal corresponding to V^{4+} ions

4.3.2 NVGPF

The $Na_3VGa(PO_4)_2F_3$ mixed phase material was investigated by a combination of ^{23}Na NMR, DFT calculations, and EPR. Figure 4.9c shows the NMR spectrum of the mixed

phase, as well as spectra of the NVPF parent material (Figure 4.9a) and the fully Ga-substituted material, NGPF (Figure 4.9b), which were used for peak assignment in the NVGPF spectrum. It is apparent that the NVGPF contains a region of Na surrounded by only V (pink), a region of Na surrounded by only Ga (blue), and a mixed region containing both Ga and V (green). The mixed region is denoted by two shades of green to denote two distinct types of Ga substitution in which will be explained later in further detail.

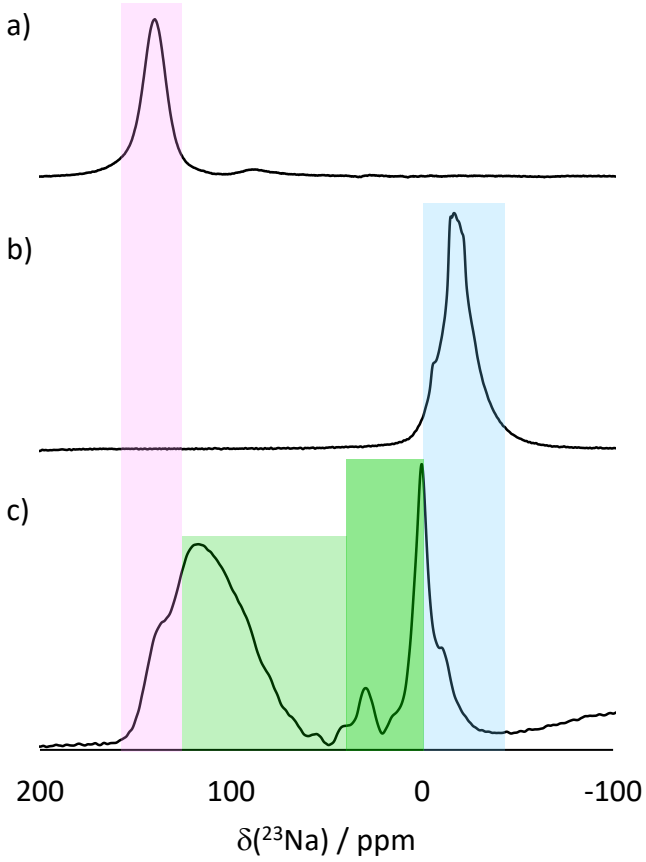

Figure 4.9 Stacked NMR spectra of a) NVPF (pink)), b) NGPF (blue), and c) the mixed phase NVGPF (green). The various regions present in NVGPF are identified by their corresponding colour.

Because there are no literature sources for NMR spectra of NVGPF, the peak assignment of the green mixed region should be confirmed by additional methods. Consequently, DFT calculations were done to elucidate the structure comprising the green mixed region of the spectrum shown in Figure 4.9. DFT calculations were done by selectively substituting out anywhere from 1 to 4 V for Ga in the unit cell and calculating

the chemical shift from the resulting optimized structure. This approach was taken because there are a total of 8 V in the unit cell, however, each Na is directly bonded through a Na-F-V bridging bond to only 4 V ions. A cross-section of the unit cell showing the Na connectivity to four neighboring V, can be seen in Figure 4.10a.

The DFT calculations yielded many interesting and informative results. Firstly, the calculations were able to confirm that partially substituting Ga for V in the NVPF structure does not significantly alter the unit cell parameters. All of the calculated unit cell parameters of the optimized structures NVGPF, NVPF, and NGPF are shown in Table 4.2. By comparing the calculated parameters to experimentally derived parameters obtained from the literature for NVPF [18] and refined in this work for NGPF, it can be determined that although there appears to be a slight overestimation in the results, the calculations generally align well with the experimental parameters. It can, therefore, be concluded that the calculated structures are representative of what is seen experimentally, and consequently, any insights gleaned from the calculations will likewise be representative of the experimentally observed results.

Table 4.2 The unit cell parameters for all calculated optimized structures of NVPF, NVGPF, and NGPF, as well as the experimentally derived parameters for NVPF from the literature [18] and NGPF, which was refined in this work

	a (Å)	**b (Å)**	**c (Å)**	**Volume (Å^3)**
Experimental NVPF [18]	9.02847(3)	9.04444(3)	10.74666(6)	877.54
Calculated NVPF	9.09926	9.15199	10.75832	895.91
Calculated NVGPF	9.05053	9.09906	10.74935	885.22
Calculated NGPF	9.00018	9.03662	10.74102	873.58
Experimental NGPF	8.89583(7)	8.89095(8)	10.64178(7)	841.6(8)

The chemical shifts for Na in unit cells with varying amounts of Ga substitution were then calculated from the optimized structures. Figure 4.10b shows a plot of the calculated chemical shifts as a function of Ga substitution. The general trend shows that increasing the amount of diamagnetic Ga^{3+} in the unit cell yields progressively lower chemical shifts. This trend is understandable when considering that V contributes positive electron density to the Na nuclei by hyperfine coupling, as previously discussed. As V is decreased, so is the amount of positive electron spin density that can be transferred to Na.

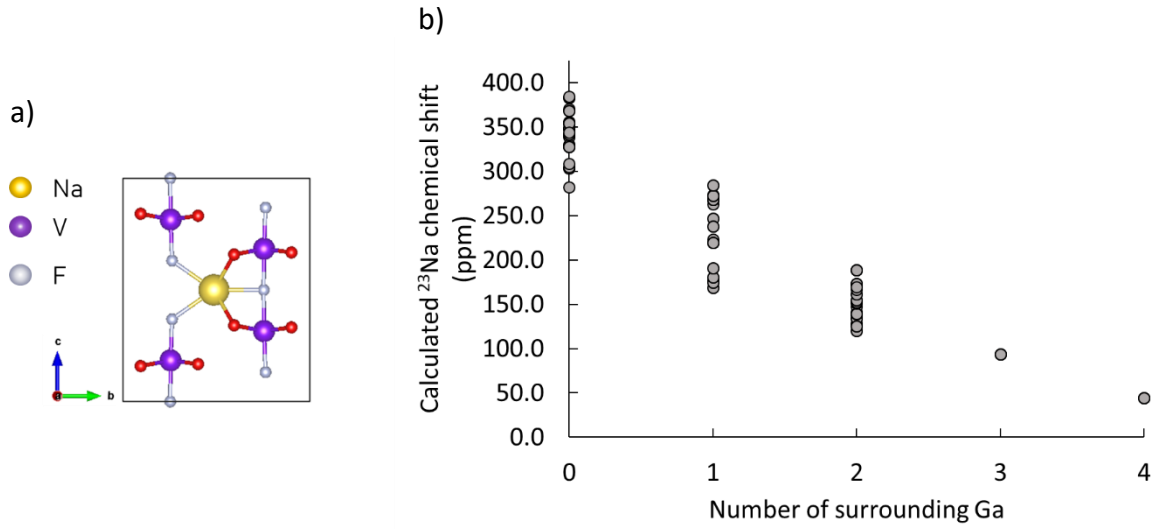

Figure 4.10 a) A cross-section of the NVPF unit cell showing the 4 neighboring V directly bonded through a Na-F-V bridging bond to Na. b) The calculated chemical shift values for various amounts of Ga substituted into the unit cell.

It should be noted that the VASP software package tends to overestimate the positive electron spin density contribution to the chemical shift, resulting in higher then expected chemical shift values.[27] Therefore, the calculated chemical shifts can only be treated qualitatively. It is still possible to compare the calculated values to the experimental mixed region, however, by scaling calculated chemical shift values to fit within the spectral region of interest. This is shown in Figure 4.11, as an overlay of a calculated chemical shift histogram on the mixed region of the NVGPF spectrum. Quite a good agreement between the calculated and experimental chemical shift values can be clearly seen. It is also important to note that for any one Ga-substitution, up to eight different Na chemical shifts could be calculated. The mixed phase region in the spectrum is, therefore, a conglomerate of many different Na environments corresponding to a

variety possible Ga-substitutions into the unit cell. The darker green area in the NVGPF spectrum has similarly been shown by calculations to belong to "Ga-rich" regions of the material. These regions consist of unit cells where the majority of the eight V in the unit cells have been substituted by Ga, with one or two V possibly remaining. Consequently, most of the Na in the unit cell will experience none or a negligible amount of positive electron spin density transfer from V so their chemical shift will be centered at zero. There will also be a few Na in these unit cells which will experience a relatively small positive spin density transfer from being near one or two V resulting in a small positive chemical shift. Hence most of the Na chemical shifts in this Ga-rich region are centred at zero with some slightly positive chemical shifts also apparent.

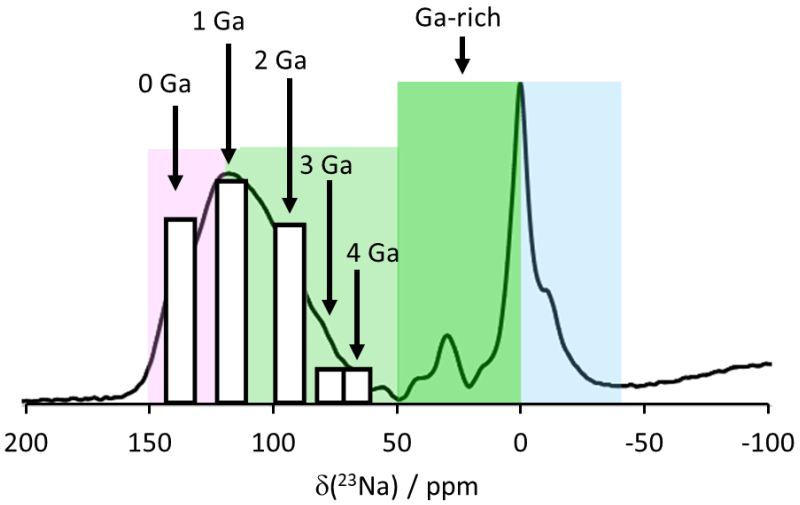

Figure 4.11 An overlay of the calculated chemical shift histogram and the NVGPF spectrum. The histogram is labeled according to the amount of Ga substituted.

Having established the structural basis for all of the regions apparent in the mixed phase spectrum, ssNMR experiments could be perfoemed to investigate Na ion dynamics in this material. A series of room temperature EXSY experiments were completed on this material, which revealed cross-peaks within the Ga-rich region of the spectrum, as can be seen in Figure 4.12a. These cross-peaks indicate that there is Na ion motion within Ga-rich regions of this material. Another set of cross peaks are also apparent in the spectra which appear at lower mixing times between the V-rich region (containing both pure NVPF and the mixed regions) and the Ga-rich region, corresponding to a Na ion exchange process. However, analysis of these cross-peaks was difficult because the T_1 of the V-rich region (in light green and pink) is very short (0.5 ms) so the peak disappears before a reasonable amount of experiments can be done to monitor cross-peak evolution over time. A detailed description of T_1 determination for this system can be found in Appendix section A.2. It also appears that the cross-peak intensities have already maximized by the first mixing time, as there is no appreciable change in normalized cross-peak intensity over the range of mixing times measured. This indicates that the exchange process present between these two regions is very fast. Unfortunately, quantification of this exchange process has remained elusive.

The cross-peaks appearing within the Ga-rich region of the spectrum, however, were quantifiable because the Ga-rich peak had a much longer T_1 (130 ms). A plot of the normalized cross-peak intensity as a function of mixing time can be fit with a first-order exponential function, $f(t)=a \cdot \mathrm{e}^{(\mathrm{bt})} + c$, which is shown as the red dashed line in Figure

4.12b. The calculated fit yielded a Na ion exchange rate of $(8 \pm 2) \times 10^2$ Hz. For comparison, similar materials have demonstrated ion exchange rates usually less than 200 Hz.[19-20, 22, 24] This exceptionally fast exchange rate along with the previously discussed unquantifiable fast cross-peak exchange prove that NVGPF is a very dynamic material. Fast ion motion is necessary to produce high power batteries. These results, therefore, demonstrate the effectiveness of this material for battery applications.

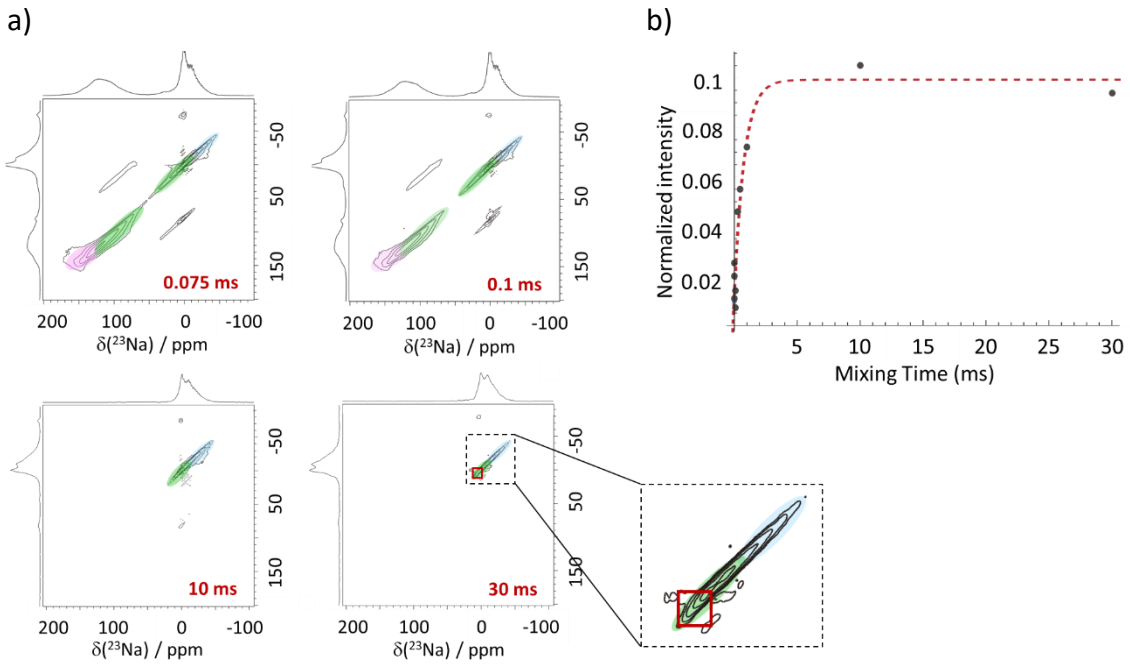

Figure 4.12 a) A sampling of the EXSY experiments of NVGPF with one of the cross-peaks expanded and outlined for clarity. b) The exponential fit (red, dashed line) to the normalized EXSY cross peak intensities as a function of mixing times.

While it would be ideal to repeat these experiments at variable temperatures to extract a Na ion exchange rate through the Arrhenius relationship between exchange

rate and temperature, this was not possible for this material. At increased temperatures, as low as 312 K, the V-rich peak in the spectrum migrated towards the Ga-rich peak. However, when the temperature was again lowered the peak would move back to its original position. What was even more peculiar was that the peak seemed to migrate closer to the Ga-rich peak when left for longer periods of time at a higher temperature. This behaviour could relate to some sort of structural instability at higher temperatures. However, this phenomenon was not investigated any further as the focus of this project shifted towards synthesizing a more homogenous phase of this material, h-NVGPF.

NVGPF was also investigated using EPR. Similar to what was discussed for EPR of NVPF, only V^{4+} resulting from O-substitution would be expected to appear in the spectrum. The EPR spectrum for the mixed phase material can be seen in Figure 4.13. Indeed, the same central peak is apparent at 3475 G corresponding with V^{4+}. The spectrum also shows what appears to be hyperfine splitting of this signal which is believed to be caused by symmetrically equivalent V in different structural environments.[28] This would be a logical assignment of the observed signals for NVGPF, where one would expect to have only one V oxidation state (4+) that could be surrounded by any number of Ga throughout the structure. This EPR spectrum, therefore, confirms the results from the DFT calculations and NMR spectra that Ga is not evenly distributed throughout this material.

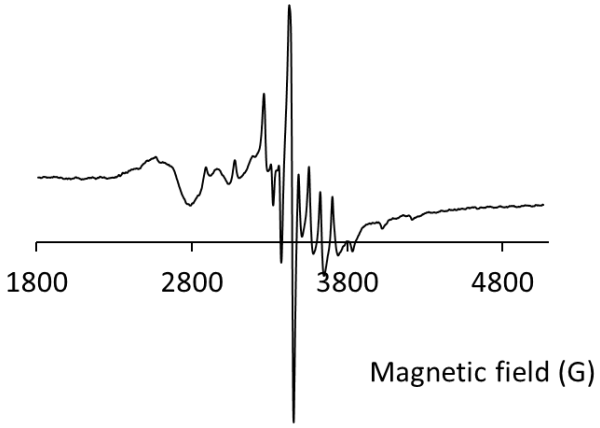

Figure 4.13 The EPR spectrum of NVGPF

4.3.3 h-NVGPF

The homogenized sample of NVGPF, h-NVGPF was also analyzed using EXSY experiments to determine if ion dynamics behaved similarly to what was observed in the less homogenized sample. Figure 4.14 shows an EXSY spectrum of h-NVGPF at 0.035 ms mixing time. Cross-peaks, like those observed in NVGPF, are again evident between the V-rich and Ga-rich regions and at a very short mixing time. However, because the regions are much more closely intermixed in h-NVGPF than in NVGPF, both the diagonal and cross-peaks severely overlap with each other, making it difficult to potentially quantify cross-peak intensity. Regardless, it is important to realize that similar Na ion dynamics appear in h-NVGPF as they do in NVGPF.

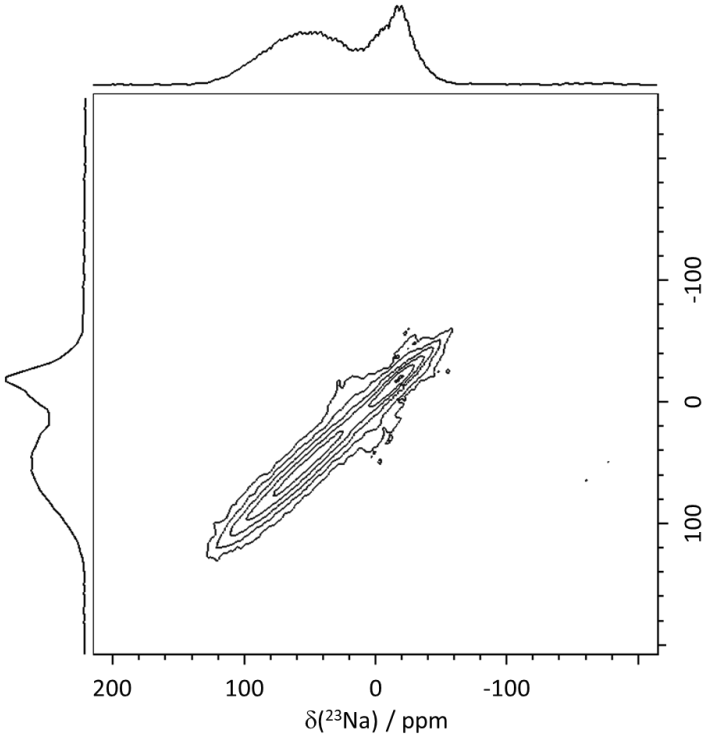

Figure 4.14 An EXSY spectrum of h-NVGPF at 0.035 ms mixing time

A phosphorous-31 spectrum was collected of h-NVGPF which revealed some interesting results. The spectrum showed in Figure 4.15 is the same as the spectrum shown in Figure 4.5 but with the region around zero expanded for clarity. The peaks centred at zero are relatively sharp compared to the significantly broader peaks observed in the NVPF ^{31}P spectrum (Figure 4.7). It is, therefore, likely that these peaks correspond with P surrounded by varying amounts of diamagnetic Ga, as the effects of paramagnetic broadening are not observed. Regions of the spectrum at higher chemical shifts are not shown because the signal-to-noise ratio was not sufficiently large enough to observe broadened paramagnetic peaks which would appear in those regions. The ^{31}P

spectrum of h-NVGPF is, accordingly, able to confirm the presence of multiple different Ga-substitution environments in h-NVGPF.

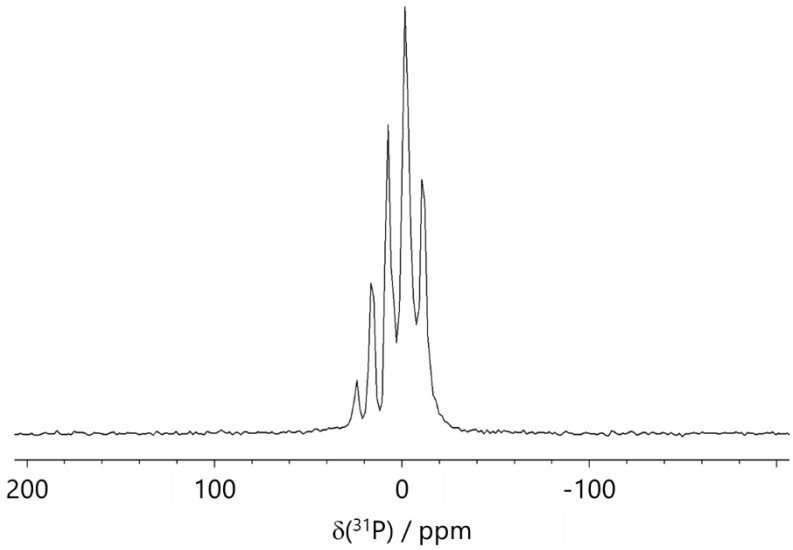

Figure 4.15 The ^{31}P spectrum of h-NVGPF showing a number of sharp peaks centred around zero

After determining the structure and dynamics in the pristine mixed phase material, the next natural step in understanding this family of cathodes is to analyze electrochemically cycled materials. SIBs were consequently made of h-NVGPF, and charged to 1.4, 3.7, and 4.5 V, corresponding to expected voltage plateaus suggested by the literature.[9] NMR spectra of the cycled and pristine cathode materials can be seen in

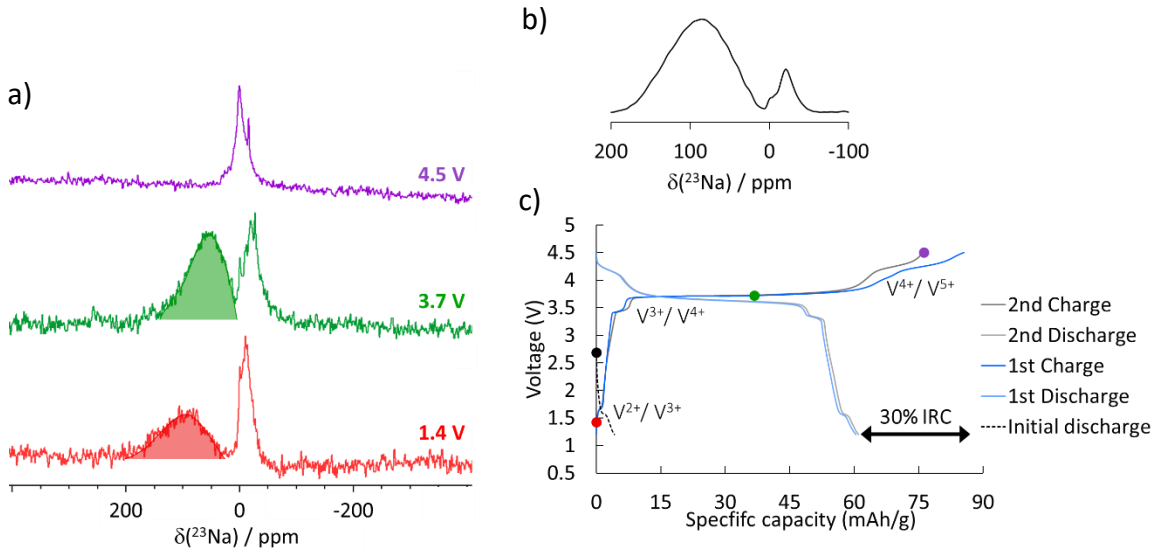

Figure 4.16 Figure 4.14 a) A series of NMR spectra of cycled h-NVGPF at 1.4 V (red), 3.7 V (green), and 4.5 V (purple). The peak areas in the 1.4 and 3.7 V spectra were highlighted to illustrate that the equivalent peak in the 1.4 V spectrum is broader than that observed in the 3.7 V spectrum. b) The NMR spectrum of pristine h-NVGPF. c) The charge and discharge curves for h-NVGPF showing the three points at which the correcponding (by colour) NMR spectra in b) were taken, the initial point of pristine h-NVGPF (black), and the irreversible capacity loss.

Figure 4.16a and 4.16b, respectively. The sharp peak that appears at -16 ppm in the cycled samples corresponds to $NaPF_6$ salt remaining on the electrode surface.[29-30] The general trend in the spectra illustrates that as V^{3+} is oxidized during cycling it becomes less paramagnetic as V^{4+} and finally diamagnetic as V^{5+} due to the observed chemical shift trend towards zero. The V^{3+} and V^{4+} present in these samples will paramagnetically contribute to a positive Na chemical shift, whereas peaks corresponding to Na surrounded by diamagnetic V^{5+} will cluster around zero. Further electrochemical and EPR measurements can be done to confirm this preliminary peak assignment. The

electrochemical charge curve shown in Figure 4.16c, appears to corroborate this peak assignment as well because three distinct voltage plateaus are visible at 1.6 V, 3.4 V, and 4.2 V, which have been assigned to the V^{2+}/V^{3+}, V^{3+}/V^{4+}, and V^{4+}/V^{5+} redox couples according to a calculated fit to the charge curve.[9] In the literature, the lowest voltage plateau corresponds with Na insertion into the material. It is, therefore, possible to conclude that substituting out some of the V in this material for electrochemically inactive Ga, forces the V-oxidation state of those remaining V ion beyond the $V^{3+/4+}$ oxidation couple in order to maintain charge balance throughout the desodiation process. This may be apparent in the NMR spectrum taken at 1.4 V, where the V-rich peak (highlighted in red) appears broader than the equivalent peak in the 3.7 V spectrum (highlighted in green). This broadness may be attributed to additional paramagnetic effects by V^{2+} ions which exist due to Na insertion at low voltages. This result aligns well with a similar observation outlined in more recent literature on the parent NVPF material, where intentional Na disordering was introduced into the structure through controlled Na insertion at low voltages resulting in the reversible extraction of all three Na from the structure in a voltage window of 1 – 4.8 V by means of the V^{3+},V^{4+}, and V^{5+} oxidation pathway.[31] Considering the results found in this work, it can be hypothesized that Ga has a similar effect in the structure of h-NVGPF, where it induces a certain amount of disorder into the structure allowing for the activation of a larger range of V oxidation states upon desodiation. Further studies would have to be done to confirm these results, as well quantify the differences between spectra taken at

different voltages, which will be discussed in Section 4.4, Summary and Outlook. This may confirm that an important next stage in materials development of SIB cathodes is to investigate disordered materials, which may open up a new avenue for high capacity SIB cathode development.

Further analysis of the h-NVGPF charge curve in Figure 4.16c, however, reveals that there is some discrepancy with what is expected from the literature. Firstly, the irreversible capacity loss (IRC) between the first and second cycle is very significant (30%), which does not appear to be the case from comparable cycling curves in the literature.[9] Additionally, the specific capacity for this material was found to be 72 mAh/g, which differs quite extensively from the literature value for NVGPF of 144 mAh/g.[9] The only considerable difference between the samples analyzed in the literature and in this work is in the synthetic method. As previously discussed, the sample in the literature was synthesized by ball milling for 24 hours, however, NMR and DFT calculations of that material revealed that V and Ga were not homogenously distributed throughout the material. Batteries made in this work used cathode samples made of h-NVGPF, which was shown by NMR to contain a more homogeneous distribution of V and Ga after ball milling for a linger period of time. It is, therefore, possible that the relative degree of homogeneity of Ga substitution into this material is quite impactful on its electrochemical performance. It should also be noted that the current supplied to these batteries during cycling was calculated using an assumed specific capacity of 141 mAh/g at a rate of C/20, according to the literature.[9] The actual

observed timescale for charging and discharging, however, was more consistent with a rate of C/10, indicating that the applied current was too high for this material. The inability for Na to reinsert into the structure upon continual cycling, resulting in a large IRC, may be one effect of applying too high a current within the time allowed for charging. Interestingly, the observed specific capacity of 72 mAh/g is consistent with the expected specific capacity of NVGPF if no Na insertion occurred at low voltages, which based on its stoichiometry would be half that of the NVPF parent compound (≈ 90 mAh/g).[9] A possible explanation then for the worsened electrochemical performance of h-NVGPF in comparison to NVGPF in the literature, which is consistent with the previous discussion of the impact of Ga substitution, is that homogeneously mixing V and Ga throughout the crystal structure reduces the overall disorder compared to inhomogeneous NVGPF, and consequently, limits the potential for Na insertion at low voltages, thus limiting the specific capacity. In order to further elucidate the electrochemical behaviour of h-NVGPF in comparison to NVGPF, a series of electrochemical measurements must be done on both the homogenized sample h-NVGPF with a lower applied current, and less homogenized sample NVGPF as demonstrated in the literature.

4.3.4 NGPF

The fully Ga-substituted phase, NGPF, was also investigated by means of ssNMR. The one-dimensional spectrum can be seen in Figure 4.17. While it was believed that

removing all paramagnetic V ions from the structure would resolve individual sites in the observed NMR spectrum, this was not this case. Instead only one peak with a distinct shoulder is visible. This is most likely due to the three Na in the structure having very similar environments, causing their peaks to overlap.

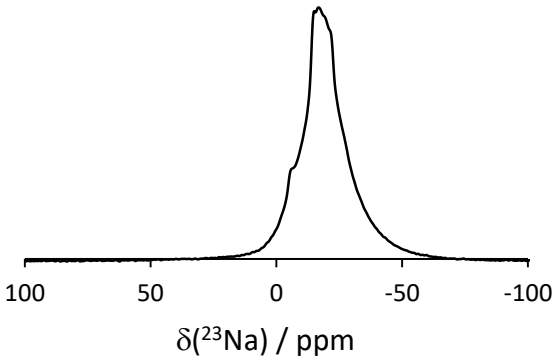

Figure 4.17 The ^{23}Na ssNMR spectrum of NGPF

Although there is no site resolution for the NGPF sample, a series of variable temperature EXSYs were done with the aim to observe any ion dynamics between sites within the single peak. Example spectra taken at three different temperatures can be seen in Figure 4.18. Unfortunately, across all temperatures no Na-ion dynamics were visible in the form of cross-peaks. A possible explanation for the lack of observable dynamics in NGPF is the decreased unit cell size upon complete Ga-substitution into the parent NVPF structure. The unit cell parameters previously shown in Table 4.1 reveal that the refined unit cell parameters for NGPF are generally smaller than those of the

NVPF parent compound. NGPF's unit cell volume is 841.6(8) $Å^3$ while that of NVPF is 877.54 $Å^3$, corresponding to an overall 4% decrease in unit cell volume. The decreased unit cell size may correspond to smaller Na diffusion pathways within the unit cell. This size decrease may be sufficient to increase the energy barrier to the point where Na diffusion in the unit cell becomes unfavorable.

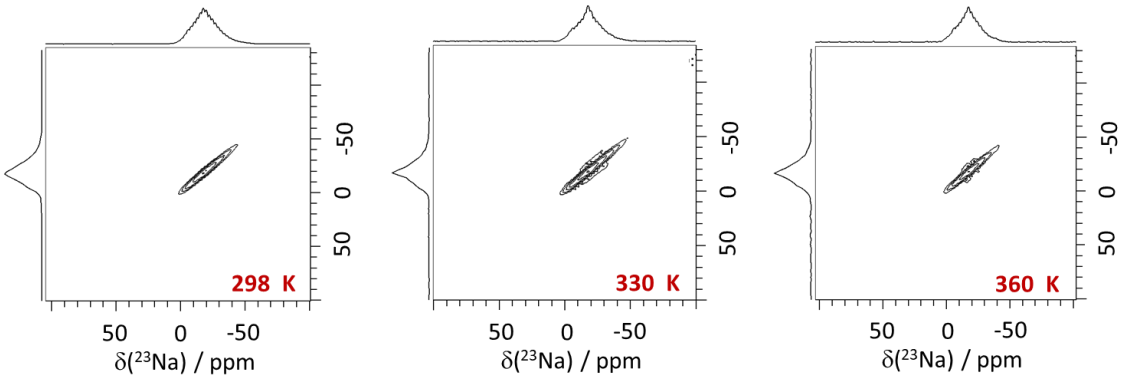

Figure 4.18 EXSY experimental spectra (30 ms mixing times) of NGPF performed at three different temperatures which are shown in red at the bottom righ corner of each spectrum

4.4 Summary and Outlook

The results presented in this chapter outline the work done to understand the promising series of SIB cathode materials stemming from $Na_3V_2(PO_4)_2F_3$. This work has demonstrated the relevance of using a combination of NMR, EPR and DFT calculations to study complex cathode materials. The parent compound, NVPF, although being inherently difficult to study using NMR, was analyzed using EPR, and the presence of V^{4+}

in the pristine material was confirmed. Extremely fast Na-ion motion was found in the partially Ga-substituted mixed phase material using ^{23}Na EXSY NMR experiments. A structural understanding of the mixed phase was obtained using DFT calculations, which confirmed that V and Ga are not homogeneously mixed together in the material that was previously reported in the literature.[9] EPR experiments also suggested inhomogeneous V^{4+} environments. A more homogenous mixed phase sample was synthesized, h-NVGPF, which showed similar Na ion dynamic characteristics as NVGPF. NMR was then used to verify the existence of V^{4+} and V^{5+} at high charge states in charged h-NVGPF, which provides experimental verification of the previously calculated results.[9] Overall, this research demonstrates the effectiveness of using several different techniques in addition to ssNMR to thoroughly explore challenging and promising Na-ion battery cathode materials. However, there is still much work to obtain a thorough understanding of this family of materials. Detailed explanations of the suggested work moving forward will be outlined for each material below.

4.4.1 NVPF

The challenges to studying NVPF using NMR are nicely overcome by using EPR. Consequently, there is much potential for effectively using EPR to track V ion oxidation throughout cycling. In the case of NVPF, cycling is expected to occur through the $V^{3+/4+}$ redox couple, which could be monitored by an increasing intensity of the observed V^{4+} peak during charging corresponding with the formation of V^{4+}. Likewise, a decrease in

intensity during discharge would indicate conversion of V^{4+} back to V^{3+}. Similar work was successfully done to analyze NVP cathodes during cycling.[15] Additionally, although Na ion dynamics were not visible on the NMR time scale in pristine NVPF, it may be possible that cycled NVPF would demonstrate observable ion dynamics. EXSY experiments should, therefore, be attempted on cycled NVPF.

4.4.2 Mixed phase materials, NVGPF and h-NVGPF

Very little work remains to be done on inhomogeneous NVGPF. Collecting additional points in the T_1 data could help obtain a better fit, and perhaps extract out the exchange process occurring in the material at short mixing times. It may also be possible to do a series of low temperature EXSYs to see a clear build up of cross-peak intensities between the V-rich and Ga-rich peaks, which could then be fit to extract an exchange rate. It may be interesting to do bulk exchange measurements for this material as well, such as PFG NMR experiments to measure diffusivity, to determine if the fast ion exchange rate observed within the unit cell is consistent throughout the bulk material.

There is much work that can yet be done in the analysis of h-NVPGF. Continued electrochemical cycling and subsequent characterization by NMR is crucial. Information provided by these experiments can help determine the V oxidation states throughout cycling, if there is any preference for Na extraction from V-rich or Ga-rich regions, and, with the aid of DFT calculations, if any structural changes occur during cycling. It may

also be interesting to do EXSY experiments on cycled cathodes of h-NVGPF to determine if any new Na exchange mechanisms arise throughout cycling, which would be evidenced by the formation on new cross-peaks as compared to the pristine material. It should be noted that in order to be able to make accurate and quantifiable comparisons between NMR spectra of cathode materials from different batteries, the spectra must be weight calibrated and collected using the same number of scans. EPR will also be a valuable technique to analyze cycled h-NVGPF, as it should be able to confirm the presence of V^{2+} in addition to V^{4+}.

In order to investigate if Ga-induced distortions in the structure are the reason additional V oxidation states are accessible during cycling, a series of cathode materials should be synthesized of the general form $Na_3V_{2-x}Ga_x(PO_4)_2F_3$ with varying values of x. These materials can then be analyzed similarly to NVGPF and h-NVGPF to determine the relationship between structure and electrochemical performance.

4.4.3 NGPF

Because NGPF had not been synthesized in a pure form prior to this project, future work involving this material will be more focused on elucidating the structure. A valuable NMR technique that can be implemented to elucidate the structure of NGPF is multiple-quantum magic-angle spinning (MQMAS). MQMAS has the potential to resolve overlapping quadrupole peaks by separating the quadrupole interaction from other

chemical shift determining interactions such as dipolar coupling and chemical shift anisotropy.[32] Using MQMAS may, therefore, make it possible to determine the chemical shifts and quadrupole parameters for all unique sties buried under the one broad peak observed in the spectrum. It may also be possible to obtain the quadrupole parameters for this peak by fitting these parameters at various field strengths.

4.5 References

1. Ellis, B. L.; Nazar, L. F., Sodium and sodium-ion energy storage batteries. *Current Opinion in Solid State and Materials Science* **2012,** *16* (4), 168-177.
2. Kundu, D.; Talaie, E.; Duffort, V.; Nazar, L. F., The emerging chemistry of sodium ion batteries for electrochemical energy storage. *Angew Chem Int Ed Engl* **2015,** *54* (11), 3431-48.
3. Hwang, J. Y.; Myung, S. T.; Sun, Y. K., Sodium-ion batteries: present and future. *Chemical Society reviews* **2017,** *46* (12), 3529-3614.
4. Palomares, V.; Serras, P.; Villaluenga, I.; Hueso, K. B.; Carretero-González, J.; Rojo, T., Na-ion batteries, recent advances and present challenges to become low cost energy storage systems. *Energy & Environmental Science* **2012,** *5* (3), 5884.
5. Chayambuka, K.; Mulder, G.; Danilov, D. L.; Notten, P. H. L., Sodium-Ion Battery Materials and Electrochemical Properties Reviewed. *Advanced Energy Materials* **2018,** *8* (16).
6. Zhu, C.; Wu, C.; Chen, C.-C.; Kopold, P.; van Aken, P. A.; Maier, J.; Yu, Y., A High Power–High Energy Na3V2(PO4)2F3 Sodium Cathode: Investigation of Transport Parameters, Rational Design and Realization. *Chemistry of Materials* **2017,** *29* (12), 5207-5215.
7. Bianchini, M.; Fauth, F.; Brisset, N.; Weill, F.; Suard, E.; Masquelier, C.; Croguennec, L., Comprehensive Investigation of the Na3V2(PO4)2F3–NaV2(PO4)2F3 System by Operando High Resolution Synchrotron X-ray Diffraction. *Chemistry of Materials* **2015,** *27* (8), 3009-3020.
8. Broux, T.; Bamine, T.; Fauth, F.; Simonelli, L.; Olszewski, W.; Marini, C.; Ménétrier, M.; Carlier, D.; Masquelier, C.; Croguennec, L., Strong Impact of the Oxygen Content in Na3V2(PO4)2F3–yOy (0 ≤ y ≤ 0.5) on Its Structural and Electrochemical Properties. *Chemistry of Materials* **2016,** *28* (21), 7683-7692.
9. Matts, I. L.; Dacek, S.; Pietrzak, T. K.; Malik, R.; Ceder, G., Explaining Performance-Limiting Mechanisms in Fluorophosphate Na-Ion Battery Cathodes through Inactive Transition-Metal Mixing and First-Principles Mobility Calculations. *Chemistry of Materials* **2015,** *27* (17), 6008-6015.
10. Broux, T.; Bamine, T.; Simonelli, L.; Stievano, L.; Fauth, F.; Ménétrier, M.; Carlier, D.; Masquelier, C.; Croguennec, L., VIV Disproportionation Upon Sodium Extraction From Na3V2(PO4)2F3 Observed by Operando X-ray Absorption Spectroscopy and Solid-State NMR. *The Journal of Physical Chemistry C* **2017,** *121* (8), 4103-4111.
11. Shannon, R., Revised effective ionic radii and systematic studies of interatomic distances in halides and chalcogenides. *Acta Crystallographica Section A* **1976,** *32* (5), 751-767.
12. Abragam, A.; Pryce, M. H. L., Theory of the nuclear hyperfine structure of paramagnetic resonance spectra in crystals. *Proceedings of the Royal Society of London. Series A. Mathematical and Physical Sciences* **1951,** *205* (1080), 135-153.
13. Weil, J. A.; Bolton, J. R., *Electron paramagnetic resonance: elementary theory and practical applications*. John Wiley & Sons: 2007.
14. Oversluizen, G.; Metselaar, R., ESR and optical absorption spectra of reduced vanadium ions in Ca2NaMg2V3O12garnet. *Journal of Physics C: Solid State Physics* **1982,** *15* (23), 4869-4880.
15. Nizamov, F. A.; Togulev, P. N.; Abdullin, D. R.; Khantimerov, S. M.; Balaya, P.; Suleimanov, N. M., Antisite defects and valence state of vanadium in Na3V2(PO4)3. *Physics of the Solid State* **2016,** *58* (3), 475-480.

16. Koller, H.; Engelhardt, G.; Kentgens, A. P. M.; Sauer, J., 23Na NMR Spectroscopy of Solids: Interpretation of Quadrupole Interaction Parameters and Chemical Shifts. *The Journal of Physical Chemistry* **1994,** *98* (6), 1544-1551.
17. Shakoor, R. A.; Seo, D.-H.; Kim, H.; Park, Y.-U.; Kim, J.; Kim, S.-W.; Gwon, H.; Lee, S.; Kang, K., A combined first principles and experimental study on Na3V2(PO4)2F3 for rechargeable Na batteries. *Journal of Materials Chemistry* **2012,** *22* (38), 20535.
18. Bianchini, M.; Brisset, N.; Fauth, F.; Weill, F.; Elkaim, E.; Suard, E.; Masquelier, C.; Croguennec, L., Na3V2(PO4)2F3 Revisited: A High-Resolution Diffraction Study. *Chemistry of Materials* **2014,** *26* (14), 4238-4247.
19. Davis, L. J. M.; Ellis, B. L.; Ramesh, T. N.; Nazar, L. F.; Bain, A. D.; Goward, G. R., 6Li 1D EXSY NMR Spectroscopy: A New Tool for Studying Lithium Dynamics in Paramagnetic Materials Applied to Monoclinic Li2VPO4F. *The Journal of Physical Chemistry C* **2011,** *115* (45), 22603-22608.
20. Davis, L. J. M.; Goward, G. R., Differentiating Lithium Ion Hopping Rates in Vanadium Phosphate versus Vanadium Fluorophosphate Structures Using 1D 6Li Selective Inversion NMR. *The Journal of Physical Chemistry C* **2013,** *117* (16), 7981-7992.
21. Langer, J.; Smiley, D. L.; Bain, A. D.; Goward, G. R.; Wilkening, M., An Unexpected Pathway: 6Li-Exchange NMR Spectroscopy Points to Vacancy-Driven Out-of-Plane Li-Ion Hopping in Crystalline Li2SnO3. *The Journal of Physical Chemistry C* **2016,** *120* (6), 3130-3138.
22. Smiley, D. L.; Davis, L. J. M.; Goward, G. R., An Improved Understanding of Li+ Hopping Pathways and Rates in Li3Fe2(PO4)3 Using Selective Inversion 6Li NMR Spectroscopy. *The Journal of Physical Chemistry C* **2013,** *117* (46), 24181-24188.
23. Smiley, D. L.; Tessaro, M. Z.; He, X.; Goward, G. R., Correlation of Electrochemical Performance with Lithium Environments and Cation Dynamics in Li2(Mn1–yFey)P2O7 using 6Li Solid-State NMR. *The Journal of Physical Chemistry C* **2015,** *119* (29), 16468-16474.
24. Cahill, L. S.; Chapman, R. P.; Britten, J. F.; Goward, G. R., 7Li NMR and Two-Dimensional Exchange Study of Lithium Dynamics in Monoclinic Li3V2(PO4)3. *The Journal of Physical Chemistry B* **2006,** *110* (14), 7171-7177.
25. Davis, L. J. M.; Heinmaa, I.; Goward, G. R., Study of Lithium Dynamics in Monoclinic Li3Fe2(PO4)3using6Li VT and 2D Exchange MAS NMR Spectroscopy†. *Chemistry of Materials* **2010,** *22* (3), 769-775.
26. Li, C.; Shen, M.; Lou, X.; Hu, B., Unraveling the Redox Couples of VIII/VIV Mixed-Valent Na3V2(PO4)2O1.6F1.4 Cathode by Parallel-Mode EPR and In Situ/Ex Situ NMR. *The Journal of Physical Chemistry C* **2018,** *122* (48), 27224-27232.
27. Hafner, R.; Spisak, D.; Lorenz, R.; Hafner, J., Does density-functional theory predict a spin-density-wave ground state for Cr? *Journal of Physics: Condensed Matter* **2001,** *13* (11), L239.
28. Weil, J. A.; Bolton, J. R., Electron paramagnetic resonance : elementary theory and practical applications. **2007**.
29. Coquil, G.; Fraisse, B.; Dupré, N.; Monconduit, L., Versatile Si/P System as Efficient Anode for Lithium and Sodium Batteries: Understanding of an Original Electrochemical Mechanism by a Full XRD-NMR Study. *ACS Applied Energy Materials* **2018,** *1* (8), 3778-3789.
30. Delville, A.; Stover, H. D. H.; Detellier, C., Crown ether-cation decomplexation mechanics. Sodium-23 NMR studies of the sodium cation complexes with dibenzo-24-crown-8 and dibenzo-

18-crown-6 in nitromethane and acetonitrile. *Journal of the American Chemical Society* **1987,** *109* (24), 7293-7301.
31. Yan, G.; Mariyappan, S.; Rousse, G.; Jacquet, Q.; Deschamps, M.; David, R.; Mirvaux, B.; Freeland, J. W.; Tarascon, J. M., Higher energy and safer sodium ion batteries via an electrochemically made disordered Na3V2(PO4)2F3 material. *Nature communications* **2019,** *10* (1), 585.
32. Engelhardt, G.; Kentgens, A. P. M.; Koller, H.; Samoson, A., *Strategies for extracting NMR parameters from MAS, DOR and MQMAS spectra. A case study for Na4P2O7*. 2000; Vol. 15, p 171-80.

Chapter 5: Summary and Outlook

5.1 Summary

With the development and implementation of technology drastically on the rise, scientists must consider what long-term consequences these technologies will have on the world. The vast majority of current technologies are primarily powered by energy from fossil fuel combustion. Unless renewable energy sources can be implemented on the large-scale, this rise in technological advancement will severely contribute to the negative environmental impacts of fossil fuel combustion. Batteries have thus emerged as one of the most promising electrochemical energy storage mechanisms, which will aid in the widespread adoption of renewable energy.

As research interest in batteries has increased, every component of the battery has been investigated in turn in order to improve the overall electrochemical performance of the battery. In general, battery research can focus on either the development of new materials or the investigation of current materials to determine the structural characteristics responsible for their observed electrochemical behaviour. This thesis has focused on the latter, where the information gleaned from the investigations herein will guide the informed development of future high-performance battery materials. The scope of this work was relatively broad, employing techniques in inorganic materials synthesis and characterization, as well as aspects of physical chemistry to exploit the magnetic moments of atomic particles to yield dynamics and crystal structure

information. Alkali ion battery cathode materials were the focus of interest, where the mobile ions were analyzed using various magnetic resonance techniques. *Ab initio* calculations were also performed to enable more thorough interpretation of experimental results. The Ni-rich NMC622 LIB cathode was explored using ssNMR to reveal local ordering in the pristine material. The SIB cathode family $Na_3V_{2-x}Ga_x(PO_4)_2F_3$ were investigated with a combination of ssNMR, EPR, and DFT calculations, which proved that the full V-oxidation range is accessible during electrochemical cycling. This was also the first instance of ssNMR and EPR being performed on Ga-substituted variants of this promising family of cathodes. Overall, the work presented in this thesis further demonstrates the viability of applying ssNMR in paramagnetic and quadrupolar electrochemical materials. This work also contributes to the knowledge base of cathode materials for both LIB and SIBs, with regards to establishing the structural correlation to electrochemical performance.

5.2 Contributions and Outlook

5.2.1 Investigating the Relationship Between Structure and Charge State in NMC622

The Ni-rich LIB cathode NMC622 was analyzed, and it was confirmed that a combined NMR and statistical Monte Carlo calculations approach was highly effective in obtaining structural information from complicated, disordered cathode materials. This approach was especially valuable for these materials because the paramagnetic redox

active metals produced extremely broad and undefined spectra of pristine and cycled materials. Monte Carlo simulations were able to illuminate the relationship between the ionic arrangement of TMs in the NMC622 TM layers and the observed NMR spectra. The calculated spectra showed good agreement in the pristine and low SOC materials. When the structure solution from Monte Carlo calculations for the pristine material was analyzed, it was found that a phase separation of ion clusters was present. The two distinct ion clusters consisted of regions containing either NMC111-like ion arrangement or Ni^{3+}/Co^{3+} regions. This result corroborated similar observations for other Ni-rich materials, where charge balance is best achieved by ionic clustering.

The Monte Carlo simulation method currently employed, however, did not produce experimentally comparable results for all data sets. The simulated spectra did not appear to fit experimental spectra at high SOCs. In order to successfully apply this technique across the full cycling range, the calculation code must be improved. The calculations can theoretically be altered in two ways to improve the fit with experimental spectra. Firstly, simulated structures can indiscriminately allow delithiation from both M^{3+} and NMC111 regions. Secondly, the calculations could force delithiation from M^{3+} regions before allowing it in NMC111 regions. The resulting high SOC simulated spectra from each calculation method which best model experimental spectra will inform the delithiation pathway that occurs in NMC622. These altered calculations may also provide insight into the preferred Ni-oxidation pathway, where a good fit between simulated and experimental spectra for indiscriminate delithiation from both

NMC111 and M^{3+} regions would indicate that Ni^{2+} and Ni^{3+} are oxidized simultaneously during cycling. Alternatively, a good fit for calculations where delithiation was initially forced from M^{3+} regions, would indicate a stepwise mechanism where Ni^{3+} is oxidized to Ni^{4+} before Ni^{2+} is accessed.

The work done on NMC622 demonstrated the viability of ssNMR informed Monte Carlo calculations to interpret the structural relationship to electrochemical behaviour in NMC cathode materials. The presence of ion clustering was found in pristine NMC622. Once the calculations have been altered to better fit experimental spectra, information about ionic clustering and preferred delithiation methods will be able to inform the strategic advancement of the next generation of Ni-rich LIB cathode materials.

5.2.2 A Magnetic Resonance Study of a Promising Family of Sodium Ion Battery Cathode Materials, $Na_3V_{2-x}Ga_x(PO_4)_2F_3$

Various experiments were done, as outlined in Chapter 4, to gain insight into the promising family of SIB cathode materials with the general form, $Na_3V_{2-x}Ga_x(PO_4)_2F_3$. In this work a combination of powder XRD, NMR, EPR and DFT calculations were employed to provide complimentary information about the crystal structures and ion dynamics within these materials. The NVPF parent compound was inherently difficult to analyze using NMR, due to the substantial paramagnetic effects of the V^{3+} ion. Consequently, NVPF was studied using EPR, which unambiguously confirmed the presence of V^{4+} ions in

the pristine material. Na-ion dynamics were investigated in the partially Ga-substituted mixed phase material by means of ^{23}Na EXSY NMR experiments, which revealed extremely fast Na-ion motion can occur throughout the various regions of this material. DFT calculations were then implemented to understand the structural correlation with the observed NMR spectrum of the mixed phase, which showed that V and Ga are not homogeneously mixed throughout the material as was previously reported.[1] EPR experiments of the mixed phase also suggested a variety of V^{4+} environments, again indicating an inhomogeneous distribution of V and Ga in the mixed phase. A homogenous mixed phase sample, h-NVGPF, which displayed similar Na ion dynamic behaviour as NVGPF. Following electrochemical cycling of h-NVGPF, NMR indicated the presence of V^{4+} and V^{5+} at a high SOC, which experimentally verified previously calculated results.[1] These results, overall, demonstrated the efficacy of using a variety of techniques to comprehensively research these challenging SIB cathode materials. Cathode materials belonging to the $Na_3V_{2-x}Ga_x(PO_4)_2F_3$ family have proven to be highly dynamic, and therefore, ideal for SIB applications.

To obtain a complete understanding of this family of cathodes, however, more work must be done. This work was outlined in detail in the Section 4.4, however, it will be summarized here. EPR can be done to track V-oxidation states throughout cycling in NVPF and h-NVGPF. Variable temperature EXSY experiments of NVGPF can be performed to further quantify Na-ion dynamics. Continued NMR analysis of cycled h-NVGPF will potentially yield information about dynamics as well as ionic and structural evolution

during cycling. Additional syntheses can be done to vary the value of x in $Na_3V_{2-x}Ga_x(PO_4)_2F_3$, which may reveal an optimal amount of Ga-substitution to maximize the electrochemical performance of this family of cathodes. Furthermore, the crystal structure of NGPF can be investigated by various NMR techniques to reveal insights into the parent NVPF compound.

5.3 Concluding Remarks

Throughout this thesis ssNMR was primarily used to probe the relationship between crystal structure and electrochemical behaviour in LIB and SIB cathode materials. The complexities of these materials necessitated the use of complimentary magnetic resonance and computational methods. This research is valuable in that it demonstrates a toolkit of magnetic resonance-based techniques to further investigate alkali ion cathode materials. These results contribute to the larger battery community by providing a deeper understanding of the mechanisms responsible for the impressive performance of these cathode materials.

5.4 References

1. Matts, I. L.; Dacek, S.; Pietrzak, T. K.; Malik, R.; Ceder, G., Explaining Performance-Limiting Mechanisms in Fluorophosphate Na-Ion Battery Cathodes through Inactive Transition-Metal Mixing and First-Principles Mobility Calculations. *Chemistry of Materials* **2015,** *27* (17), 6008-6015.

Appendix A: Supporting Data and Further Explanation

A.1 The Mixed Phase Homogeneity Characterization

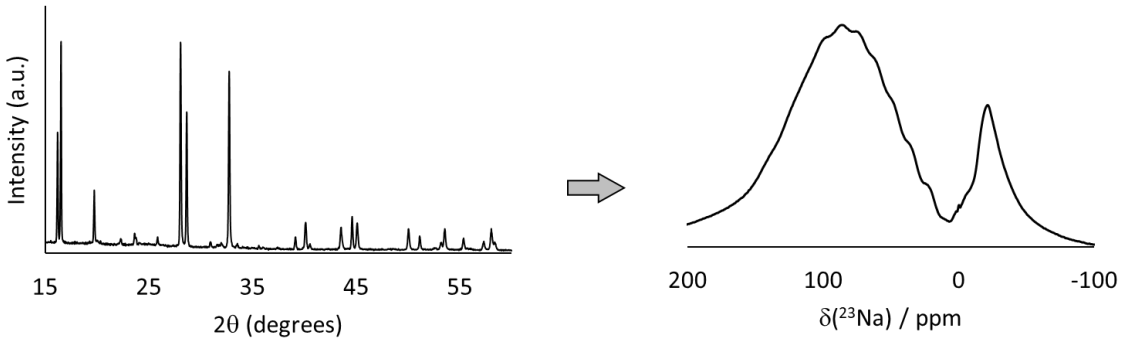

Figure A. 1 The powder XRD pattern and corresponding NMR spectrum of a synthesized mixed phase NVGPF sample ball milled for 96 hours

A.2 Detailed Description of T_1 Determination for NVGPF Sample

The T_1 of NVGPF was determined by fitting the data from a standard inversion recovery NMR experiment in two ways. In an inversion recovery experiment, the entire spectrum is inverted by a 180° pulse, and the intensity of the inverted peaks are repeatedly measured over a range of times given to allow the system to return back to equilibrium. The peak intensity can then be plotted as a function of time and fit with a first order exponential function to extract out the T_1. It has been particularly challenging to obtain a good fit for the T_1 data of NVGPF, which is primarily due to the fact there appears to be an initial very fast exchange process that takes place between the Ga-rich and V-rich peaks. Two methods were applied to fit the data, and it is currently unclear

which method yields a more accurate result. The first method was to use a two-component first order exponential function, $f(t) = z - a\,e^{bt} - c\,e^{ft}$, fit using Mathematica software. The fits for the V-rich and Ga-rich peaks are shown in Figure 5.2a 5.2b, respectively. The initial rises of both curves especially appear to fit poorly. The T1 values obtained for the V-rich and Ga-rich peaks using this method were 0.5 and 120 ms respectively. The second component of the fit, assumingly for the initial exchange

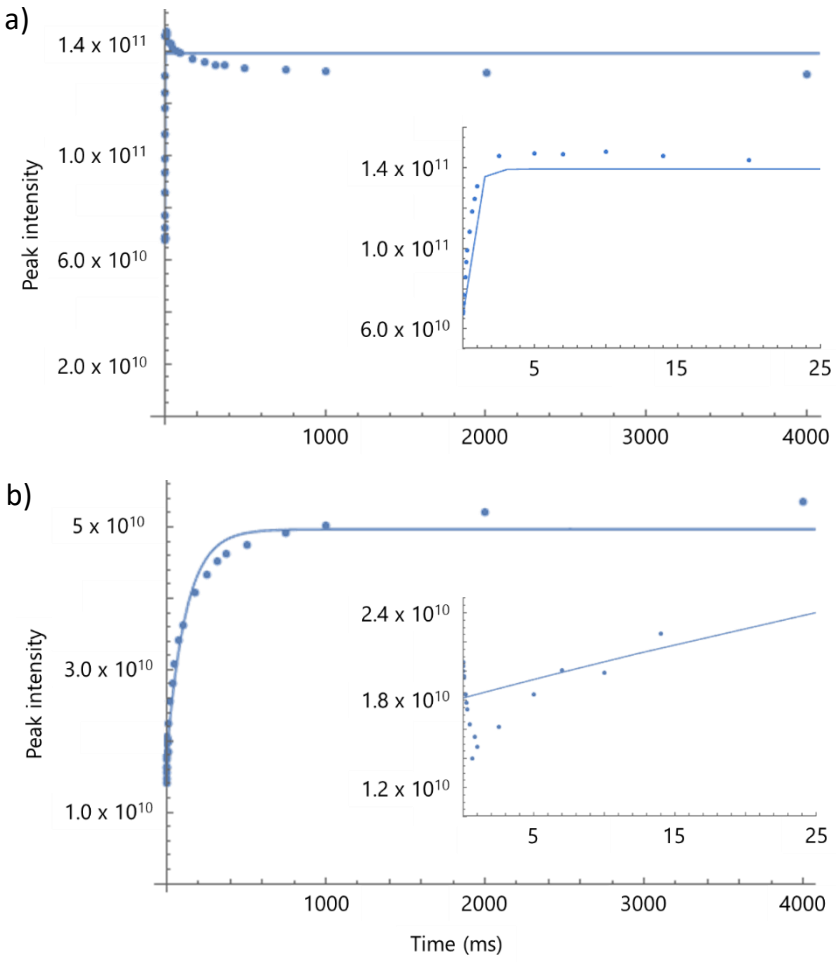

Figure A. 2 The inversion recovery data (blue dots) fit with a first order exponential function (blue curve) in Mathematica for a) the V-rich peak and b) the Ga-rich peak, with an inset of the initial rise of the both curves expanded in the inset for clarity.

process was with values of 8.6 x 10^{-7} and 4.3 x 10^{-9} ms respectively, which seems impossibly fast. Consequently, a second fitting method was employed using a program called CIFIT,[1] which is able to simultaneously fit both the T1 values and exchange process between two peaks. The fits for the V-rich and Ga-rich peaks are shown in Figure 5.3a 5.3b, respectively. The fit for using CIFIT seems only slightly better than that obtained using Mathematica, 0.5 and 140 ms respectively, however, the initial rise is still quite poorly fit. The CIFIT modeled exchange process had an exchange rate of 1.3 Hz, which in this instance appears to slow compared to the time scale of the exchange apparent in the graphs. However, the fit to the main relaxation was mechanism was similar enough for both methods that the T_1 values could successfully be estimated as the average of both fits, as reported in Chapter 5.

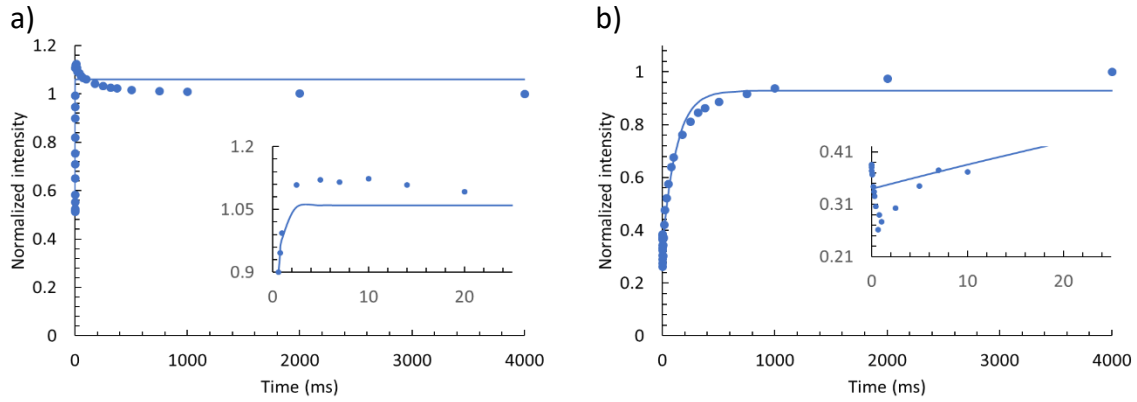

Figure A. 3 The inversion recovery data (blue dots) fit with a first order exponential function (blue curve) using the CIFIT program for the a) V-rich peak and b) Ga-rich peak, with an inset of the initial rise of the both curves expanded in the inset for clarity.

A.3 References

1. Bain, A. D.; Cramer, J. A., Slow Chemical Exchange in an Eight-Coordinated Bicentered Ruthenium Complex Studied by One-Dimensional Methods. Data Fitting and Error Analysis. *Journal of Magnetic Resonance, Series A* **1996,** *118* (1), 21-27.